A preliminary study of rainfall measurements based on four double-gauge platforms at the Government Canyon State Park, Texas

Anne Ji

Summer 2008 MORE Science

Undergraduate Student

Under the supervision of Dr. Hongjie Xie

With guidance from Mr. Newfel Mazari

University of Texas at San Antonio

Abstract

The purpose of this study is to understand rainfall patterns of the Government Canyon area and to evaluate the accuracy and precision of the tipping buckets used to measure rainfall. It is important to know how rainfall is distributed throughout an area of a radar cell and how well rainfall measurement equipment and technologies work under both uniform and non-uniform conditions. With accurate rainfall information, we can validate rainfall measurement products like the WSR-88D NEXRAD radar. In this study, a total of 8 rain gauge tipping buckets are set up at four locations within a 1 km by 1 km grid to test for rainfall patterns like uniform and non-uniform rainfall. Each location has two rain gauges mounted side by side, to ensure that the rainfall data collected is accurate. The data examined are based on the 6-minute interval collections of rainfall during the period of August 2007-July 2008. The mean, standard deviation, and the coefficient of variation are used to determine uniform or non-uniform rainfall patterns. The Coefficient of Variation (CV) measures the relative scattering in data with respect to their mean and CV=0.8 is used as a threshold to determine uniform or non-uniform rainfall. Initial findings the period of April 2008 to July 2008 (good reliable data) indicate that the percentage of uniform rainfall events decreased from April to July, while heavier rainfall increased.

1. Introduction

The spatial distribution of rainfall can be defined into two types, uniform and non-uniform rainfall events with constrains of a certain time and space scales. If the measured rainfall in an area is similar for a period of defined time and space scale, it then can be considered a uniform rain event. Rain gauges can only measure rainfall at a certain point and is only accurate when using rain gauge rainfall to validate areal radar estimation during uniform rainfall events. For non-uniform rainfall events, rain gauge measurements can not be used to validate radar rainfall estimations. Therefore it is important to know rainfall spatial distribution and variation within one radar cell (1 km x 1 km). The purpose of this study is to analyze rainfall spatial variation within one radar cell at the Government Canyon State Park using rainfall measurements from 4 double-gauges platforms, distributed in a 4 designed locations. This setup is assumed to represent the rainfall variation in the cell. Since a single rain gauge measurement in one radar cell can not be used to validate the radar estimate for those non-uniform rainfall events, 4 double-gauge platforms should be able to catch the rainfall spatial variations in the cell, thus a reasonable areal mean rainfall for the cell can be reached. Therefore, the areal mean rainfall can now be used to validate the radar rainfall estimate, even if it is non-uniform rainfall events.

2. Study area and data collection

2.1 Government Canyon and double-gauge platforms

The location chosen for the installation of the rain gauges was at Government Canyon State Natural Area in Helotes, Texas (Figure 1). The network of gauges were placed at the southern section of the park in the NE, NW, SE, and SW areas of a 1 km by 1 km grid, with 2 gauges mounted to a wooden platform at each location. The sites selected were not accessible to the public and were in relatively flat areas with little vegetation cover like grass, bushes, and trees. The highest elevation in the park was at 479.23 meters, and the lowest was at 292.92 meters. The highest location for the rain gauges was at the NW corner with 336.05m, followed by the SW at 313.57 m, then the NE at 313.03m, and finally the lowest at the SE with 308.13m. The longest distance was between the NE and the SW gages at 0.73 km. The shortest distance was between the NE and SW gauges at 0.41 km. I used the Garmin Etrex Venture GPS system to collect waypoints of the location of each rain gauge. Then I downloaded the Digital Elevation Model (DEM) of the Helotes area from the USGS Seamless website. I added the DEM and the rain gauge waypoints to the map I created with GIS.

2.2 Calibration of rain gauges and rainfall data collection

Rainfall was collected and measured with the TE 525 WS Tipping Bucket rain gauge from Campbell Scientific Inc. The gauge has an 8 inch diameter funnel shaped collector with seesaw tipping

buckets collecting 0.01in (0.254mm) of rainfall per tip. Rain collects into the tipping collector and once the collector fills with 0.254mm of rain, it drops down hitting a sensor while the other collector rises up to catch more rain. Two of these gauges are mounted on a wooden platform one meter apart from each other. The right rain gauge was named P_SW, while the left gauge was named P_LL. The gauge resolution is one tip and is limited by atmospheric conditions of temperature from 0 to $+50^0$ C and 0 to 100 % humidity.

Calibration of the rain gauges is needed to maintain the accuracy of the rainfall collection measurements. The manufacturer requires 16 oz. (14.478mm) of water to be drained into the bucket for no less than 45 minutes to simulate a normal rainfall event. To do this, a water bottle is filled with 16 oz of water and placed on the opening of the bucket. A hole is poked on the bottom edge of the bottle to let the water drain out and another hole is poked at the top to let air in. When all the water has drained out of the bottle, the number of tips recorded on the datalogger should be 57 tips with a difference of +/- of 2 tips. Two adjusting screws are located on the bottom of the rain bucket, on each side of large center drain hole. Rotating the screws clockwise increases the number of tips; counter clockwise rotation decreases the number of tips. One half turn of both screws causes a 2% to 3% change.

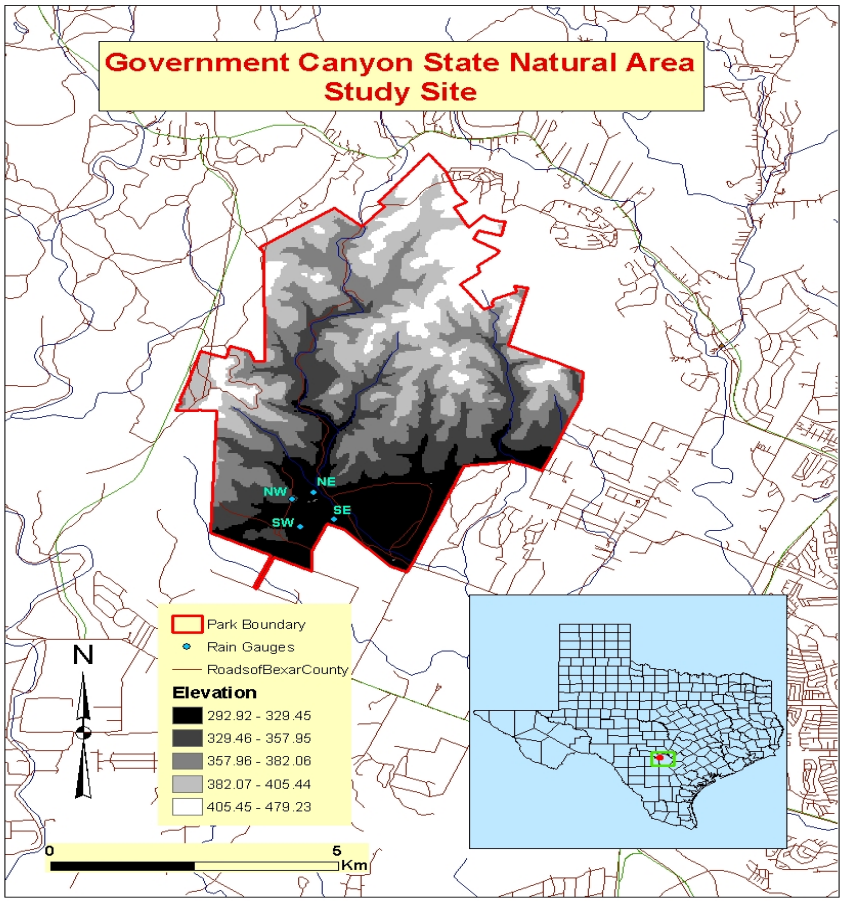

F

Figure 1. *The study area at the Government Canyon. Four cyan dots representing the 4 double-gauge platforms at one radar cell (1 km x 1 km).*

3. Data analysis and results

3.1 Errors and malfunctions of rain gauges

Mechanical malfunction of the tipping bucket rain gauge does occur when the system is jammed (by spiders or other insects) and sends continuous false pulses to the datalogger. Errors associated with mechanical gauges could also be due to heavy winds or heavy flooding rainfall events that overwhelm the tipping mechanism, causing either more or less rainfall to be recorded than the actual rain amount. A new datalogger program (XX_6MIN&60MIN_31MAR08.CR2) for the CR200 datalogger data recording scheme was used starting March 31, 2008. This has greatly increased the correlation of the P_SW and P_LL gauges at all four locations.

The datalogger records two tables of rainfall, one is 6-minute intervals and the other is hourly. It is supposed that the hourly accumulation of 6-minutes rainfall should be the same as the hourly rainfall in the hourly rainfall table. As previously mentioned, there was a malfunction in the program used before March 31, 2008. Table 1a and 1b give examples showing the mismatching. The problem was corrected after the new program was put in place.

Table 1a. 6-minute recording interval shows un-matching rainfall totals between the P_SW and P_LL gauges.

TIMESTAMP	RECORD	NERain1_mm_Tot P_SW	NERain2_mm_Tot P_LL
1/28/2008 22:15	0	8.128002	9.144002
2/15/2008 22:40	1	2.032	4.318
	TOTAL:	**10.160002**	**13.462002**

Table 1b. Hourly recording interval totals match between P_SW and P_LL gauges, but do not match the 6-minute interval totals in the Table 1a.

TIMESTAMP	RECORD	NERain1_mm_Tot P_SW	NERain2_mm_Tot P_LL
1/21/2008 14:00	0	4.826	2.794
1/21/2008 18:00	1	1.524	1.524
1/21/2008 19:00	2	0.508	0.508
1/28/2008 23:00	3	1.27	4.826001
2/15/2008 23:00	4	2.286	3.809999
2/16/2008 15:00	5	4.064	1.016
	TOTAL	**14.478**	**14.478**

3.2 P_SW and P_LL Gauge Correlations

High correlation between the P_SW and P_LL gauges is necessary for the validation of rainfall data. The possibility that the actual rainfall amount would differ just one meter apart from one gauge to another is slim. Consequently, for our rainfall measurements to be valid, both gauges at each location should measure the same or very similar amounts of rainfall per 6-minute interval, given the datalogger program was corrected on March 31, 2008. From the data, only the NW and the SE locations were the most consistent in high correlation between its P_SW and P_LL gauges as seen in Table 2.

Table 2. P_SW and P_LL Gauge Correlations:

	NE	NW	SE	SW
August (7/15/08-8/5/08)	0.9851	0.9997	0.9877	0.9868
July (6/10/08-7/15/08)	N/A	0.9890	0.9920	0.9907
June (5/4/08-6/10/08)	N/A	0.9799	0.9734	N/A
April (3/18/08-4/18/08)	0.9963	0.9920	0.8826	0.9889
March (3/3/08-3/16/08)	0.0320	0.9963	0.9802	0.6406
February (1/8/08-2/16/08)	0.00005	0.8057	0.0064	0.0013
December (11/16/07-12/2/07)	Too few and erratic data points were taken to make meaningful correlation.			
November (10/11/08-10/25/08)	N/A	0.9969	0.9944	0.2762
October (9/11/07-10/11/07)	0.7016	0.9973	N/A	0.7398
September (8/15/07-9/5/07)	0.9365	N/A	0.9933	0.7141

Note: Our datasets were not collected on an exact monthly basis and were named after the month which the data was collected.

3.3 Correlation between Locations (platforms)

Calculating the correlation of amount of rainfall between the locations was done by matching exactly the times of the 6-minute intervals between all four locations. This way, one can see obvious gaps where certain locations recorded rainfall and which locations did not. The average rainfall amount between the P_SW and the P_LL of each double-gauge platform was used to calculate the correlation between every two locations such as NE platform with SE platform (or simplified as NE and SE).

During the August period of collection (7/15/08-8/5/08), there were high correlations between the NE & SE, NE & SW, and SE & SW locations. The correlations between the NE & NW, NW & SE, NW & SW, were drastically lower as seen in Table 3. It seems that when the NW gauge is paired with the other gauges, it lowered the value of correlation. As seen in Figure 2, the NE, SE, and SW had their rainfall amounts peaking together, while the NW had its peaks after them. This showed that the rain may have moved or increased from the other locations to the NW. For the entire August period collection (7/15/08-8/5/08), the NE, NW, SE, and SW locations had an average total rainfall of 70.485mm, 72.263mm, 73.787mm, and 73.533mm respectively. The average rainfall for all four locations were very similar with very similar deviation of 1.3mm from the mean. This indicated that rainfall amounts and patterns were generally regular and uniform in this period.

Table 3. Correlation coefficients between all locations.

	NE & NW	NE & SE	NE & SW	NW & SE	NW & SW	SE & SW
August (7/15/08-8/5/08)	0.5450	0.9523	0.9261	0.6353	0.4751	0.9220
July (6/10/08-7/15/08)	N/A	N/A	N/A	0.7209	0.7723	0.9128
June (5/4/08-6/10/08)	N/A	N/A	N/A	0.9065	N/A	N/A
April (3/18/08-4/18/08)	0.5913	0.6926	0.6559	0.5421	0.7783	0.6573
March (3/3/08-3/16/08)	0.1850	0.0882	0.1002	0.3161	0.3245	0.9942
February (1/8/08-2/16/08)	0.0016	0.0222	0.0229	0.0021	0.0005	0.0002
December (11/16/07-12/2/07)	Too few data points were taken to make meaningful correlation. A malfunction with either the program or the tipping bucket caused a lot of erratic measurements between all gauges.					
November (10/11/07-10/25/07)	N/A	N/A	N/A	0.031	0.4908	0.0008
October (9/11/07-10/11/07)	0.7726	N/A	0.6743	N/A	0.5345	N/A
September (8/15/07-9/5/07)	N/A	0.6960	0.5442	N/A	N/A	0.5815

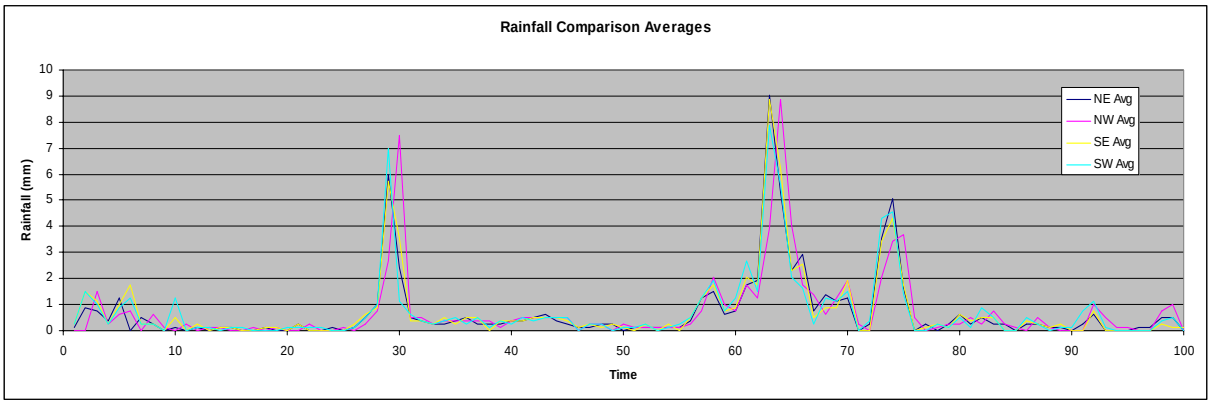

Figure 2. *Rainfall location comparison for August collection period (7/15/08-8/5/08).*

3.4 Mean Rainfall and Standard Deviation Analysis by Collection Periods

The mean and the standard deviation of each location can be compared with one another to get a sense of rainfall patterns and its variability. The mean and standard deviations were taken from the averaged P_SW and P_LL rainfall data. Table 4 shows the mean and standard deviations for each defined period of study. As shown in Table 3, data from September 2007 to November 2007 were unreliable and erratic and were not included in Table 4 for further analysis. Figure 3 shows the mean ±1 standard deviation of each location in the period of study.

Table 4. Mean and standard deviation values from all locations for February to August collection periods.

	NE		NW		SE		SW	
	Mean	ST. Dev	Mean	ST. Dev	Mean	ST. Dev	Mean	ST. Dev
February (1/8/08-2/16/08)	0.689	1.268	0.744	0.967	0.956	1.136	0.750	1.442
March (3/3/08-3/16/08)	0.700	0.887	0.615	0.824	0.692	1.020	0.645	1.102
April (3/18/08-4/18/08)	1.466	1.765	1.443	1.508	1.743	1.515	1.455	1.509
June (5/4/08-6/10/08)	N/A	N/A	0.504	1.046	0.463	1.067	N/A	N/A
July (6/10/08-7/15/08)	N/A	N/A	0.741	1.782	0.731	1.783	0.706	1.655
August (7/15/08-8/5/08)	0.705	1.361	0.723	1.370	0.738	1.377	0.735	1.335

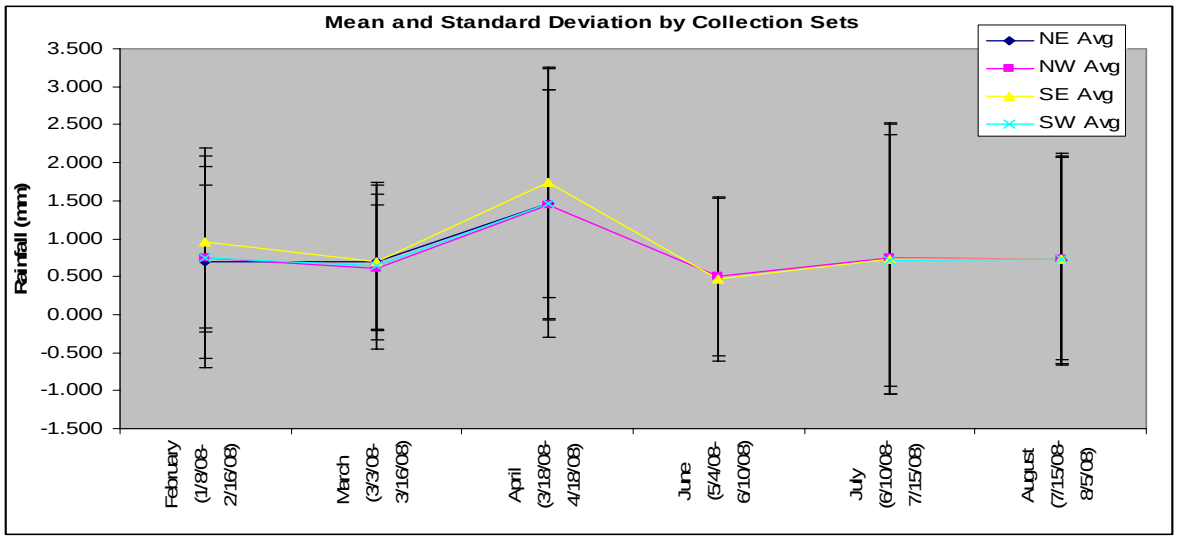

Figure 3. *Comparison of mean and standard deviation from all locations for February to August collection periods*

For the February, March, and April collection periods, the data showed a variation of the average rainfall and varying standard deviations between the locations seen in Figure 3. This signifies rainfall amounts were different from location to location, which could indicate some non-uniform rainfall. For the February collection period, the P_SW and P_LL Correlations were erratic ranging from 0.00005 to 0.8057, while the Correlation between Locations values ranged from 0.0002 to 0.0229, indicating that there was a malfunction in the program. Therefore, it is difficult to determine whether the varying rainfall means and standard deviations were actually due to non-uniform rainfall.

For the March collection period, the mean rainfall was similar and the range of the standard deviations was small compared with other months. The P_SW and P_LL correlations were high for the NW at 0.9963 and SE at 0.9802 locations, medium for SW at 0.6406, while the NE at 0.0320 showed signs of malfunction. The Correlations between Locations were erratic and low except for between the SE and SW locations (0.9942). Not surprisingly, the mean rainfall and standard deviation for the SE and SW locations were the most similar. This indicates that rainfall was uniform at the SE and SW locations. As for the other locations, uniform rainfall cannot be accurately assessed.

For the April collection period, the gauges were working properly with high P_SW and P_LL gauge correlations for NE (0.9963), NW (0.9920), SW(0.9889) locations and medium correlations for SE location (0.8826). The correlations between the locations were medium to low, ranging from 0.7783. to 0.5421. There was a slight variation of mean rainfall for the SE location, but the SE location also had the lowest P_SW and P_LL gauge correlation. In general, there seemed to be a mixture of uniform and non-uniform rainfall for the April collection period of 3/18/08-4/18/08. This was because all the gauges were working properly, but the correlations between the locations were medium to low. The rainfall patterns and peaks did not match the locations very well, as seen in Figure 4. Also standard deviation values were high and there was variability of the standard deviation between the locations, with the most prominent at the NE location.

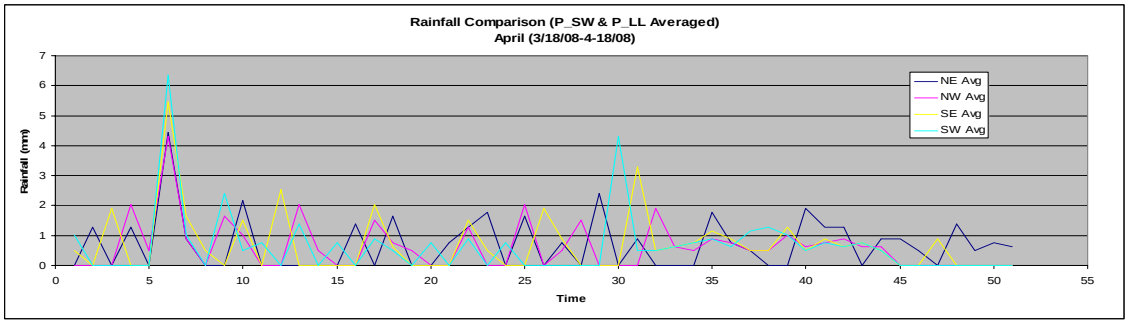

Figure 4. *Rainfall amounts comparison for all locations for the April collection period.*

For the June, July, and August collection periods, the average rainfall at each location for each month were very similar to each other. Also, their P_SW and P_LL correlations were high and the variations of standard deviation were generally low. These data show that the gauges were functioning properly, but it does not show definitive correlation between standard deviation and the amount of uniform or non-uniform rainfall. To further confirm uniform or non-uniform rainfall, another method is used to analyze for those patterns.

3.5 Using CV to Determine Uniform and Non-uniform Rainfall

The Coefficient of Variation (CV) measures the relative scattering in data with respect to their mean. In this case, CV was used as a threshold to determine uniform or non-uniform rainfall. It is defined as a ratio of the standard deviation of the 6-minute interval precipitation to the mean of the 6-minute interval precipitation in a 1 km by 1km grid (Wang, 2008).

CV = Standard Deviation / Mean

The CV values were calculated by taking the average rainfall between the P_SW and P_LL gauges for each 6-minute interval rainfall record. Then the mean and standard deviation of each averaged 6-minute interval record between all four locations were calculated. Finally, the CV for each 6-minute interval was found by dividing each standard deviation by the mean.

Small CV values indicate more homogenous rainfall data between the locations, thus signifying uniform rainfall. While large CV values indicate more scattered data, thus signifying non-uniform rainfall. There is no universal number to determine uniform rainfall. It can only be derived by examining all the CV values from each month and comparing it with each other and to all the CV values compiled together.

Quality control was applied to the original data by adjusting the placement of rainfall tips between the P_SW and P_LL gauges. The data sets that needed to be adjusted were ones where in a 6-minute interval, one of the gauges recorded rainfall, while the other gauge recorded zero rainfall. In most instances, this occurred because one of the gauge's bucket would tip after the other gauge, thus this late tip would be recorded in the next 6-minute interval.

Based on the frequency distribution patterns of the CV (Figure 5) and the analysis done in Wang's

2008 paper, we used CV = 0.8 as a threshold for separating uniform and non-uniform rain events. Therefore, uniform rainfall occurs when CV < 0.8, and non-uniform rainfall occurs when CV ≥ 0.8.

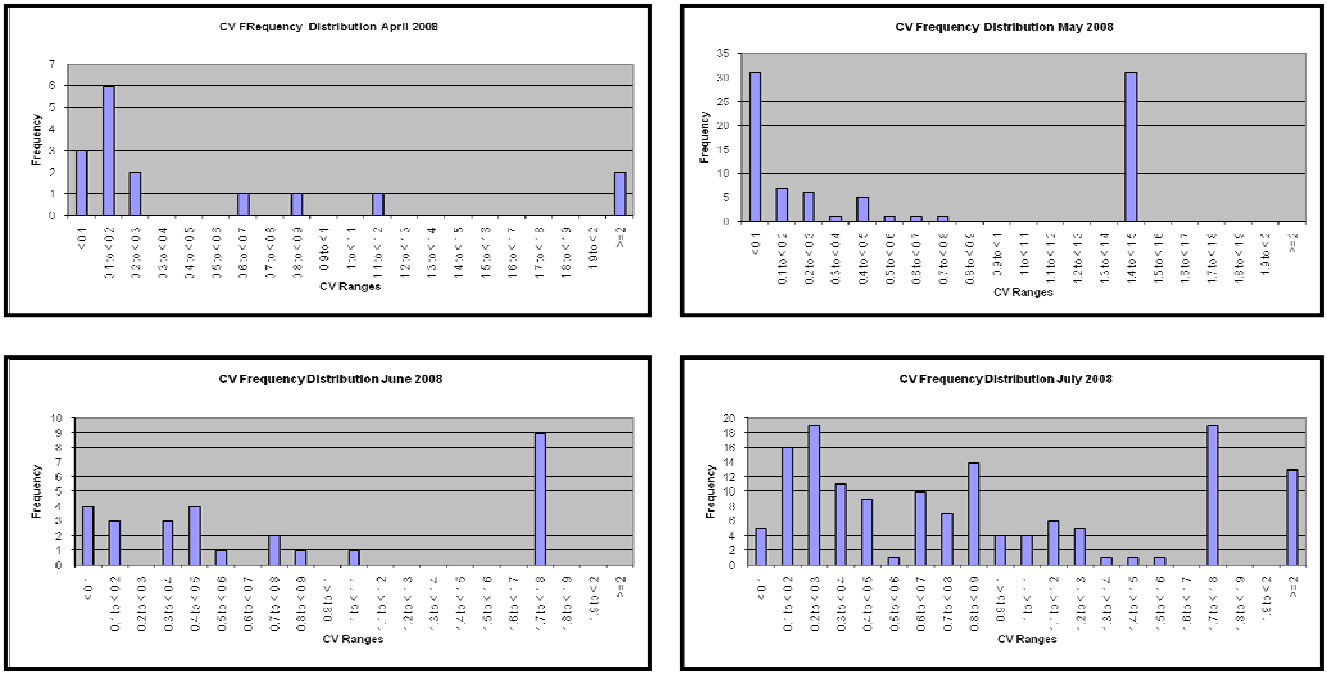

Figure 5. *CV frequency distributions from April to July 2008*

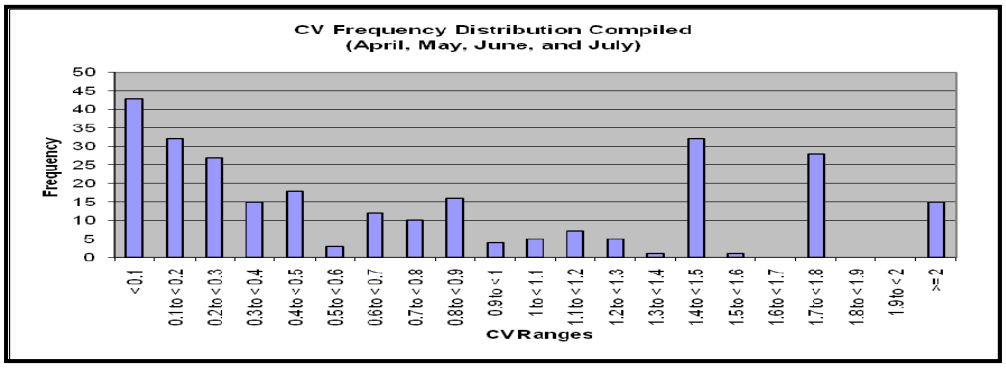

Figure 6. *Compiled CV frequency distributions*

The trend indicates that the percentage of uniform rainfall decreased from April to July as non-uniform rainfall increased (Figure 7). Uniform rainfall seemed to decrease as the average total rainfall increased (Table 5), but it could also decrease due to seasonal changes. When the CV data is compiled from all four months (Figure 6), the data showed uniform rainfall occuring 60% of the time during the April to July period.

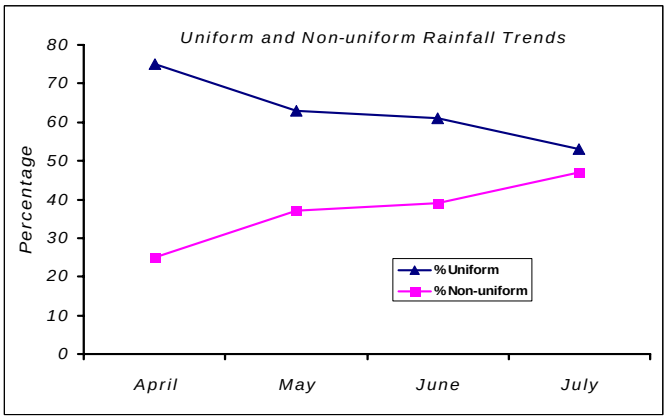

Figure 7. *Uniform and non-uniform rainfall trends.*

Table 5. Percentage of uniform and non-uniform rain.

	% Uniform Rainfall	% Non-uniform	*Avg Total Rainfall*
April	75	25	*28.7*
May	63	37	*48.7*
June	61	39	*46.2*
July	53	47	*103.7*

Next I looked at individual rain events within the month of July. Initial analysis showed that rain events with small amounts of rainfall have more CV ≥ 0.8 values and thus a higher percentage of non-uniform rainfall; even when the rainfall deviation between the locations are low. For instance, Rain Event 7/7/08 lasted 29 hrs 12 min, and only had an average of 19 mm of rain (Table 6). The standard deviation for this rain event is low at 0.639, yet much of the CV values were concentrated at CV ≥ 0.8 with 60% non-uniform and only 40% uniform rainfall (Table 6, Figure 8a). This showed that although rainfall amounts between the locations may be similar, it is not an indication of constant uniform rainfall. Small rain events like a day of constant drizzle seems to be less uniform than large rain events. For example, the duration of Rain Event 7/24/08 lasted 2hrs 24min less than Rain Event 7/7/08; it's average total rainfall was much higher at 70 mm; the standard deviation was also higher at 1.9, yet it's distribution of CV values are concentrated more on the CV < 0.8 side, with 67% uniform rain and 33% non-uniform (Table 6, Figure 8b).

Table 6. Average rainfall amounts at each location for two rain events in July.

Total Average Rainfall for July Rain Events		
	Rain Event 7/7/08 29 hrs 12 min	**Rain Event 7/24/08 26 hrs 48 min**
NE	N/A	68.326
NW	19.939	68.707
SE	18.669	72.517
SW	19.431	70.612
ST Dev	***0.639***	***1.930***

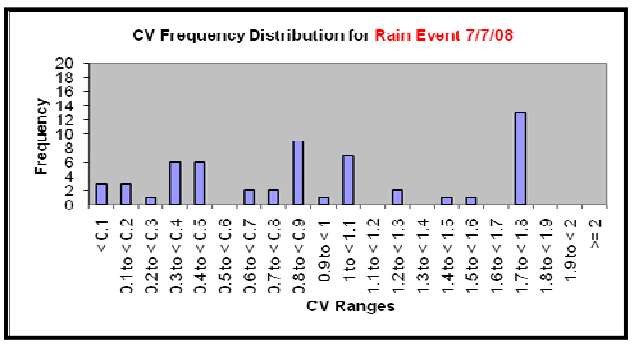

Figure 8a. *Rain event 7/7/08 CV frequency distribution*

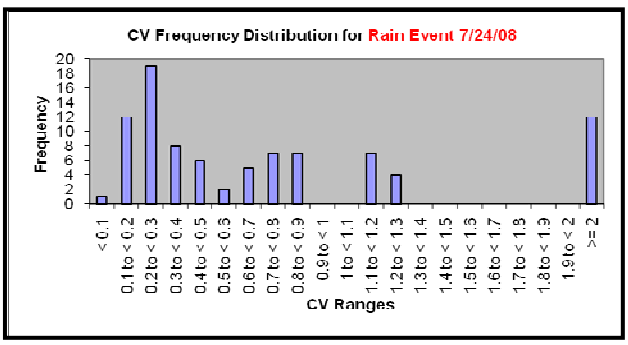

Figure 8b. *Rain event 7/24/08 CV frequency distribution*

This shows that factors like the different types of rain events (small, medium, large) and the amount and mixture they occur throughout the month also affects uniform rainfall. During a whole month there are light rain events and large storm events. Or during one rain event, rainfall may start out small, and then pour later on. All these factors can cause the standard deviation of rainfall to increase. Therefore, CV values must be used to see what percentage of the time is rainfall truly uniform.

3.6 Comparing Government Canyon Data over 30 years Trend

For more validation of the accuracy of the our rain gauges, I found San Antonio rainfall data for the past 30 years from the National Weather Service (NWS), an organization under the National Oceanic and Atmospheric Administration, which is an agency under the United States Department of Commerce. The NWS uses a vast network of ground rainfall gauge reports as a bias or correction factor with WSR-88D NEXRAD radar to measure rainfall. The radar and gauge fields are combined into a "multisensor field", which is quality controlled on an hourly basis. In areas where there is limited or no radar coverage, satellite precipitation estimates (SPE) are incorporated into this multisensor field, and it can also be used as a bias against rain gauge reports.

Since each of our data sets were not exact monthly collections, the data had to be reorganized and grouped into separate calendar months to be matched with the NWSF data. The total rainfall for each month was recalculated by taking the average between the P_SW gauge total and the P_LL gauge total from each location (NE, NW, SE, and SW). Then the totals from all four locations' were averaged together to determine the final monthly total.

Table 7. Average rainfall amounts for the past 30 years and data collected at Government Canyon.

	Avg for Past 30 years	Avg Gov. Can 2007	Avg Gov. Can 2008
JAN	46.02398065		10.16000013
FEB	43.67980645		6.318249875
MAR	57.34664516		38.70325063
APR	62.18903226		28.702
MAY	103.2632903		48.70450175
JUN	107.9663871		46.185669
JUL	68.47594194		103.6743348
AUG	54.74109677	201.8030075	
SEP	75.08567742	90.2546675	
OCT	95.06974194	30.543503	
NOV	67.03141935		
DEC	48.71883871		

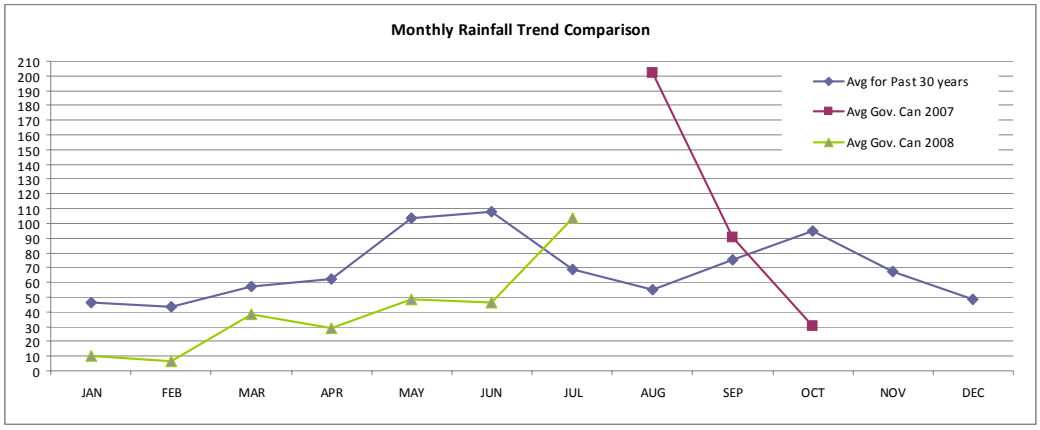

Figure 9. *Comparison of 30 years rainfall trend and data collected at Government Canyon.*

The general trend of the past 30 years gives us a guideline to follow when determining whether our gauges data is valid by comparing it to the general trend. The Government Canyon rainfall data collected from January to July of 2008 seems to follow the general trend of the averaged monthly rainfall pattern of the past 30 years (Figure 8). However, since the rainfall is restricted to a 1 km by 1 km area, Government Canyon rainfall measurements generally fall below the amount of rain of the general trend. The NWS data is from radar measurement of the entire San Antonio area; therefore the location of the park, its elevation, and surrounding vegetation may also be a factor in differing rainfall amounts. The rainfall data taken from August to October of 2007 is erratic and does not follow the trend. This may indicate that the study area had heavier precipitation above the normal. Or it could be due to many mechanical malfunctions or inaccurate calibrations of the tipping bucket or errors in recording due to faulty datalogger programming.

4. Conclusion

The gauges only worked well for 4 months (April-July) as seen in the smaller deviations from the mean, and the correlations between the gauges and locations. But the data suggests that even within a 1km by 1km grid, there is still spatial variability of amount of rainfall between different areas. During these 4 months, uniform rainfall dominated, but showed signs of increasing non-uniform rainfall. The increase in non-uniform rainfall seemed to be affected by rain events with small amounts of rain over a long period of time. Continued data collection has been going on and will continue so that enough data can be used to validate the radar rainfall for the study area.

References

Mazari, Newfel, 2008, Validation of NEXRAD Products With Rain Gauge Networks [Masters Thesis]: Department of Geological Sciences at University of Texas at San Antonio.

Wang, Xianwei, Xie, Hongjie, Sharif, Hatim, Zeitler, Jon, 2007, Validating NEXRAD MPE and Stage III precipitation products for uniform rainfall on the Upper Guadalupe River Basin of the Texas Hill Country, San Antonio, TX: Elsevier Journal of Hydrology (2008) 348, 73-86.

National Weather Service website for San Antonio Monthly/Annual Average Precipitation 1871-July2008: http://www.srh.noaa.gov/ewx/html/cli/sat/satmonpcpn.htm

Nutrient Dynamics in Antarctic Sea Ice

Undergraduate Student
Beverly Saunders

Advisor
Stephen Ackley
Department of Earth and Environmental Sciences
University of Texas at San Antonio

MORE Science Colloquium: Final Paper

Nutrient Dynamics in Antarctic Sea Ice

Abstract
The ecological systems within Antarctica are highly dependent on biological activity within the sea ice. This activity is in turn largely dependent on the physical processes and dynamic sea ice interactions which are unique to Antarctica. In addition the porosity of ice which allows for nutrient transport also plays a very large role in microbial community development. Nutrient values are dependent on the amount of biological activity present within the ice as well as the ice formation processes while isotope values depend solely on the latter. Studies looking at the nutrients, chlorophyll a and isotope values are needed in order to confirm models describing sea ice interactions and also in order accumulate data so that trends may be established over time. This report presents SIMBA cruise 2007 nutrient and isotope profiles of ice cores taken from the Bellingshausen Sea Ice. The profiles show counterintuitive trends and require further evaluation.

Introduction
Sea Ice processes within the Antarctic represent complex and unique environments that support one of the most pristine ecological systems in the world. This ecological system is highly dependent on krill populations represent the main food source for higher trophic levels. Krill and other food sources are directly related to the microbial communities associated with the Sea Ice. Understanding this relationship leads to the conclusion that the biological and chemical characteristics of this highly heterogeneous and dynamic Sea Ice system have direct effects on the Southern ocean food web in general and on the overall equilibrium of Antarctic Marine life (1).

This paper will be highlighting the nutrient dynamics in sea ice and its relationship to the overall development of microbial communities in the Antarctic. These dynamics, based on a relationship between physics and biology within the ice, are ones that have few datasets and so are largely understood qualitatively (1) but yet are still necessary in order to fully understand how sea ice plays a role in the ecological system as a whole.

I will begin by giving a brief review of Sea Ice physical characteristics and general pathways to formation (highlighting ice types and their formation pathways) and how these different categories can be differentiated when an ice core is extracted (ice structure and sable isotopes). I will then introduce the concept of inorganic nutrients (nitrate, nitrite, phosphate, ammonia and silicate) within Sea Ice which are present due to both conservative deposition and biological processes. This will include a brief introduction to the conservative incorporation of nutrients into the sea ice and what patterns or values should be expected if this were taking place without biological interference. I will then discuss porosity of sea ice and percolation of nutrients within sea ice which makes internal biological activity possible and allows for growth to be largely unlimited by nutrient depletion. Finally I will mention the types of microbial environments located throughout sea ice profiles and how their presence effects the nutrient concentrations.

Once these concepts have been discussed I will highlight the methods that are used to extract nutrient and isotope data from water samples which I learned to use proficiently through this research. I will then briefly discuss the data extracted from the five ice cores extracted site Brussels (a fixed site) within the Bellingshausen Sea, in a time series fashion during the SIMBA cruise 2007. These profiles still need to be compared to the nutrients in the surrounding seawater and so still need work completed in order to allow for data interpretation.

Sea Ice Characteristics

Sea Ice is a complex material which includes pure ice in conjunction with brine and air inclusions. Its structure and characteristics are dependent on various factors including temperature, salinity and formation pathways. The brine inclusions present in sea ice provide environments for microbial growth and high primary productivity (2) and lead to highly localized growth all over the Antarctic (3). Sea Ice is also one of the few materials on earth whose bulk material properties vary extensively even with slight temperature changes (4) (ex. Porosity).

The sea ice based biological community characteristics, and in turn expected nutrient values, are greatly influenced by which ice type is present (discussed further in sections below) (3). The different types of ice that will be discussed in this report include frazil ice, snow ice, congelation ice and platelet ice. Frazil ice is made through turbulent processes packing ice crystals formed during initial freezing of sea water. Snow ice is formed through surface flooding and subsequent freezing of flooded snow. Congelation ice is formed underneath an already formed ice flow through the freezing of the sea water, below resulting in a highly structured ice crystal formation. (2) Platelet ice consists of ice crystals formed by super cooling which consist of 25% ice and 75% sea water and are located along the bottom of ice flows (1). Each formation pathway and structure has an influence on their chemical and biological characteristics.

Methods for Determining Formation Pathways

In order to determine the formation pathway sample consists of two procedures. This first is to classify the sea ice segments into ice types by looking at a thin slice of the sample with polarized light. Each ice type has a specific crystal size and orientation which generally be determined by this method and will be classified as Platelet, Columnar or Granular. The platelet structure and columnar structure are indicative platelet ice and congelation ice respectively. Granular structures however can indicate two different ice types; snow ice or frazil ice. As mentioned before snow ice is derived from snow becoming flooded and then freezing over while frazil ice is formed directly by seawater freezing (turbulent forces). These differences in formation give rise to different oxygen isotope ratios within the samples. Snow ice, which is made primarily of precipitation in the form of snow, has significantly lighter oxygen isotopes due to preferential evaporation of lighter oxygen isotopes. In contrast frazil ice, directly frozen seawater does not have this preferential fractionation present. By analyzing these values the sea ice formation pathway can be determined.

Nutrients in Sea Ice

Inorganic nutrient concentrations including silicate, phosphate, ammonium, nitrate and nitrite are found within sea ice samples. The incorporation of these nutrients is due to one of two processes; the first is physical incorporation (independent of biological activity) which would be indicated by a conservative salinity to nutrient relationship. The second is based on biological activity which can cause depletion of nutrients or elevated values depending on the types of organisms present and whether or not seawater exchange is taking place (5). The nutrient values relative to sea water can therefore tell us a great deal about the amount of sea water interactions that are taking place, the amount of biological activity and

the types of biological communities and thus are common measurements to make when analyzing ice core samples.

Conservative Nutrient to Salinity Ratio

In abiotic systems, when biological influences are not a factor, nutrient concentrations within sea ice should be proportional to the salinity of the ice (reflecting brine rejection and subsequent loss of nutrients) meaning any nutrient concentrations should be proportional to the amount of seawater that is included within the sea ice structure. This model of nutrient values within sea ice does not hold true in ice cores that have biological factors involved. In many studies phosphate, sulfate, nitrate, nitrite and ammonium levels have been observed to be either far depleted or far in excess to the dilution curve of surrounding seawater (7, 8, 9, 11). Silicate tends to have the largest affinity to staying within the dilution curve with the exception of areas where diatom populations are prevalent (3).

As a result the dilution curve associated with seawater in the sample area is used in order to find whether nutrient levels have been depleted or replenished/ incorporated in the ice through biological and physical processes beyond those predicted of the conservative model (3) (7).

Sea Water/ Nutrient Exchange

If sea ice were a closed system then it would be expected that the presence of primary production would cause a depletion of the initial nutrient deposits in all sea ice communities except for bottom communities which are directly associated with seawater. However nutrient values far in excess to that of sea water, and biological communities whose growth surpass that which could be supported a limited supply of nutrients, are commonly observed. This realization as well as observations of things like brine channels and surface flooding allows scientists, with certainty, to claim that sea water exchange within sea ice has major effects on sea ice characteristics (biological, chemical and physical).

The percolation theory addresses the physical conditions necessary to allow for sea ice to become porous and therefore a media for exchange. This theory is referred to the “law of fives” and states that once sea ice in Antarctic hits a temperature of -5 degrees Celsius, a salinity of 5ppt and a critical brine volume fraction of 5%, it then becomes permeable to seawater coming from below or above. These interactions are what drive a great deal of microbial growth that takes place in Antarctica as it makes nutrient exchange much more common and reduces nutrients role as a limiting factor. These interactions are also useful as they give an indication of the amount of nutrients that run through the system (9) when compared to biological growth.

Biology in Sea Ice

The presence of biological communities within sea ice is often what drives nutrient concentrations away from the dilution curve. In order to analyze why nutrient concentrations vary we must first understand where biological communities are located and the physical processes that take place which provide the “seed population and nutrients”. There are three layers of biological growth; surface, interior and bottom (9). Each community type often is observed within ice cores, their prevalence and characteristics dependent on the sea ice type and external conditions. The types of communities and processes involved in creating these layers are discussed below.

Surface Communities

High nitrate and silicate concentrations (five to ten times the surrounding sea water) as well as nutrient depletion have been observed in the surface communities (5). These communities are formed through the introduction of seawater which supplies microbial communities with ample nutrients, and a possible

seed population, in order to begin a microbial community (9). This is confirmed by high surface salinities which tend to be found within these communities (3). Two different surface communities have been observed in Antarctica. They result from different processes which lead to the introduction of seawater to the surface. The first process is associated with snow loaded areas. The second process is associated with pressure ridges.

Snow loading

These communities directly result from snow accumulation on the surface of porous sea ice which leads to the creation of slush pools from subsequent flooding through cracks and pores. This provides the starting conditions necessary for primary production as long as warm temperatures and high irradiance are present (9). These kinds of communities have been shown to hold 10-400ug/m3 of chlorophyll a (1) and are associated with 50% of Antarctic Sea Ice (Legendre et al. 1992). It is also believed that these types of communities are associated with very high primary and secondary production and could possibly be the largest sea ice community producer of carbon (1).

Pressure ridges

Pressure ridge communities have been observed frequently in heavily ridged areas of the Western Weddell Sea. These surface habitats result from pressure ridge interactions and can be formed due to three distinct processes which introduce sea water to the surface. The first takes place during the formation of pressure ridges (one block loading onto another) which causes cracks to be deflected below sea level. This type of community has been found associated with 43mg/m^3 of chlorophyll a (an indicator of primary activity) (1).

The second process involves marginal ice zone where large flows break off and head towards open water. The weight of the ridge is offset momentarily below sea level causing a pool of sea water on the surface which can be distinguished from melt ponds by the high salinity associated with these communities. These types of communities have been associated with algal growth of ten to hundred times that of areas without this flooding as well as the nearby seawater (1).

The third surface community is associates with ice blocks that are submerged in seawater due to ridging. These kinds of communities have not been quantitatively measures but were observed on the AMERIEZ cruise in 1986 (1).

<u>Interior Communities</u>

Two kinds of interior communities are associated with Antarctic sea Ice. The first is the frazil ice community and the second is the freeboard layer community (or “gap layer”). These two communities have very different biological characteristics and formation mechanisms.

Frazil Ice

Frazil ice is formed by ice crystals packing together as a result of turbulent forces. Unlike columnar ice this ice type is associated with high chla levels (from algae) even within young ice. Young frazil ice also associated with conservatively distributed nutrient values (correlating with seawater dilution curve). These observations lead to the conclusion that the incorporation of biological matter is due to physical incorporation rather than biological activity (which would result in nutrient levels either above or below dilution curve). This takes place as the ice crystals move vertically through the water column catching biological matter along the way (a process called scavenging) or though wave pumping associated with the formation of the pack ice itself (1). This type of initial accumulation of biological matter can account

for concentrations of up to 10^6 cells per liter and also explains biology being present throughout the flow rather than preferentially at the top or bottom.

After the initial incorporation of the biological matter changes in species composition takes place within the ice due to in situ growth, in response to limiting factors and species succession that is associated with the localized flow. These types of changes in microbial composition cause changes in nutrient concentrations. Frazil ice communities occur in low amount in comparison to other sea ice communities but could have a significant impact in the food chain of the Weddell Sea where it has been suggested that accumulation of frazil ice is continuous (6).

Freeboard Layer

Internal layers or "gap layers" are located at about 20-30cm depths in late first year and second year Antarctic ice and are characterized by a partially melted honey comb or slush layer filled with sea water and high biological activity. They are found under intact surface layers of snow and ice and often above less porous ice. They are also associated with brine channels which travel through the columnar ice below allowing drainage to take place (10).

Up until recently, there were three main theories attempting to explain these gap layer observations, each not fully explaining all the observations noted in reference to these gap layers through Antarctica. The first was a physical-biological feedback system proposed by Ackley et al. (1979) which explained the melted layer by algal blooms, enhanced by brine drainage, below the ice surface, accelerating melting by solar radiation absorption. This theory was later disproved by experiments showing the radiation was not enough to account to melts that were often observed. The second theory, purposed by Fritsen et al. (1998) attempted to explain the hard ice cover that is sometimes observed over the gap layer. This theory says the layer originates as surface slush and then as snow melt and hits this layer an impermeable layer of superimposed ice forms. This is inconsistent with gap layers that do not have this superimposed ice above the gap layer as observed by Gow et al. (1987). The third theory was that snow induced flooding, and partial top down freezing of flooded snow, causes brine rejection to lower levels and consequentially lowers the freezing point causing subsequent melting. This theory did not explain the honey comb structure often observed (10).

The general theory that explains the wide range of observations is a mechanism in which heat is pumped into the gap layer by inverted summer temperature gradients. This thermal conductivity is dependent on salinity and takes into account the thermal properties of the upper layers of sea ice as it is warmed, brine is drained through brine channels and salinity is lost. The melting then lakes place at sea level where the melting point for sea water is located. This model explains the honeycomb structure of these layers by saying only internal melting is taking place and also explains horizontal widening. This also explains gap layer presence in many environments as it can happen in most summer sea ice. This theory can then be coupled with the earlier theories mentioned above to explain the observations often made (1).

The high biological activity is evident within these gap layers due to the dark color associated with their presence. These communities are often also associated with krill population. These microbial populations also have a huge effect on the mass balance of sea ice throughout the Antarctic and on the nutrient composition.

Bottom Communities

The bottom layer of sea ice is characterized by two different types of ice, columnar and in select regions platelet, each associated with communities that grow along the bottom of the pack ice. These types of communities have the most capability of free exchange with sea water as they have direct contact and diffusion potential. As a result they tend to have different limits to growth than the rest of the communities discussed. Instead the largest limiting factor in these communities is light availability (severely hindered by now cover and ice thickness). This fact limits these types of communities largely to the coastal regions (1). These types of communities are also more common to bloom in Antarctica in the fall.

SIMBA cruise 2007

As I mentioned, nutrient exchange and concentrations are necessary to evaluate when looking at the biology of the ice within Antarctica. Correlations between the nutrient data, ice types and biological presence have potential for being discovered and understood as datasets grow. This is a goal that is often addressed on cruises traveling to Antarctica, including the SIMBA cruise in 2007.

Five ice cores were extracted from a specific location in the pack ice of the Bellingshausen Sea. They were taken over a time series and then analyzed for ice structure, chlorophyll a, inorganic nutrients, salinity and temperature. During my research I learned the methods used in order to extract this data (and applied my knowledge by processing Antarctic water samples). I also analyzed this data using excel programs in order to produce the profiles presented in this report. The ultimate goal of the research is to examine what values can be explained by observations and theories that have been made in past published works and to find a way to explain nutrient depletion and/or excess within the cores.

Extracting Nutrient and Isotope Data

In order to extract isotope values a mass spectrometer is used to measure the oxygen 16 to oxygen 18 ratios. During the application of this method I used a Finnigan Gasbench which requires each sample to be flushed with carbon dioxide and allowed to equilibrate (thus making to possible to sample the air instead of the water in order to gain the correct values). This method is called Carbon Dioxide Equilibration and is a widely accepted technique. In order to measure the Nutrient values for the water samples a Lachat Nutrient Analyzer was used which utilizes a combination of chemical interactions in order to determine the nutrient levels of the samples.

SIMBA 2007 Extracted Data

Once all of the data was extracted from the five cores from the Brussels site it was then input into excel and profiles were created of the ice type, salinity, chlorophyll a and nutrients for each of the cores. By comparing these profiles a visual correlation could be established between each of then

The data is not entirely completed but in progress. In order to see the data thus far as it continues to progress please refer to Appendix A. Take note that dilution curves representing sea water levels must still be evaluated in order to really be able to interpret the data. This is also in progress. The correlations found in the core profiles are counterintuitive and require further evaluation

Conclusion

Nutrient interactions within Antarctic Sea Ice are influenced by salinity, nutrient exchanges and biology. These interactions can yield chlorophyll A values well above those exhibited by the sea water and pave the way for microbial communities and the food chain in Antarctica. Understanding and learning more thoroughly the stories behind nutrient values, their causes and meanings, will help the scientific

community to truly evaluate nutrient composition comprehensively. As a result more expeditions to Antarctica need to take place in order to accumulate data on biological sea ice interaction.

Acknowledgements
I first want to thank my advisor Stephen Ackley for giving me such great opportunities over the past few years. I learned a great deal about lab work and data analysis as well as the overall scientific process. As a result of my work with Stephen I feel far more prepared to begin my graduate studies.

In addition I would like to thank Dr. Debajyoti Paul for allowing me to use his laboratory in order to learn the techniques needed in order to analyze oxygen isotope values within water samples. While the project was cut short I learned a great deal.

I would also like to thank the MORE science program for the funding which allowed for me to proceed with this project and various others. The opportunities this funding has provided for me has allowed me gain extensive experience within the world of scientific research.

Bibliography/ References

1) S.F. Ackley and C.W. Sullivan, 1994. Physical Controls on the development and characteristics of Antarctic Sea Ice biological communities. *Deep Sea Research 1, Vol. 4, No.1, p*1583-1604.

2) D.L. Garrison, C.W. Sullivan and S.F. Ackley 1986. *American institute of Biological Sciences Vol. 36, No. 4.* p243-249.

3) D.B. Clarke and S.F. Ackley, 1984. Sea ice Structure and Biological Activity in Antarctic Marginal Ice Zone. *Journal of Geophysical Research Vol. 89, No. C2.* p2087-2095

4) K.M. Golden, S.F. Ackley and V.I. Lytle, 1998. The Percolation Phase Transition in Sea Ice. *American Association for Advancement of Science. Vol. 282, p2238-2241.*

5) D.N. Thomas, S. Papadimitriou, 2003. Sea Ice: An Introduction to its Physics, Chemistry, Biology and Geology. *Blackwell Science Ltd. Biogeochemistry of Sea Ice.* p279-286

6) D.L. Garrison, S.F. Ackley and K.R. Buck, 1983. A Physical Mechanism for Establishing Algal Populations in Frazil Ice. *Nature, Vol. 306, No. 5941, p363-365.*

7) G.S. Deickmann, M.A. Lange, S.F. Ackley an J.C. Jennings Jr., 1991. The Nutrient Status in Sea Ice of the Weddell Sea during winter: Effects of Sea Ice Texture and Algae. *Polar Biol II p449-456*

8) D.B. Clarke and S.F. Ackley, 1982. Physical, Chemical and Biological properties of Winter Sea Ice in the Weddell Sea. *Antarctic Journal of the United States. Vol XVII no.5, p107-109.*

9) S.F. Ackley, C.H. Fritsen, V.L. Lytle, 1996. Freezing Driven Upwelling in Antarctica Sea Biological Systems. and C.W. Sullivan. *Proc. NIPR Symp.Biol.,9, 45-49.*

10) S.F. Ackley, M.J. Lewis, C.H. Fritsen and Hongjie Xie. Internal Melting in Antarctic Sea Ice: Development of "Gap Layers", 2008. *Geophysical Research Letters, Vol. 35, No.11 503.*

11) J.C. Jennings Jr., L.I. Gordon and D.M. Nelson. Nutrient Depletion Indicates High Primary Productivity in the Weddell Sea. *Nature Vol. 308, no.6393, p 51-54*

APPENDIX A: SIMBA CRUISE 2007 Analyzed Nutrient Data

Overall Data Set

Salinity vs. Nutrient Concentration

SIMBA Cruise, Brussels Site

All nutrient values for the five cores taken at Brussels site platted against their salinity measurements.

Dates extracted: Oct. 1st – Oct. 21st 2007.

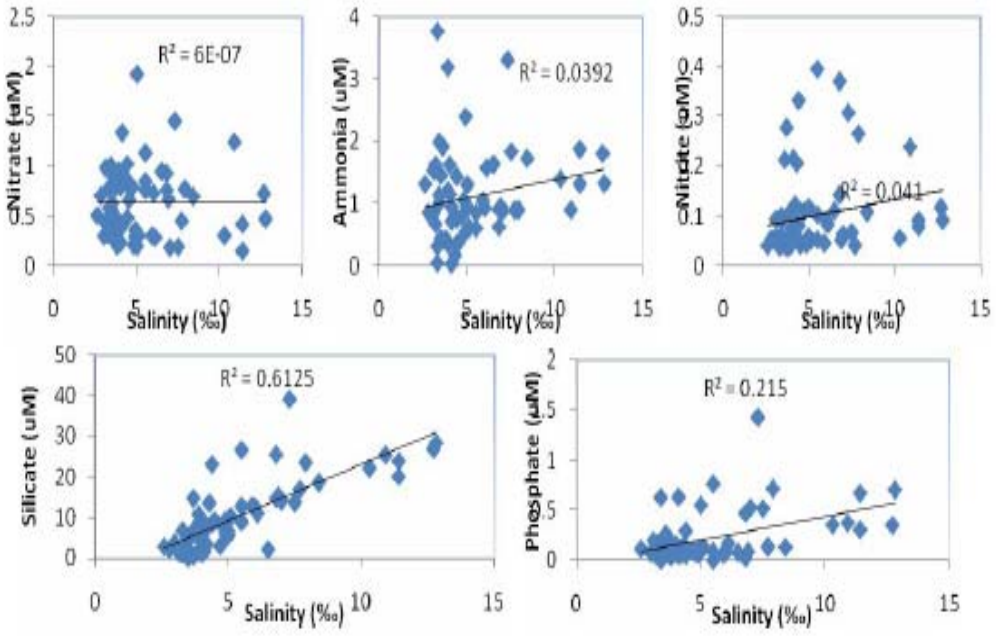

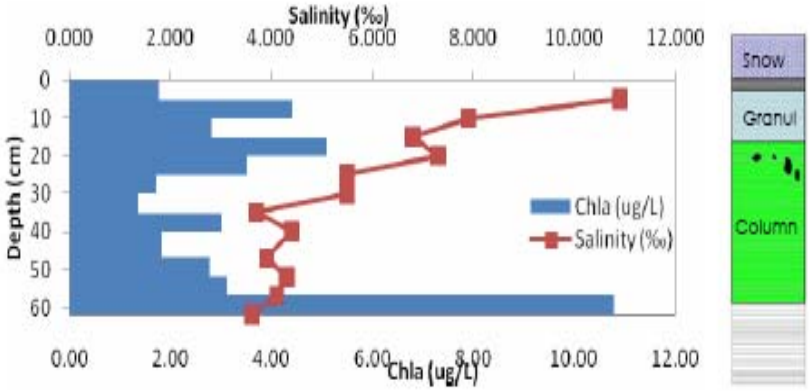

Ice Core #1: SIMBA Cruise, Brussels Site.

Chlorophyll A, Salinity, Nitrate, Nitrite, Phosphate, Silicate, Ammonia and Ice Type Profiles.

Date extracted: Oct. 1st, 2007.

Note: Core Profile from Fred Brabant EGU Presentation

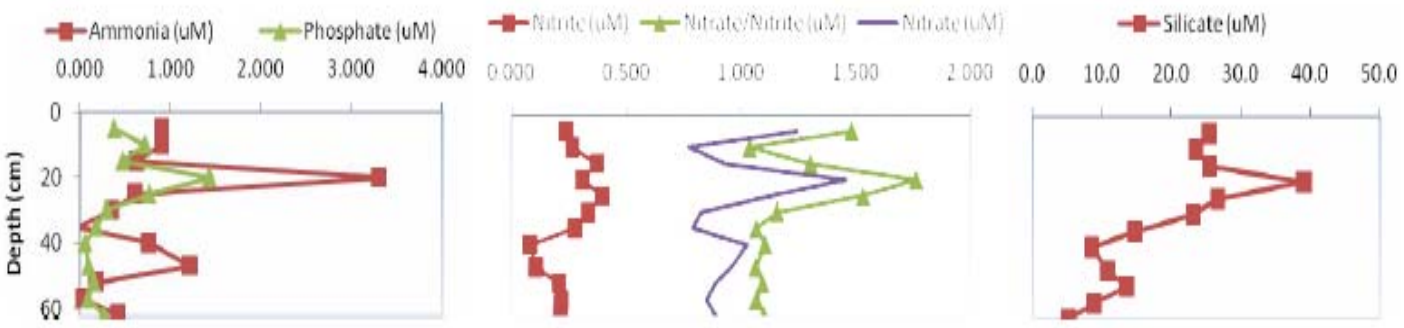

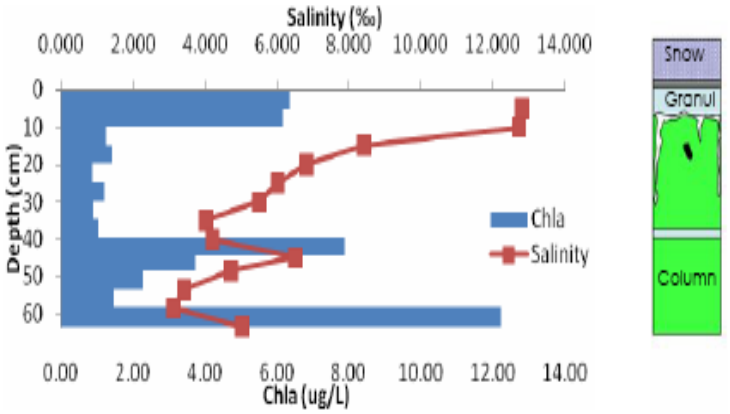

Ice Core #2: SIMBA Cruise, Brussels Site.

Chlorophyll A, Salinity, Nitrate, Nitrite, Phosphate, Silicate, Ammonia and Ice Type Profiles.

Date extracted: Oct. 6th, 2007.

Note: Core Profile from Fred Brabant

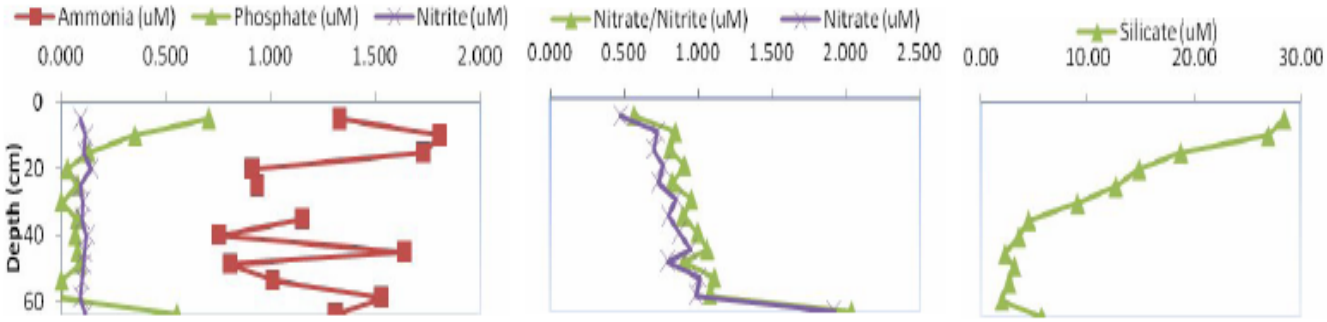

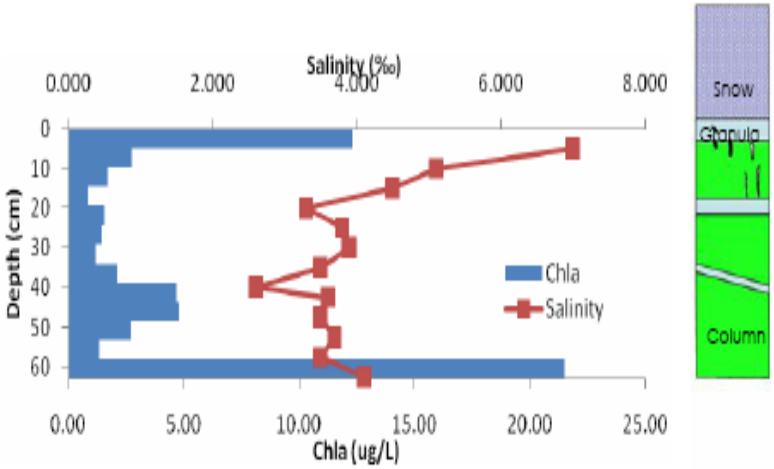

Ice Core #3: SIMBA Cruise, Brussels Site.

Chlorophyll A, Salinity, Nitrate, Nitrite, Phosphate, Silicate, Ammonia and Ice Type Profiles.

Date extracted: Oct. 10th, 2007.

Note: Core Profile from Fred Brabant

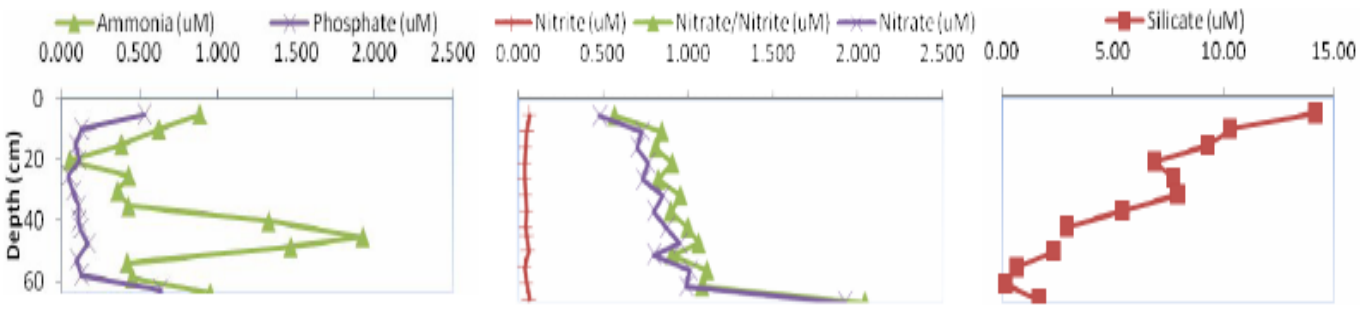

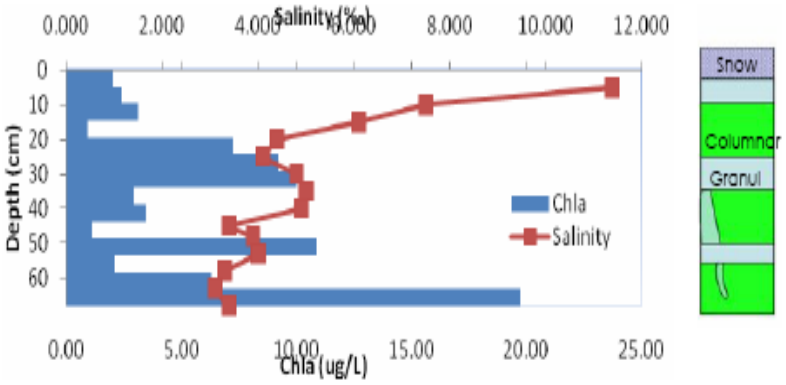

Ice Core #4: SIMBA Cruise, Brussels Site.

Chlorophyll A, Salinity, Nitrate, Nitrite, Phosphate, Silicate, Ammonia and Ice Type Profiles.

Date extracted: Oct. 16th, 2007.

Note: Core Profile from Fred Brabant EGU Presentation

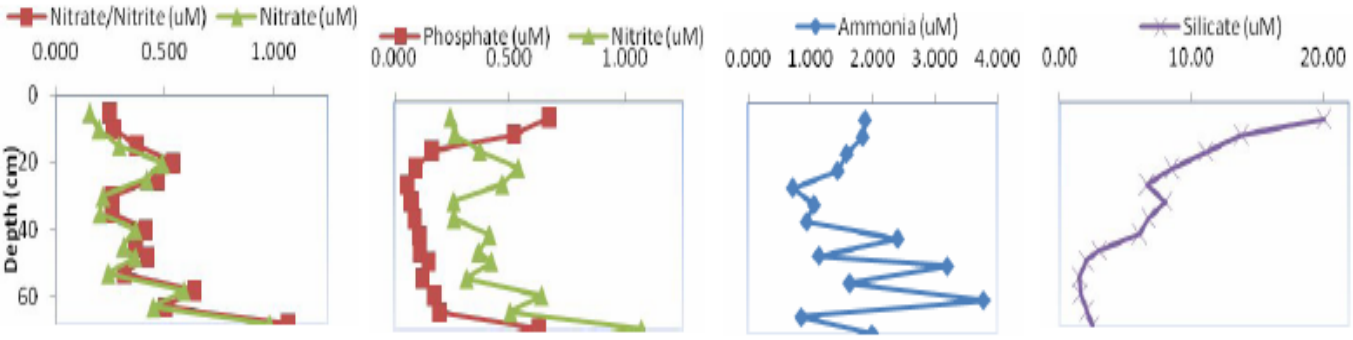

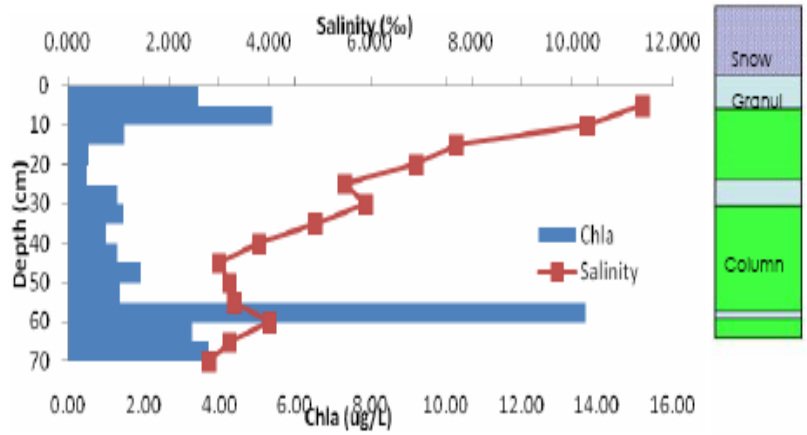

Ice Core #5: SIMBA Cruise, Brussels Site.

Chlorophyll A, Salinity, Nitrate, Nitrite, Phosphate, Silicate, Ammonia and Ice Type Profiles.

Date extracted: Oct. 21st, 2007.

Note: Core Profile from Fred Brabant EGU Presentation

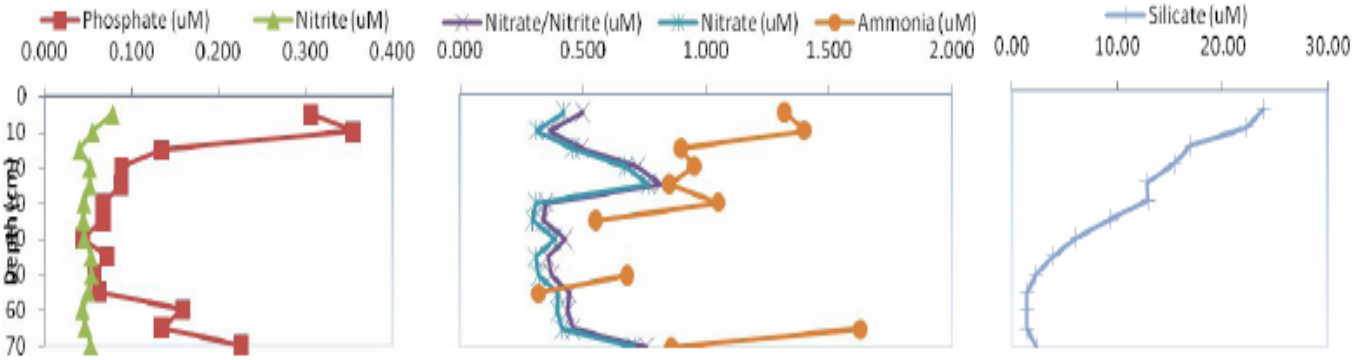

Morphometric Analysis and Landscape Evolution from Gridded DEMs

Donald M. Hooper

Jeffrey L. Allen

Southwest Research Institute San Antonio

Morphometric Analysis and Landscape Evolution from Gridded DEMs

Abstract

This study focuses on the ability to obtain topographic information from Digital Elevation Models (DEMs) to interpret landscape characteristics and evolution. Slope, elevation, and aspect data were extracted from gridded 10 m (meter) DEMs, then summarized and compared to their respected geologic formation or setting. The areas of interest contain different sets of data comprised of 250 m^2, 10,000 m^2, 22,500 m^2, 250,000 m^2, and 10^6 m^2 regions. Each landscape or terrain type chosen represents an area of change by various means of geologic activity throughout the United States: drainage pattern, glacial, volcanic, dune, karst, impact crater, ridge-and-valley, canyon, and mesa and butte. These selected areas provide well-defined topographic features which make this study and the data more unambiguous. In order to explore the DEMs and obtain the data, we used the software package ENVI (version 4.5). KaleidaGraph (version 4.0) was used to organize and statistically analyze the data. The data collected from the DEMs helped visualize even the most minuscule topographic feature. The methods employed show great promise for rapidly computing geomorphometric parameters. The landforms display morphologic and morphometric characteristics that can be quantified. Several landforms exhibit high mean slope values that are discernable at various spatial scales from other landforms or terrain types. This study endorses the use of 10-m DEMs to define, analyze, and read topographic sections, whether large or small scale.

Introduction

The ability to visualize and define earth's topographic features and locations effectively is a useful tool for many professions and individuals. Digital Elevation Models, or DEMs, are a way to ease the process of gathering the data as well displaying the data more clearly and successfully. In this case, to help people become more acquainted with Earth's topography and to conduct geomorphometric analysis. Digital elevation models are rectangular grids of elevation values that provide a tool for geomorphometry. The DEM is a raster grid of elevation values derived from the U.S. Geological Survey (USGS) 7.5 minute topographic maps. DEMs allow a multitude of data parameters to be stored for any region, including slope, elevation, and slope aspect, the topics of this study.

There are different quality DEMs, 90, 60, 30, and the most recently, 10 m (meter). For this study we chose the highest resolution, 10 m. We do believe a lower resolution would have been sufficient for this project, but 10 m resolution was available for each of our targeted study regions and is superior to 30 m DEMs when analyzing small landforms (e.g., dunes). Being the most recently acquired and processed, high resolution 10 m DEMs do not have complete coverage across the United States (or the world). To gather DEMs takes time and is a lengthy process, thankfully the U.S. has the most aggressive programs in the world for mapping DEMs (Guth, 2003).

The purpose of this study is to use digital elevation models to conduct a geostatistical terrain analysis of common fluvial, volcanic, tectonic, and eolian terrain types. To acquire, organize, and interpret topographic data, the USGS website and seamless data provider, ENVI 4.5 (version 4.5), and KaleidaGraph (version 4.0) were used extensively. Topographic maps and DEMs were obtained from the U.S. Geological Survey (USGS, 1999, 2000). Topographic data were then extracted into ENVI, a software program that allows the user to view and manipulate the data. KaleidaGraph was used to organize the datasets and produce statistics from the topographical information. Similar to a Microsoft Excel program, but more specific towards science and data, KaleidaGraph makes it easy to organize, explore, and analyze data. Slope, aspect, and elevation were the key morphometric parameters acquired.

Data

Digital elevation models (DEMs) are used often in geographic information systems (GIS). The grid cells of a DEM are spaced at regular intervals along south to north profiles that are ordered from west to east. Other DEMs or digital terrain models (DTMs) are composed of a triangular irregular network (TIN) rather than a grid of squares. DTMs were not used in this study. The U.S. Geological Survey (USGS) produces five primary types of elevation data: 7.5-minute DEM, 30-minute DEM, 1-degree DEM, 7.5-minute Alaska DEM, and 15-minute Alaska DEM (USGS, 2000). The USGS 7.5-minute topographic quadrangle map series was used in the initial stages of this study to select and locate specific landforms and regions for study. DEM data for 7.5-minute units correspond to the USGS 7.5-minute topographic quadrangle map series for all of the United States.

The USGS National Elevation Dataset (NED) has been developed within the last 10 years by merging the highest-resolution, best quality elevation data available across the United States into a seamless raster format (USGS, 1999). The NED is designed to provide national elevation data in a seamless form (not arranged by quadrangles) with a consistent elevation unit, datum, and projection. This dataset fulfills the USGS effort to provide 1:24,000-scale DEM data for the conterminous United States and 1:63,360-scale DEM data for Alaska. Data corrections are made during the NED assembly process to minimize artifacts, permit edge matching, and fill areas of missing data (USGS, 1999). It is a living dataset that is periodically updated to incorporate the "best available" DEM data. Finally, NED data are available to download from the Internet using file transfer protocol or other standard distribution media.

A uniform data resolution or grid spacing is required for landform morphometric analyses. The 7.5-minute DEMs have ground spacing of 30 m ("1 arc-second") or 10 m ("1/3 arc-second"). The 10 m DEMs (NED 1/3 arc second) are the best, most accurate data available from the USGS and these were selected for this study.

Method and Procedure

The methodology consists of five steps: (1) Select regions of interest in the United States; (2) Acquire topographic (7.5 minute quadrangle) maps of each study area; (3) Select the coordinates of each specific region and acquire the DEM; (4) Acquire topographic and morphometric information based on the DEM and calculate statistics for key morphometric parameters; and (5) Check resolution and quality, complete data processing and organization, and produce graphical output.

More detail for each step follows:

1. We focused on obtaining at least one area in the United States that represents each particular geologic environment outlined in the beginning of the project. Each targeted study site is discussed in more detail in the section on Landforms and Study Sites.

2. Topographic (7.5 minute quadrangle) maps were obtained first and served as thumbprints for landscape identification and characterization. The USGS Map Locator and Downloader allows internet users the opportunity to find topographic maps by searching or navigating through an interactive map. Users can pan, zoom, change map view, order printed maps, or download a scanned map image in GeoPDF® format. We utilized the latter option. Map Locator and Downloader is available through the USGS Store (http://store.usgs.gov). This service became available in early 2008. The 7.5 minute topographic quadrangles were vital identifying the areas and gaining the needed UTM (Universal Transverse Mercator) coordinates for each specific region.

3. With the UTM coordinates acquired from the topographic maps, the DEMs were downloaded from the National Map Seamless Server (USGS) web site, http://seamless.usgs.gov. The USGS National Elevation Dataset (NED) has been developed within the last 10 years by merging the highest-resolution, best quality elevation data available across the United States into a seamless raster format (USGS, 1999). The NED is designed to provide national elevation data in a seamless form (not arranged by quadrangles) with a consistent elevation unit, datum, and projection. We were able to obtain high quality-high resolution 10 m data for each targeted study site. All acquired DEMs were organized and cataloged based on their terrain type. For processing, the GRID file that was imported from the USGS had to be converted into a DAT file that could be used in ENVI (version 4.5). Within the ENVI environment the coordinate system of the DEMs was changed from degrees (using the geographic latitude/longitude in the North America 1983 datum) to meters using the UTM projection coordinates in the North American 1983 datum. A STACK file was then saved for each study area. STACK files are single files that contain all the different coordinate, topographic, and formatting data needed from the DEM. Rather than recollecting the information each time the file is opened; it is saved in a STACK file in a ready-to-use format. With the STACK files ready and organized, the Regions of Interest (ROI), or Area of Interest (AOI), were defined. The ROIs were the specific regions of focus within the DEM, such as the actual impact crater walls and then expanding out to the crater floor and immediate surroundings at Meteor Crater, Arizona.

4. Based on the correct DEM coordinates explained above, the data can be collected and organized, respectively. At the beginning of this project and after reviewing the selected environments or terrain, it was our objective to capture as much as the characteristic terrain or landform as possible. The minimum/maximum, mean, and standard deviation was collected for slope, elevation, slope aspect, and drainage density. After reviewing the data, we focused on slope, aspect, and elevation; and the minimum/maximum, mean, and standard deviation of each were preserved in the STACK file. Drainage density was abandoned due to time constraints.

5. Each 10 m DEM was integrated into the ENVI 4.5 environment to analyze topographical relationships. Statistical evaluation and analysis was conducted with Kaleidagraph software (version 4.0). Both of these software packages aided data collection, organization, and classification. Data were output in graphical format (plots) through Kaleidagraph in order to compare the various landforms and their geomorphometric statistics.

Spatial Analysis

Geostatistical terrain analysis was conducted on controlled areas across each DEM. Each area of interest or gridded search area was square in configuration. Small target areas were selected to capture the detail of smaller landforms (e.g., dunes), while larger areas were selected to examine more regional characteristics (e.g., ridge-and-valley tectonic terrain). Because of the 10 meter NED cell size (pixel), the smallest area of interest measured 50 × 50 meters (Table 1). Measurements were not made for such landforms as small dune fields or giants current ripples once the spatial area greatly exceeded the region occupied by the landform.

Table 1. Dimensions and Characteristics of Areas of Interest

Dimensions (in pixels)	Total Pixels	Area (m^2)
5 × 5	25	250
10 × 10	100	10,000
15 × 15	225	22,500
50 × 50	2500	250,000
100 × 100	10,000	1.0×10^6
500 × 500	250,000	2.5×10^7
1000 × 1000	1,000,000	1.0×10^8

Landforms and Study Sites

A wide selection of landform types were examined for morphometric analysis. Although seamless 10 meter NED data were used, the 7.5-minute topographic quadrangle map names were retained for identification purposes. For eolian dunes, Big Dune (Big Dune quadrangle) is a small dune field composed primarily of transverse and star dunes in the Amargosa Desert of Nevada. A second eolian site was selected (Liberty, Colorado) to include Great Sand Dunes National Monument. Camas Prairie (Montana) and West Bar (Washington) were selected because they feature giant current ripples from the Channeled Scabland floods. Along the Gulf of Mexico shoreline, the Indian Pass (Florida) quadrangle was selected because it has beach ridges. The Y U Bench NE quadrangle (Wyoming) contains two fluvial terraces: Y U Bench and Emblem Bench.

The Corydon East quadrangle in southern Indiana was selected because it is covered by numerous sinkholes and other classic karst features. Enders, Pennsylvania, hosts ridge-and-valley terrain while Havasupai Point, Arizona, displays cliff-and-bench topography of the Grand Canyon. Hummocky topography can be found in the Little Prairie quadrangle of Wisconsin. A large moraine and numerous kettles are the prominent glacial landforms in this quadrangle. Loggers Lake quadrangle in the Mark Twain National Forest of Missouri features a dendritic drainage pattern. The Wapi lava flow of the Snake River Plain, Idaho, covers the Rattlesnake Butte quadrangle. A pediment dominates the arid landscape of the Sacaton quadrangle in Arizona.

Mauna Loa volcano (Mauna Loa quadrangle, Hawaii) was selected to represent the upper slopes of a large shield volcano. For planetary applications, the Meteor Crater quadrangle in Arizona was chosen as an example of an impact crater. Mitten Buttes quadrangle in Monument Valley along the Arizona-Utah border was selected as an example of mesas and buttes. Drumlins are another type of landform related to glacial processes. As an example of these elongated hills, the Sodus quadrangle near Lake Ontario, New York, was chosen for study. Time constraints limited the study to these quadrangles and their respective 10 meter NED.

Results

Geomorphometric analysis focused on two parameters: mean slope and topographic texture. Topographic texture is defined as the standard deviation of elevation and serves as a measure of local relief

or surface roughness. Parameters describing aspect and dissection (stream density) are not presented at this time.

In Figure 1, the mean slope for small eolian dune fields is greater than the other landforms displayed in the first figure. Big Dune is a smaller dune field than the Great Sand Dunes National Monument; therefore, the mean slope consistently decreases and begins to be dominated by the adjacent terrain when the area of interest is approximately 1 × 1 kilometer. The smaller areas of interest are able to capture individual dunes and their steep slip faces, whereas larger areas contain a greater percentage of flatter, interdune corridors and surrounding sand sheets. This result was anticipated, but can now be identified and quantified.

The topography of Y U and Emblem Bench reflects the varying flat terrace surface versus the steeper, surrounding fluvial banks. Giant current ripples and beach ridges maintained low mean slope values across all spatial scales.

Figure 2 displays the topographic texture of the landforms described in Figure 1. The Indian Pass (Florida) beach ridges show very little variation in elevation for each measurement. This is explained by the limited range in topography found along the Gulf of Mexico shoreline. The other landforms show an increase in standard deviation of elevation as the spatial area increases. This is because of area of interest is not flat but often contains a regional slope itself. For example, the fluvial terraces are in a mountainous area of Wyoming in which elevation is naturally decreasing downstream. Furthermore, as the measurement area increases, adjacent or neighboring landforms may become more influential. In future calculations this bias may be normalized or mitigated.

The mean slope values for the Grand Canyon (Havasupai Point, Arizona) and ridge-and-valley terrain (Enders, Pennslyvania) remain consistently high at each spatial scale (Figure 3). The dendritic drainage pattern seen in the Loggers Lake (Missouri) quadrangle displays a fractal characteristic such that it is suggestive of being similar at all scales. This is anticipated for dendritic character. Karst, lava flow, and pediment examples each had low mean slope values.

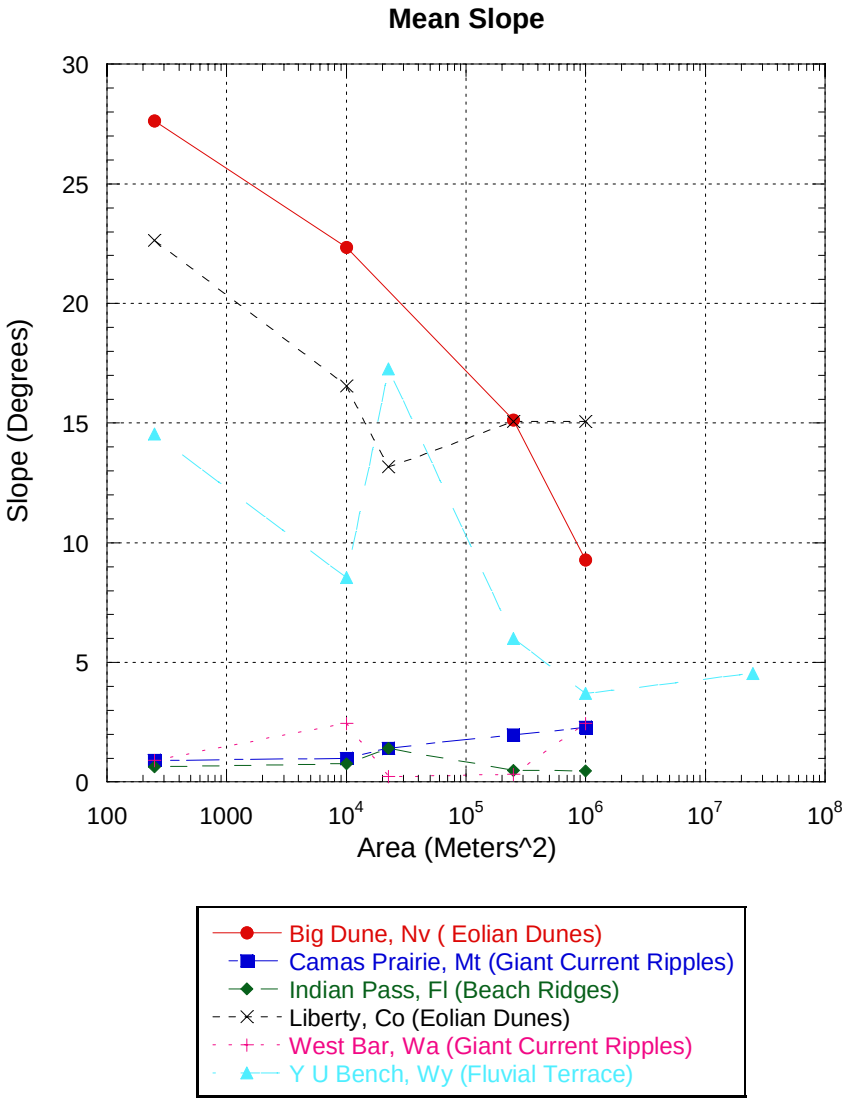

Figure 1. Mean slope angle (degrees) for the first set of landforms.

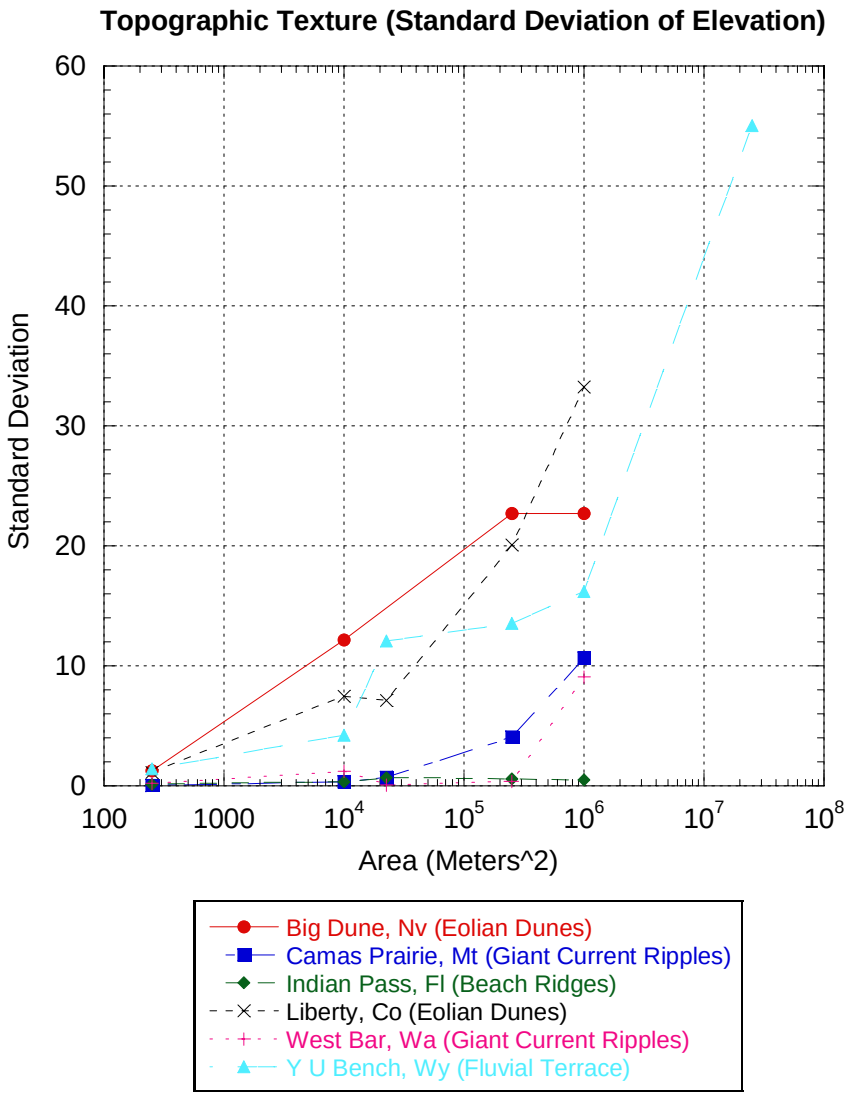

Figure 2. Topographic texture (standard deviation of elevation) for the first set of landforms.

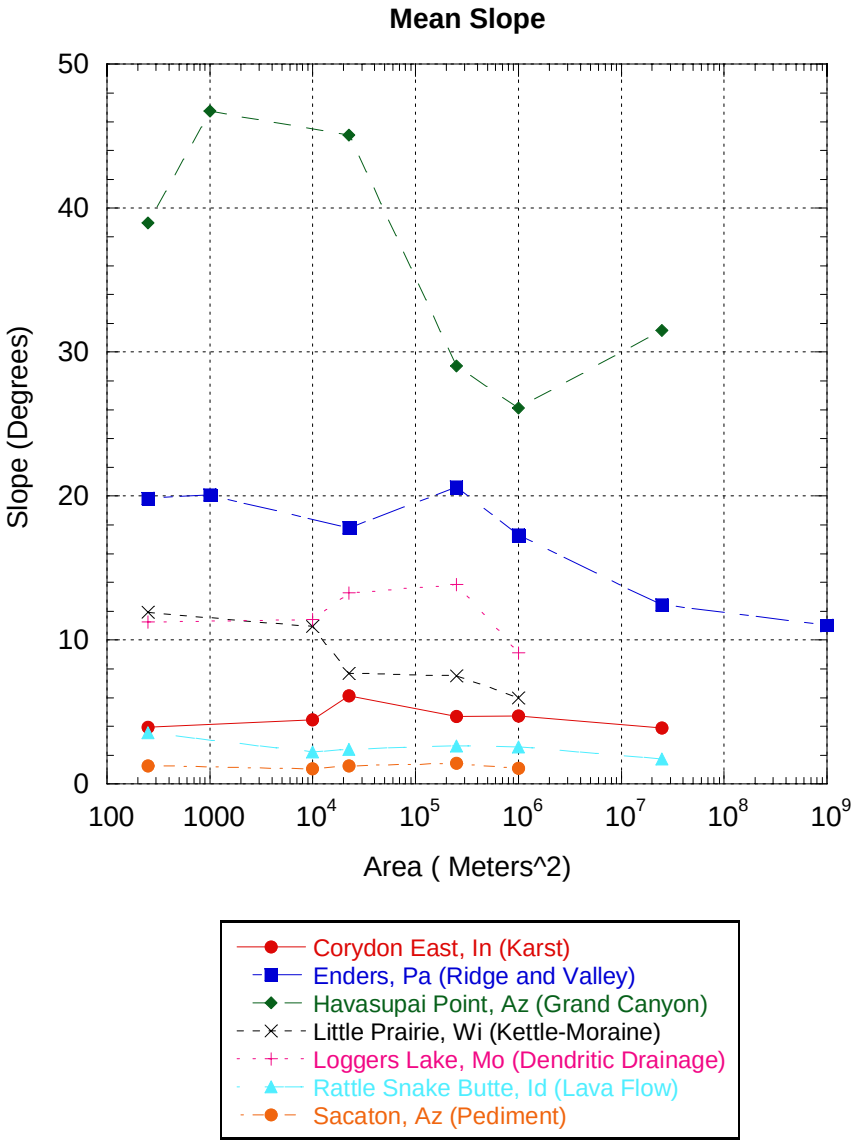

Figure 3. Mean slope angle (degrees) for the second set of landforms.

Figure 4 displays the large variation in relief seen at the Grand Canyon, Arizona. Numerous sinkholes and other karst features (Corydon East, Indiana) did not display an anticipated rough or hummocky topography at the smaller areas of interest.

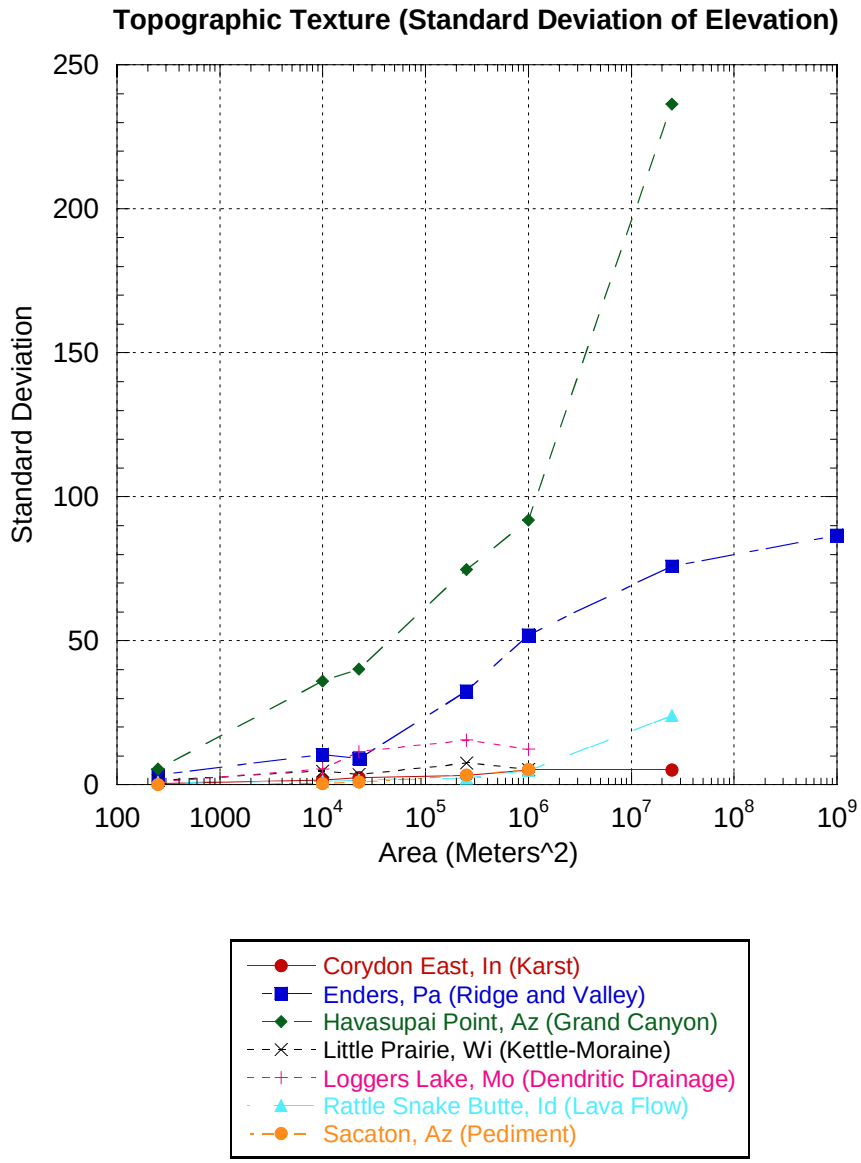

Figure 4. Topographic texture (standard deviation of elevation) for the second set of landforms.

Several mesas and buttes are included in the areas of interest for the Mitten Buttes quadrangle (Arizona-Utah). This causes the variation in mean slope seen in Figure 5. Meteor Crater, Arizona, contains steep interior crater walls, but the floor and exterior rim are much flatter. The Wapi lava flow (Idaho) and large Mauna Loa shield volcano (Hawaii) both maintain their mean slope angle across each spatial area of measurement. Figure 6 includes the topographic textures for the landforms listed in Figure 5 and in general shows an increase in standard deviation of elevation as the spatial area increases.

Discussion

Digital elevation models can help classify terrains and landforms on other planets. Although the work is in process, this method for morphometric analysis is being applied to the planet Mars. The assortments of other GIS-based maps (hillshade, relief, drainage density, etc.) are useful compliments to tools for mapping geologic environments. Whether the objective is to produce generalized regional maps for structural analysis, as was done for this study, or very specific and detailed maps, the 10 meter DEM and GIS maps reveal the true landscape and features with much clarity. This study recommends the use of 10 meter DEMs to clearly visualize and analyze topographic characteristics.

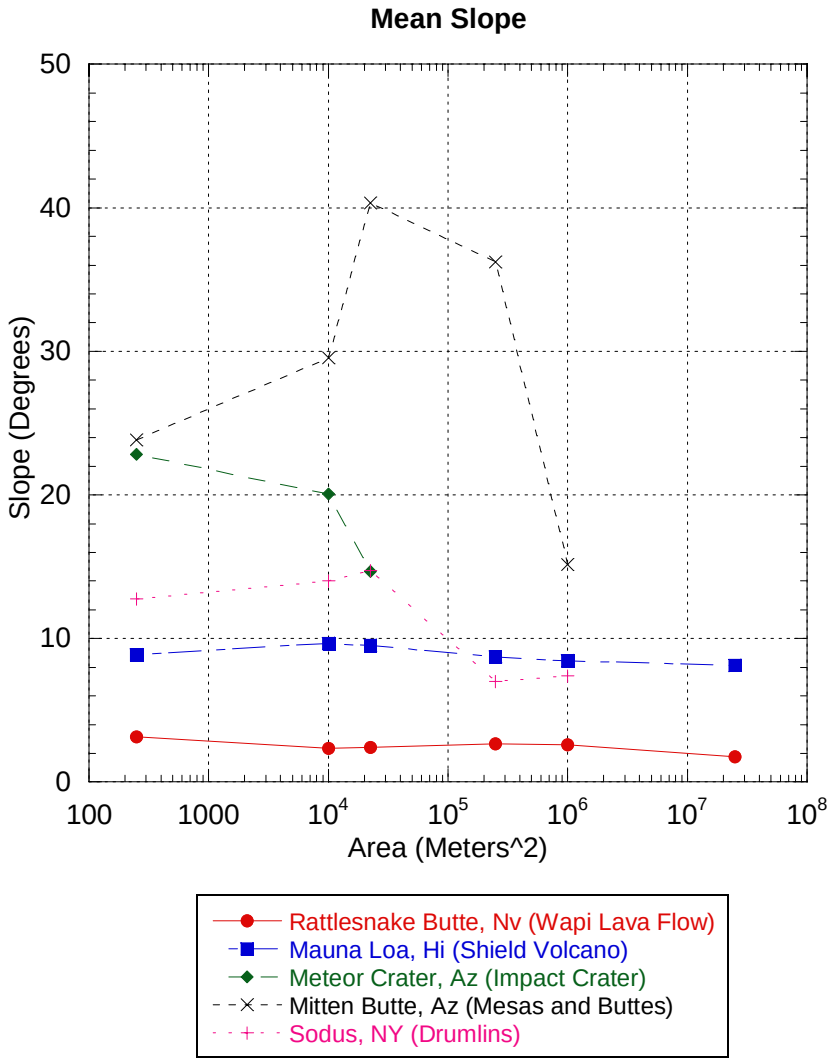

Figure 5. Mean slope angle (degrees) for the third set of landforms.

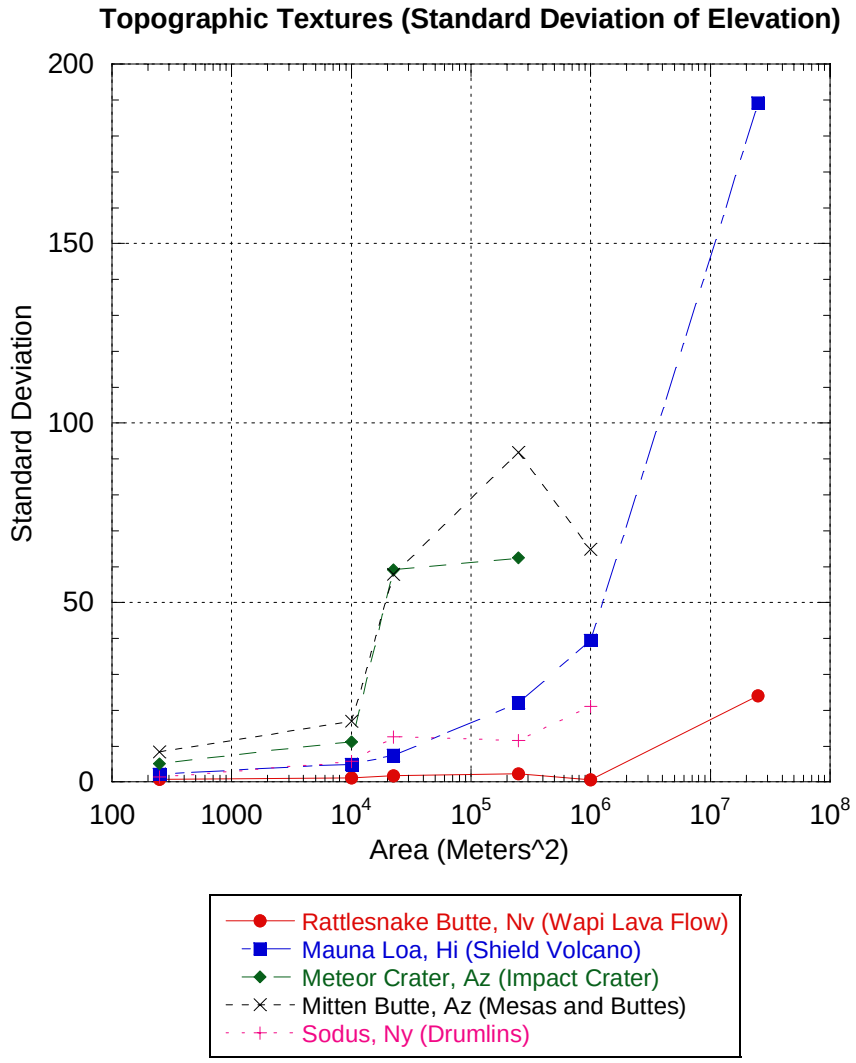

Figure 6. Topographic texture (standard deviation of elevation) for the third set of landforms.

Conclusion

Digital elevation models (DEMs) were utilized to conduct a geostatistical terrain analysis of common fluvial, volcanic, tectonic, and eolian landforms. The quantity and quality of data permitted by 10 meter Digital Elevation Models shows how straightforward it is to use once acquainted with the preferable software. Obtaining and processing the data was made easier because of the simplicity and supportive software used: ENVI 4.5 and ArcGIS. This study endorses the use of 10 meter DEMs to define, characterize, and read topographic sections whether large or small scale. For example, eolian dunes, cliff-and-bench topography of the Grand Canyon, mesas and buttes, and ridge-and-valley topography exhibit high mean slope values that are discernable at various spatial scales from other landforms or terrain types. A self-similar or fractal pattern was observed for dendritic drainage, although other study targets also displayed this characteristic. More morphometric analyses will be conducted in the future, including the potential application to digital topographic datasets from the planet Mars.

References

Guth, P.L. Eigenvector Analysis of Digital Elevation Models in a GIS: Geomorphometry and Quality Control. In *Concepts and Modeling in Geomorphology: International Perspectives*, Eds. I. S. Evans, R. Dikau, E. Tokunaga, H. Ohmori and M Hirano. TERRAPUB, Tokyo. pp 199-220. 2003

USGS (U.S. Geological Survey). National Elevation Dataset. Fact Sheet 148-99. September 1999.

USGS (U.S. Geological Survey). US GeoData Digital Elevation Models. Fact Sheet 040-00. April 2000.

Preliminary Report:

Formal Stratigraphic Nomenclature for the Kainer Formation San Marcos Platform and Arch, Texas

by
Mark Childre

Minority Opportunities for Research Experience
Science Program

16 January 2009

Sponsored by: Lance L. Lambert
Department of Geological Sciences
University of Texas at San Antonio

Allan K. Clark
United States Geological Survey
Texas Water Science Center
San Antonio, TX

Formal Stratigraphic Nomenclature for the Kainer Formation San Marcos Platform and Arch, Texas

Abstract

Lower Cretaceous strata of north Texas have been formally subdivided following the North American Stratigraphic Code (NASC) requirements for some time. However, in south Texas more informal descriptive units have historically been used with success because the paleoenvironment was a stable, shallow, lagoonal region protected behind the Stuart City Reef trend. As more detailed studies are conducted, the stratigraphy, hydrogeology, karst, and structure of the Edwards Group and its equivalents are often confused by the misleading informal nomenclature, which often used descriptive lithologic terms for member names. Formal stratigraphic nomenclature is needed to more precisely correlate increasingly finer subdivisions of the Edwards Aquifer with equivalent shelf-edge deposits of the Devil's River trend and the epicontinental Maverick Basin. Better correlations beyond the immediate region, such as with Lower Cretaceous strata in trans-Pecos and north Texas, should be another positive result because of concurrent sequence stratigraphic analysis.

The objective of my research is to measure potential type sections, describe the lithology, and interpret the sequence stratigraphy for each of the members for the Kainer Formation according to the NASC. The data collected will ultimately result in a formal stratigraphic nomenclature based on properly measured and described reference sections with geographically derived names.

1. Introduction

The Edwards Aquifer of south-central Texas is noted as one of the most permeable and productive aquifers in the United States. The porosity and permeability of the Edwards Aquifer is related to stratigraphy and to selective leaching of particular strata. The strata were products in the freshwater zone as water moves from the fractures into beds of collapsed breccias, wackestones, and rudistid grainstones. Many of the facies have relatively large intrinsic permeability (Maclay and Small, 1984). The Edwards Group is also an important target for oil exploration in the Gulf Coastal Plains south of San Antonio and the source rock for the Edwards Aquifer, which is recharged through outcrops in the Balcones Escarpment.

The confining features limit the Edwards Aquifer vertically between the relatively impermeable argillaceous facies. The Maverick Basin to the west, Comanche Shelf to the north, and North Texas-Tyler Basin strata surround the San Marcos platform and Devil's River trend.

Of primary importance for this paper is the San Marcos platform which is the location that formal stratigraphic measurements were made. The data and analysis from this report will provide data for the abstract "Formal stratigraphic nomenclature for the Edwards Group in south Texas" by Lambert and Clark (2005).

The primary emphasis of this paper is to present the measured sections and lithology for the members of the Kainer Formation which compose the lower Edwards Group within the San Marcos platform. Formal names will replace the informal designations for each member according to the North American

Stratigraphic Code requirements (Appendix E). Numerous rock samples were collected from the measured sections and were cut into rock slabs and thin sections defining the lithology.

2. Geologic History

The features that surround the San Antonio region had composition of reefs and basins, both exposed and subsurface. The Lower Cretaceous rocks that comprise the Edwards Aquifer were deposited upon the landward margin of the Comanche continental shelf which was sheltered from the storm waves and the deep ocean by the Stuart City Rudistid Barrier Reef trend in the ancestral Gulf of Mexico, forming the offshore margin of the Central Texas platform. Subsidence across a tectonic hinge line that skirted the southern edge of this carbonate shelf kept most of the Edwards Aquifer submerged within a curved bank of reefal growth known as the Devil's River trend. Greater rates of subsidence south of the hinge line caused fundamental differences between rocks deposited within the Devils River trend and those deposited in deeper water inside the Maverick Basin. These geologic features are illustrated in Figure 2 (Clark et. al., 2006).

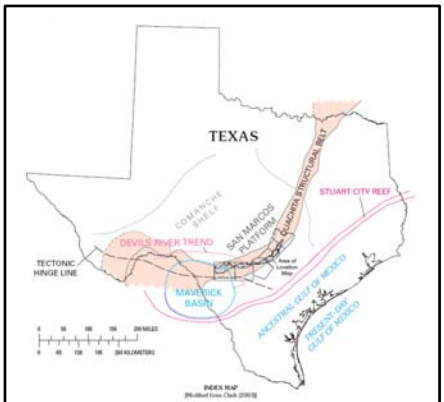

Figure 2: Paleogeographic and structural features in Texas associated with the Edwards Aquifer (Clark, 2003)

The San Marcos platform became the site of deposition with cyclical transgressions, maximum flood stages, and high system tracts between 107 my and 103 mya (Albian Age, Cretaceous Period) in the San Antonio area. Regressive events occurred following subaerial exposure at the end of the Edwards Group depositional event in the early and middle time range of the Late Cretaceous period. This is described with more detail in Table 1 (Maclay, 1995).

The final stage was the erosional hiatus of evaporite sedimentation cycle, deposited on the hot supratidal flats of the San Marcos platform. These deposits were wholly or partly removed by circulating ground waters and collapsed breccias of high porosity and permeability. Subaerial erosion removed about 100 ft or more of the deposits and resulted in karstification (Maclay and Land, 1988).

Subsidence of the Gulf Coast Region continued throughout the late Oligocene and early Miocene Epoch. This renewed extensional deformation occurred from about 30 ma to 15 ma resulting in the Gulf of Mexico we know today (Ferrill et. al., 2005) and the formation of the Balcones Fault Zone. The Edwards Aquifer is located along the Balcones Escarpment, a topographic feature that separates the Edwards Plateau and the Texas Hill Country from the Gulf Coastal Plain.

3. Stratigraphic History

Rose (1972)

Discovery of oil at Luling in 1922 promoted the extension of north Texas nomenclature southward into the area of the San Marcos platform. In north Texas, the Edwards Formation replaced the previous nomenclature defined in the 19th century. The Edwards was a thick mass of resistant limestone which also composed the Edwards Plateau of southwest Texas (Rose, 1972).

In the 1950's (Van Siclen, 1958, fig.10), a regional, widely traceable, argillaceous, compact limestone was recognized in the middle of the Edwards Formation. The thin bed was assigned the nomenclature Regional Dense marker by Knapp (1962). Tucker (1962) then recognized that the apparently absent Kiamichi Member could be traced subsurface to the Regional Dense member (informal) south of Travis and Bastrop Counties (Rose, 1972).

The nomenclature assigned to the Edwards Formation in north Texas was unacceptable in southwest Texas. Based on the type section from the petroleum cores in Karnes County, the Edwards B-zone was assigned the 250 feet thick Kainer Formation and the Edwards A-zone was given the nomenclature of the 180 feet thick Person Formation. Conceptually, the north Texas remained the type area of the Edwards Formation, despite its southwest Texas place name (Rose, 1972). The Edwards in southwest Texas became a "group" containing the Kainer and Person Formations.

For the Edwards Group, two members of the seven were previously named by Barnes (1944) and Knapp (1962) prior to Rose (1972) research. First, Barnes (1944) investigated the gypsum horizon in Gillespie County, assigning the formal nomenclature Kirschberg Member. Then, Van Siclen (1958) and Knapp (1962) recognized and named a thin, widely traceable unit, called the Regional Dense member, which separates the upper and lower Edwards Group. Rose (1972) identified and named the remaining members informally for the Edwards Group from subsurface and surface investigations. Rose (1972) made no attempt to define the specific lithology in the type section for the Balcones Escarpment while Maclay and Small (1976) measured the broad homocline interrupted by the Balcones Fault Zone, still using the informal nomenclature established by Rose and others.

Following Barnes (1944) and Knapp (1962) identification of nomenclature for the Kirschberg and Regional Dense (respectively;) Rose (1972) completed the informal definition based on lithology for the Basal Nodular, Dolomitic, Grainstone, Collapsed, Leached, Marine, and Cyclic members. Extensive cores, samples, and electric log control from a linear trend of oil and gas fields in Atascosa, Karnes, and Gonzales Counties provided the subsurface core data. Type sections of Edwards Group outcrops were measured and sampled for correlation near the Kerrville area. The relations were applied to the same rocks throughout the area of the San Marcos platform, where control is sparsely defined (Rose, 1972).

Shown in Figure 3, Rose performed evaluations for three regions. These locations were southeast and northwest of the Balcones Fault Zone:

1) The subsurface investigation began with detailed examination of cores from the Fashing-Person trend of oil fields south of Bexar County. Cores were slabbed and etched. Interlocking electric log correlation provides documentation of the extension of boundaries throughout the San Marcos platform area.
2) Cores were studied from wells throughout the San Marcos platform. Cores and sample data with electric log correlations were analyzed.
3) The eastern Edwards Plateau is limited on the north by the Llano Uplift and on the south and east by the Balcones fault zone.

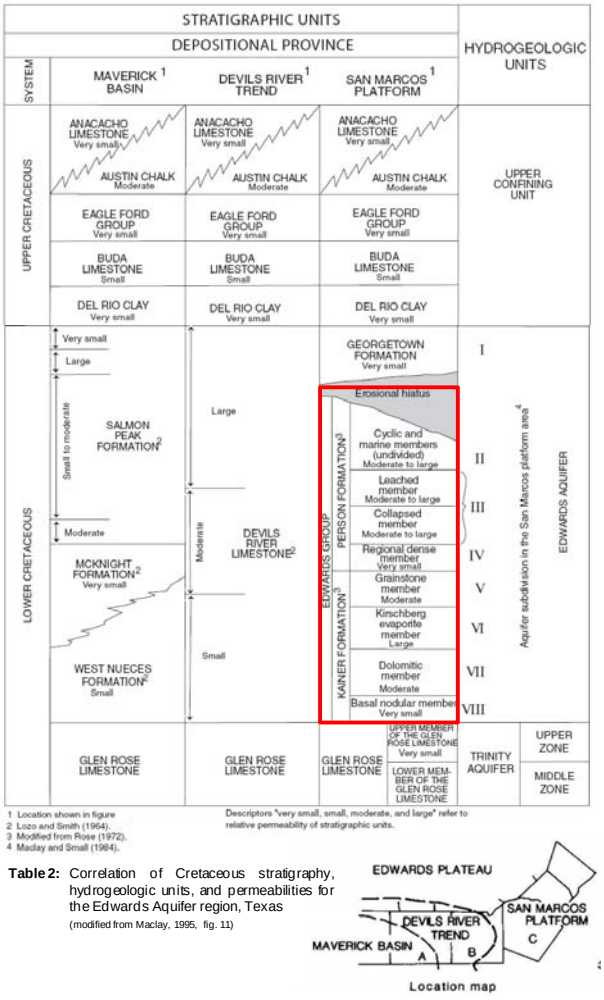

Table 2: Correlation of Cretaceous stratigraphy, hydrogeologic units, and permeabilities for the Edwards Aquifer region, Texas (modified from Maclay, 1995, fig. 11)

Outcrops were evaluated in the hill country counties north and west of both San Antonio and the Balcones Fault Zone. Type sections of the outcrop were also measured and sampled (Rose, 1972).

The Kainer Formation is typically 300 feet thick but varies. It can range between 250 and 400 feet thick. The Person Formation is typically 200 feet thick but can range between 180 and 250 feet thick (Maclay, 1995).

Maclay and Small (1976) used the informal definitions while establishing the aquifer subdivisions. There are 8 subdivisions for the Edwards Aquifer. The 1st subdivision is the confined beds of the Georgetown Formation, and the 2nd through the 8th were assigned to the Edwards Group. In consideration of petroleum drilling practices, the Georgetown is assigned to the aquifer but is impermeable and is actually a confining bed.

There were four depositional provinces that were formed during the Early Cretaceous time. These provinces were the Central Texas platform (or Comanche continental shelf), Maverick Basin, Devil's River trend, and San Marcos platform all of which were west of the Stuart City Reef. The geology of the San Marcos platform, Devil's River trend and Maverick Basin are illustrated in Figure 2 (Clark et. al., 2006).

The Maverick Basin is the depositional province that was confined between the reef to the south and shallow water or tidal flats north and east. The Devil's River trend is adjacent Maverick Basin and is a complex consisting of marine, supratidal, and reefal deposits (Maclay and Small, 1984).

The Edwards Group consisted of porous dolomite and limestone accumulated on the Comanche shelf as shallow marine, intertidal, and supratidal deposits. The Edwards thickness ranges from about 1000 ft near the Maverick Basin and thins northeastward. The rock facies is conformable with the Glen Rose Formation below and disconformable with the Georgetown Formation above. The Edwards Group outcrops parallel with the Balcones Fault Zone (Rose, 1972).

Maclay and Small (1976)

Maclay and Small (1976) expanded the research conducted by Rose (1972). The primary purpose of Maclay and Small (1976) is to describe the geology and

porosity of the rocks of the Edwards Aquifer and to provide the preliminary interpretations of the borehole geophysical and laboratory data.

There are several observations and analyses that should be considered while working with the Edwards. All of the major springs in the San Antonio area occur on major faults, common throughout the area. The ground-water flow toward San Marcos Springs is relatively unobstructed, and the direction of flow is controlled by the permeability of the strata (Maclay and Small, 1976).

The stratigraphic units of the Edwards Group that crop out on the Edwards Plateau have been mapped by Rose (1972) as the Segovia and Fort Terrett Formations. The outcrops are correlated with the Person and Kainer Formations using subsurface rock samples and geophysical logs (Rose, 1972).

The dominant structural feature of the Edwards Group in south Texas is a broad homocline that extends from nearly flat-lying beds on the Edwards Plateau to steely dipping beds in the deep subsurface of the Gulf Coastal Plain. The homocline is interrupted by the Balcones Fault Zone (Maclay and Small, 1976).

The Balcones Fault Zone is the result of stresses built up in the rocks of the Edwards Group by the weight of gradually accumulating sediments in the ancestral basin of the Gulf of Mexico and by upward forces developed on the San Marcos platform, which is a subsurface extension of the Llano uplift. Figure 4 identifies the major normal faulting in the San Antonio area (Maclay and Small, 1976).

Table 2 illustrates that the Edwards Group of the San Marcos platform is equivalent to the Devil's River Limestone; and the West Nueces, McKnight, and Salmon Peak Formations of the Maverick Basin The Edwards Aquifer is composed of water-bearing rocks in hydraulic continuity in the Georgetown Formation. The aquifer, the Edwards Group, and the Comanche Peak Formation, can be subdivided into eight informal units within the San Marcos platform. The Edwards Aquifer is permeable in the hydrogeologic units II, III, V, VI, and VII, shown in Table 2. The I, IV, and VIII hydrogeologic units have small matrix permeability except where karst features exist (Maclay and Small, 1976).

Porosity is evident in several forms. Voids or molds result from the dissolution of fossils forming honeycombed rock. Many large molds are poorly connected and contribute little in the effective porosity in the lower part of the aquifer. Intraparticle porosity, within the allochem, is another common type of porosity in the Edwards Aquifer. Selective leaching is readily identifiable by the moldic porosity formed from the leaching of fossils. Indiscriminant leaching occurs along some fractures (Maclay and Small, 1976).

Important diagenetic processes include dolomitization, recrystallization, leaching, cementation, and replacement. The process of recrystallization of dolomite to calcite or spar is termed dedolomitization which generates a dense, nonporous rock (Maclay and Small, 1976).

Six test holes were drilled and cored by the Texas Water Development Board (TWDB) and two test holes were drilled and cored by private drilling companies under contract with the USGS

4. Tectonic History

Figure 5 illustrates a geologic cross section across the Balcones Fault Zone in Bexar County, Texas using the well locations shown in map view in Figure 6

(Maclay, 1995). Figure 7 illustrates the correlation between the Maverick Basin, San Marcos platform, and the North Texas-Tyler Basin.

The high permeability is a result of dissolution imprinted upon zones of weakness, such as fractures, faults, bedding plane partings, and stratigraphic features (Schindel et. al., 2007). Unconformable or paraconformal contacts occur within the Edwards Group representing periods of subaerial erosion and cavernous porosity (Maclay and Land, 1988).

5. Regional Structure

The top of the Edwards dips gently southeast at 3 to 4 degrees. Northwest of San Antonio, the Balcones monoclinal fault zone interrupts the dip with long antithetic and synthetic systems of en echelon normal faults.

The Person Field and Falls City fault zones comprise the (1**) Karnes trough**. Fashing-Person series of oil and gas fields lies along the upthrown side of the antithetic Person Field fault. A structural feature branches off the Karnes trough, passing westerly across Atascosa County, forming the (2) **Atascosa trough**. The (3) **Mexia fault system** is an ill-defined counterpart of the Atascosa trough, branching away from the Karnes trough, passing into northeast Texas. In Figure 5 the depositional patterns of Edwards and later rocks were profoundly affected by these three troughs, which were actively subsiding during the later part of the Early Cretaceous time (Rose, 1972).

The Edwards thickens southwestward to about 1000 ft near the Maverick Basin and thins northeastward by basinward thinning to zero ft in the north Texas – Tyler Basin. In the San Marcos platform, the Edwards Group consists of the Kainer and Person Formations. The Edwards is conformable with the Glen Rose Formation and disconformable with the Georgetown Formation above.

6. Depositional Environments

The shallow-water depositional model defines the environment as tidal flats (supratidal and intertidal), restricted shallow marine, open shallow marine, and open shelf for the Edwards Group. Certain textures, sedimentary structures, minerals, and faunal associations are characteristic of each environmental belt. The shallow marine depositional environment is outlined in Table 3 (Rose, 1972).

The end-members of the classification are usually distinctive and readily identified. 1-There is no inherent depth distinction between restricted shallow marine and open shallow marine. 2-The open shallow marine category can be subdivided into high- and low-wave energy categories. 3-A depth distinction is intentionally implied between the open shallow marine and open shelf categories (Rose, 1972).

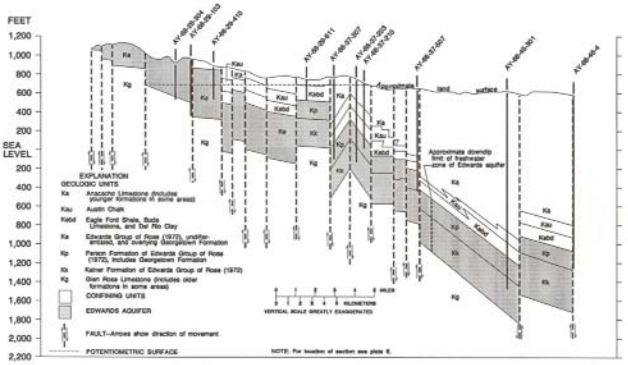

Figure 5: Hydrogeologic section *B-B'* through the Edwards Aquifer in Bexar County, Texas (Maclay, 1995)

Open Shelf deposits are dark to light, slightly argillaceous, non-dolomitic lime mud with diverse indigenous fauna including common pelagic foraminifera,

calcispheres, and fragile mollusks. Ammonites are also common. More robust bivalves and gastropods are abundant in shallower aspects of the environment. This is the common environment for the **Georgetown Fm** and the **Regional Dense member** (Rose, 1972).

Open Shallow Marine High-Wave Energy deposits are a light-colored, relatively coarse-grained, well sorted, chiefly bioclastic limestones containing a diverse fauna rich in algae, corals, and a variety of rudists but lacking pelagic foraminifera are the most common sediment type found in this environment. This environment produced the upper Devil's River Formation and the coarse-grained shelly units in the **Marine member** (Rose, 1972).

Open Shallow Marine Low-Wave Energy deposits are a light-colored, poorly sorted, muddy limestones rich in miliolid foraminifera, *Toucasia sp.*, *Monopleura sp.*, oysters, and snails lacking pelagic foraminifera. This sediment forms the **Grainstone** member (Rose, 1972).

Restricted Shallow Marine deposits are light-colored, poorly sorted, commonly burrowed, muddy limestone and dolomite rich in miliolid foraminifera, oysters, and snails. Generally, this marine environment is found in shelf interiors and in the lee of protective barriers that are common with the **Dolomitic, Leached, and Cyclic** members (Rose, 1972).

Tidal flat deposits are thin-bedded,pelleted micrite and dolomitized micrite. Fauna is limited to miliolid foraminifera, cerithid or turritellid snails, and oysters. Stromatolitic, mud cracks, root marks, bird's eye structures, exposure surface, "rip-up" clasts, thin collapse breccias, pseudomorphs after gypsum, burrows, and various channel features. Tidal flat is a combination of the supratidal and intertidal depositional environments. These tidal conditions are intermixed throughout the Edwards Group. Distinct tidal flat sequences have been recorded in the **upper Dolomitic, Collapsed, and Cyclic** members (Rose, 1972).

Evaporite-Dominated Supratidal Flat deposits are where gypsum and anhydrite crystals precipitated, grew and merged within soft dolomitized muddy sediments to form thick massive layers of admixed nodular gray gypsum and subordinate brown dolomite mud. The environment is analogous to the sabkhas of the Persian Gulf tidal flats. These evaporite-dominated sediments are localized over structural highs in the interior of the Central Texas platform. In part, the Kirschberg Member. represents the evaporite-dominated supratidal flat depositional environment (Rose, 1972).

7. Sequence Stratigraphy

The Upper Glen Rose Formation exhibits the characteristics of low, intertidal or supratidal, sea-level near the transition with the Basal Nodular member. Ripple marks have been observed near this transition in several locations throughout the San Marcos platform. Rapid transgression followed during the deposition of the Basal Nodular member (Chenault and Lambert, 2005).

Near the transition between the Glen Rose Formation and the Basal Nodular member, a transgressive system tract (TST-1) begins. The TST-1 continues into the Dolomitic member with high stand system tract (HST-1) occurring. During the upper Dolomitic member, progradation occurred, continuing into deposition of the Kirschberg Member, generating an evaporite-dominated supratidal flat. Fluctuating

water depths were common in both the Kirschberg Member and Grainstone member. The Grainstone member commonly has cross-bedding and ripple marks near the transition with the Regional Dense member A deeper depositional environment occurred where the rudists (*Toucasia sp.*) were identified in the Grainstone member, prior to the Regional Dense member (Chenault and Lambert, 2005).

The Regional Dense member resulted in deeper water and TST-2 was initiated. Within the upper part of the Regional Dense member, HST-2 occurred generating a Maximum Flood Stage (MFS). The Regional Dense member is slightly argillaceous and has non-dolomitic lime mud. After the HST-2 occurred, there was progradation into the thin-bedded, dolotimized micritic tidal flat of the Collapsed member (Chenault and Lambert, 2005).

Once again, the water depths were fluctuating throughout the Leached and Collapsed member and the Cyclic and Marine member. The water level varied from tidal flat, restricted shallow marine, and open marine with high energy wave action. An unconformity was formed during the late Cyclic and Marine member, eroding away approximately 100 ft of the Person Formation. The transgressive system tract (TST-3) submerged the outcrop during the Georgetown Formation deposition, continuing into the Del Rio Formation where a deep depositional environment was in place (Chenault and Lambert, 2005).

8. Analysis and Results

The possible type sections were identified by Allan Clark (USGS) during numerous field trips, analyzing the outcrop exposure, continuity, and accessibility. Three locations were identified and chosen based on these qualities. The specific type section locations are provided in Figure 8.

Cibolo Canyon. Type section 1 (GPS: N29.67189^{o} W98.38306^{o}) Basal Nodular and Dolomitic members.

Cibolo Canyon.Type section 2 (GPS: N29.66692^{o} W98.39076^{o}) Kirschberg Member measurement.

Eisenhower Park (GPS: N29.62468^{o} W98.57974^{o}) Dolomitic member Because of this faulting, the type section is not continuous and may not be used. Rock sample analysis from Eisenhower Park was used to supplement the Dolomitic carbonate petrology for this report.

Table 3: Classification of depositional environments
San Marcos Platform, Texas (Rose, 1972)

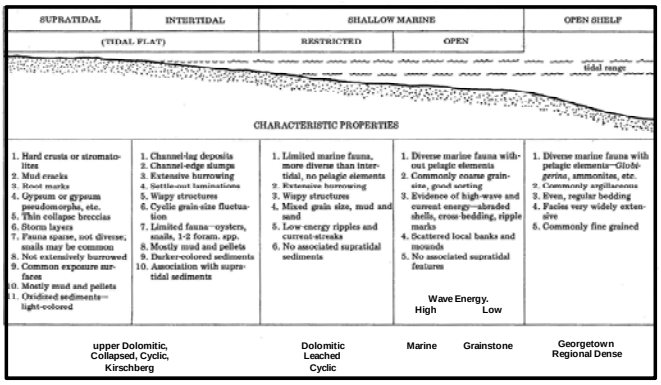

High Mountain Ranch Type section 1 (GPS: N29.51416^{o} W98.91036^{o}). Grainstone and Regional Dense members

The type section was measured using a Brunton 5008 compass, Jacob's staff, and a tripod. The data correlates well with other type section measurements in the San Antonio region. The stratigraphic column (Appendix A), and the carbonate petrology for each type sections are available for review in

Appendices B, C, and D (not included). The facies zones (FZ) and standard microfacies (SMF) shown in Appendix A are defined by Flugel (1982) and Wilson (1975). Below is a summary of these analyses for each member within the Kainer Formation with additional data for the Regional Dense Member (Person Formation).

Basal Nodular member

The base of the Kainer Formation is the Basal Nodular member and is hydrogeologic subdivision VIII. Considered regionally to be a lower confining unit, it is locally water bearing through dissolution along bedding planes. The measured thickness at Cibolo Canyon is 32 feet with other analyses in the San Antonio area providing thicknesses between 20 and 70 feet overall. The Basal Nodular is generally of dense, shaley, clayey, fossiliferous, nodular limestone. Most of this member is burrowed mudstone to wackestone with minor lateral cavern development noted elsewhere at the surface and exhibits non-fabric selective porosity. Dolomite crystallization and stylolitic features were also observed. Black rotund bodies ("brb's") were identified in hand samples 5 ft from the base of the Basal Nodular member and the occurrence of miliolids, bivalves, and peloids was noted erratically scattered, generally, throughout the lower part of the member. Previous research was conducted by Clark (2003) and Stein and Ozuna, (1995).

Dolomitic member

The Dolomitic member lies atop the Basal Nodular and had a measured thickness of 99 feet.. This hydrogeologic subdivision VII component is mostly composed of crystalline limestone, wackestone, and packstonene, and layers of variably-burrowed mudstone. Chert nodules and thin discontinuous beds of chert are scattered throughout the subdivision. A bed of gastropods (*Turritella sp.*) were identified while surveying the Eisenhower Park type section and was confirmed elsewhere in the park at the base of the Dolomitic member. Rudists, commonly *Toucasia sp.*, have been collected in other studies and have been noted to be common near the top of the member. Cavern development is directly related to faults, fractures, and bedding planes. Exhibits non-fabric selective porosity except where solution along bedding planes yields water. The massively bedded dolomitic unit weathers to light gray in outcrop. Stein and Ozuna (1995), Maclay and Small (1976), and Clark (2003) have previously researched and measured this member.

Kirschberg evaporite member

From stratigraphic measurements and hand samples, the Kirschberg evaporate member (hydrogeologic subdivision VI) measured 53 feet thick and is composed, mostly of highly altered crystalline limestone, chalky mudstone, with chert nodules and lenses. The Kirschberg is identified by boxwork voids with neospar and travertine framing. Extensive cavern development throughout the unit makes the Kirschberg evaporite one of the most porous (mostly fabric-selective porosity) and permeable members of the Kainer Formation. No common fossils are identified within this unit. Previous work was conducted by Stein and Ozuna (1995).

Grainstone member

The Grainstone member (hydrogeologic subdivision V) overlies the Kirschberg evaporite member and is the uppermost subdivision of the Kainer Formation. The Grainstone member measured 58 feet thick at the High Mountain Ranch type section. The Grainstone member contains white, thickly cemented, miliolid and

ooliticl grainstone with mudstone to packstone common throughout with calcite crystallization and replacement. Chert nodules exist near the Kirschberg and Grainstone contact boundary. Cross-bedding and ripple marks can be found near the top in the grainstone (Landa Park, Stone Oak). Cavern development is rare to nonexistent throughout the unit. Classified as having non-fabric selective porosity and low permeability as a result of recrystallization.. Locally, in other studies *Touscasias* are common near the top of the member. Bivalves, miliolids, peloids, and gastropods are common throughout. Previous research was conducted by Stein and Ozuna (1995), Maclay and Small (1976), and Clark (2003).

Regional dense member

The Regional dense member (hydrogeologic subdivision IV) is the lowermost subdivision of the Person Formation. This member provides an excellent marker bed and was included in this survey. It consists of dense, argillaceous mudstone and wackestone, and is persistent throughout the San Marcos platform and is considered a major barrier to vertical ground-water flow in the Edwards Aquifer. It is identified by its characteristics of very light tan color, argillaceous limestone lithology, and wispy iron-oxide stains. Bivalves, scaphopods, peloids, and ooids are common. 'The occurrence of wispy iron-oxide stains statesd that the unit is susceptible to erosion. Very few caverns have been found, but vertical fracture enlargement does occur locally in this non-fabric selective porosity, low permeability unit. The thickness in Cibolo Canyon is 20 feet. Previous work has been conducted by Small and Hanson (1994), Maclay and Small (1976), and Clark (2003).

9. Conclusions

The research work identified two possible locations for a formal type section. The High Mountain type section measurement for the Grainstone and Regional Dense members is continuous with good rock exposure and is recommended as a formal type section location. Cibolo Canyon provides an excellent outcrop for the Basal Nodular and Dolomitic members. These members were accurately measured. Adequate hand samples were not obtained for the Dolomitic member, so rocks from Eisenhower Park were analyzed for the base. The stratigraphic column for the Dolomitic member was composed from original work from a road cut at San Antonio Ranch (GPS: N29.59929^{o} W98.71541^{o}). This type section was measured but not used because the Dolomitic and Kirschberg contact could not be identified.

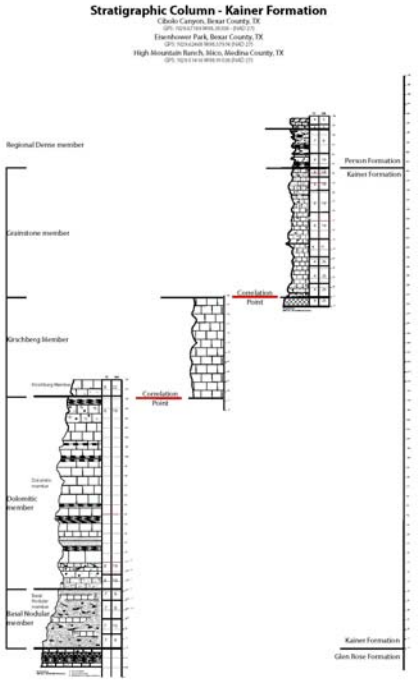

The Cibolo Canyon area provides an excellent location for measurement of the Basal Nodular, Dolomitic, and the Kirschberg members. Negotiations need to be.continued so that access to the property may be obtain so that this location may be a formal type

section.

Formal nomenclature is recommended that will replace the informally named member. Table 4 suggests geographic names that meet the NASC requirements and should be submitted for internal review in the future.

Member Unit	Formation	Formal Nomenclature
Regional Dense	Person	Cedar Hill Member
Grainstone	Kainer	High Mountain Member
Dolomitic	Kainer	Bat Cave Member
Basal Nodular	Kainer	Cibolo Canyon Member

Table 4: Formal stratigraphic nomenclature for the Kainer Formation members and the base of the Person Formation

References

- Barnes, Virgil Everett; 1944; Gypsum in the Edwards limestone of central Texas; Publication University of Texas, Bureau of Economic Geology, Report: 4301, pp.35-46.
- Chenault, Dena S.; Lambert, Lance L.; 2005; Sequence correlation of the mid-Comanche Series, South Texas region; Bulletin of the South Texas Geological Society, vol.46, no.3, pp.13-30.
- Clark, Allan K.; 2003; Geologic framework and hydrogeologic characteristics of the Edwards Aquifer, Uvalde County, Texas; U.S. Geological Survey, Water Resources Investigations Report 03-4010; 17 pp., 1 sheet.
- Clark, Allan K.; Faith, Jason R.; Blome, Charles D.; Pedraza, Diana E.; 2006; Geologic Map of the Edwards Aquifer In Northern Medina and Northeastern Uvalde Counties; U.S. Geological Survey, Open-File Report 2006-1372; 22 pp.
- Ferrill, David A.; Morris, Alan P.; and Waiting, Deborah J.; 2005; Structure of the Balcones Fault System and architecture of the Edwards and Trinity Aquifers, South-Central Texas; Geological Society of America South-Central Meeting Spring 2005; 39 pp.
- Flügel, E., 1982, Microfacies Analysis of Limestones: New York, Springer-Verlag, 633 pp.
- Knapp, R W; 1962; Person Field; Transactions - Gulf Coast Association of Geological Societies, vol.12, pp.199-204.
- Lambert, Lance L.; Clark, Allan K.; 2005; Formal stratigraphic nomenclature for the Edwards Group in South Texas; Geological Society of America, vol.37, no.7, pp.214-215.
- Maclay, R. W. and Small, T. A.; 1976, Progress Report on Geology of the Edwards Aquifer, San Antonio Area, Texas, and Preliminary Interpretation of Borehole Geophysical and Laboratory Data on Carbonate Rock; U. S. Geological Survey Open-File Report 76-627, 65 pp.
- Maclay, R. W. and Small, T. A.; 1984; Carbonate Geology and hydrology of the Edwards Aquifer in the San Antonio area, Texas; U. S. Geological Survey Open-File Report 83-537, 72 pp.
- Maclay, R.W.; and Land, L.F.; 1988; Simulation of Flow in the Edwards Aquifer, San Antonio Region, Texas, and Refinement of Storage and Flow Concepts; U. S. Geological Survey Water-Supply Paper 2336-A, 48 pp.
- Maclay, Robert W.; 1995; Geology and Hydrology of the Edwards Aquifer in the San Antonio Area, Texas; U. S. Geological Survey, Water-Resources Investigations Report 95-4186, 64 pp.
- Rose, Peter R.; 1972; Edwards Group, surface and subsurface, central Texas; Report of Investigations - Texas, University, Bureau of Economic Geology, Report: 74, 197 pp.
- Schindel, Geary M.; Johnson, Steve; and Alexander Jr., E. Calvin; 2007; Hypogene Processes in the Balcones Fault Zone Edwards Aquifer in south-central Texas, a new conceptual model to explain aquifer dynamics; Edwards Aquifer Authority Stratigraphy Field Trip, October 5 and 6, 2007; subset of internal EAA document.
- Stein, William G.; Ozuna, George; 1995; Geologic framework and hydrogeologic characteristics of the Edwards Aquifer recharge zone, Bexar County, Texas; Water-Resources Investigations - U. S. Geological Survey, Report: WRI 95-4030, 8 pp., 1 sheet.
- Tucker, Delos R.; 1962; Central Texas Lower Cretaceous stratigraphy; Transactions - Gulf Coast Association of Geological Societies, vol.12, pp.89-96.
- Van Siclen, DeWitt Clinton; 1958; Depositional topography; examples [Louisiana-Texas] and theory; Bulletin of the American Association of Petroleum Geologists, vol.42, no.8, pp.1897-1913.
- Wilson, J., 1975, Carbonate Facies in Geologic History: New York, Springer-Verlag, 471 pgs.

THE UNIVERSITY OF TEXAS AT SAN ANTONIO

AUV Design for Sea Ice Research

Michael Daniel[1]
Brent M. Nowak, Ph.D. [1]
Stephen Ackley [2]
[1] Mechanical Engineering Department, College of Engineering
[2] Geological Sciences Department, College of Sciences
San Antonio, Texas, USA

January 27, 2009

Abstract -Research under the Polar sea-ice is a remote, hazardous, and a unique environment. The Polar Regions are by definition remote, which limits access due to seasonal ice breaking expeditions in the Antarctic. Under ice investigations are hazardous to humans. Therefore, to conduct ongoing research under the sea-ice in Polar Regions requires an influx of technology. Remotely operated underwater vehicles (ROV) or autonomous vehicles (AUV) have been shown to be strong candidates to collect scientific data.

However, current AUV and ROV technologies are not specifically designed for sea-ice research. The most prolific AUV technologies are designed around the "torpedo" geometry. Many of the applications for this design are for benthic research. Two major commercial manufacturers are Bluefin Technologies and Hydroid, LLC. The cost of these AUVs is over $400,000. These costs are prohibitive for many researchers. ROV technologies have been typically designed around hull inspection, oil platform and oil pipeline service. Again, the costs and utility of these ROVs is limiting for sea-ice research.

Therefore, we conducted research, analysis, and prototyped candidate AUV designs for shallow depth applications. The requirements for the application were provided by Prof Steve Ackley (sea-ice geophysicts), in conjunction with Matthew Joordens (visiting researcher). The intent of the vessel is to explore the underside of arctic ice, creating a topographic map of the bottom of the ice. This would be used to monitor the melting rate of such ice caps. Our focus was the design of the hull for the AUV. The main constraints are as follows: The AUV had to be able to obtain a depth of 100 meters, it must be easily serviceable, and it must be cost effective to produce in numbers. During the course of the design we explored many different options for the design of the hull. Several shapes were investigated, as well as several materials. Once the design was narrowed down, we began running finite element analysis to ensure that the vessel could withstand the pressure at the depth. Next, several "hatch" designs were explored until a suitable option was found.

Our work is on-going, yet we will provide some preliminary results, discuss the analysis, and provide an outline of future work.

I. INTRODUCTION

The design of underwater vehicles presents an interesting and unique set of challenges. Like any design, there is a compromise between function, reliability, manufacturability, and cost. What sets this apart are the constraints that the operating environment imposes on the vehicle, for instance, the depth and pressure, as well as the extreme low temperatures that the vehicle operates in. Current underwater vehicles, whether remote, or autonomous, are very specialized units, and often the high cost associated with these vehicles is prohibitive to arctic researchers. One of the intended uses of this particular vehicle will be to explore the underside of the sea ice. Sonar can be used to map the topography of the bottom of the ice, this data can be compared month to month to observe the changes and movements of ice sheets. In addition to this, the vehicle will be affordable enough, and modular enough to be adapted for a large variety of undersea experiments and research.

II. BACKGROUND

This project was initiated by Mathew Joordens, a member of the Electrical Engineering department. Joordens developed the initial proof of concept, as well as the first prototype of a modular, affordable AUV. With this initial proof of concept and a basic outline of the requirements of the vehicle, Joordens contacted Prof. Brent Nowak for additional expertise in the robotics and mechanical design for the vehicle.

Figure 1: Original Proof-of-Concept AUV

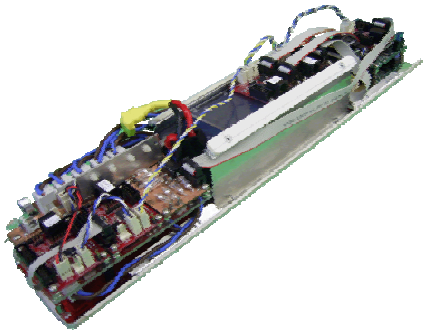

Figure 2: Proof-of-Concept Interal Configuration

With these initial concepts and basic requirements for the abilities, a literature study was conducted to determine what other researchers from around the world had published on AUVs. A comprehensive review of this study is covered by Nowak, see bibliography. From this survey it was concluded that current vehicles are too large and costly for this application.

There are several other companies around the world that have developed various underwater vehicles. Some of the more relevant to this research are as follows.

Monterey Bay Aquarium Research Institute (MBARI) developed a modular AUV on an preexisting chassis, the odyssey, which later became the Dorado class AUV.[i] This design is important due to a multitude of achievements that were demonstrated on this AUV, including single and multiple mid-body design and deployments. Of these all the achievements there are a

few that pertain to our research, the modifications that simplified the design, and introduced the concept of modularity by interchanging inner-hull sections in the Arctic.

Smith et. al. developed, designed, constructed, and tested a small plastic AUV in the "mini" class.[ii] This AUV was designed to a maximum depth of 300 meters.

Another company,Remote Environmental Measuring Unit(s) (REMUS), created by Woods Hole in 1994[iii]developed an array of AUVs that vary in size, abilities and cost. These vehicles range in size and depth ratings from 36 kg and 100 meters to 700kg and 6000 meters.

The design constraints for the vehicle to be developed were now fully ironed out. The vehicle was to be able to reach a depth of 100m, it must be re-configurable in order to suit many different researchers needs, it must be serviceable by the researchers, and it must be cost effective to manufacture.

III. DESIGN CONCEPTS

Once the design constraints were fully defined, initial concepts were then discussed. The first thing to be determined was the internal layout of components. This was crucial due to the re-configurability constraint. Several different layouts were considered, a "manta ray", a sphere, and a torpedo.

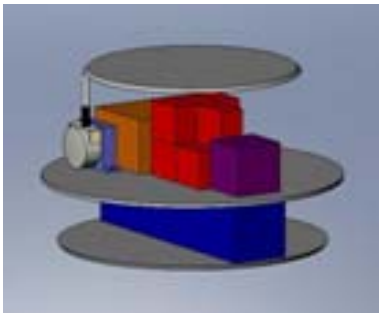

Figure 3: Spherical layout

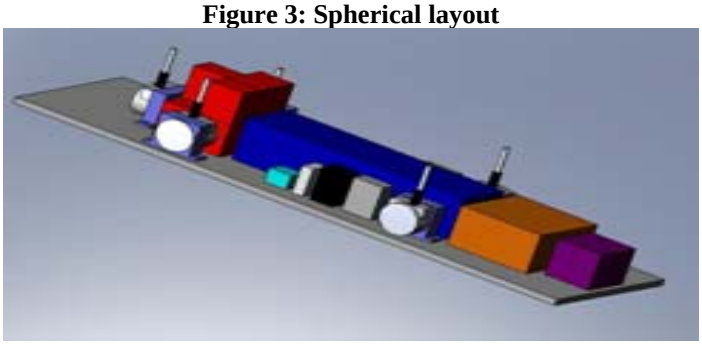

Figure 4: Torpedo Layout

Having determined which configuration would be the easiest to adapt too many different sensors, several other configurations of a similar basic lay-out were investigated. The torpedo design was chosen due to its adaptability of length, and cost effective hull design. Once the basic shape was determined many different materials were considered including, but not limited to aluminum,

PVC, steel, and carbon composite. Along with these materials, several different manufacturing processes were considered including, but not limited to, blow-molding, injection molding, extrusions, casings, and traditional machining.

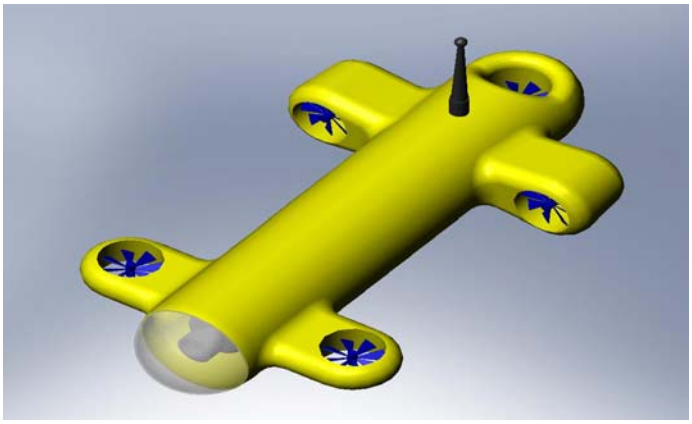

Figure 5: single piece hull

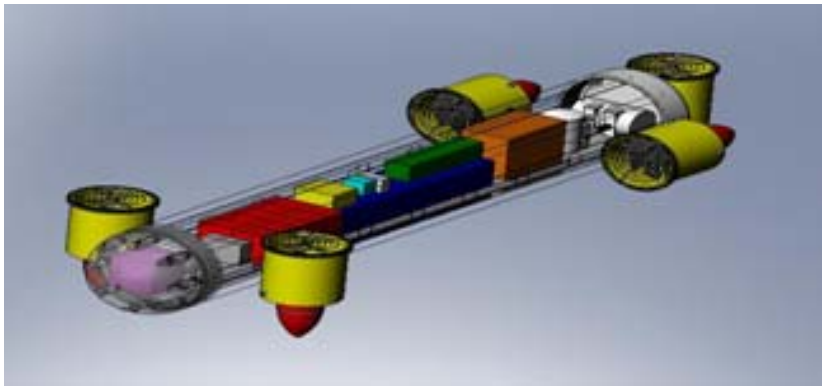

Figure 6: Multi Piece Hull

Although at this time no final decisions were made about the hull construction, the design team leaned in the direction of the multi piece hull in order to keep tooling costs to a minimum, as well as to further increase modularity and serviceability. The next major design objective to tackle was the hatch design. This component is crucial when considering the serviceability aspect of the vehicle.

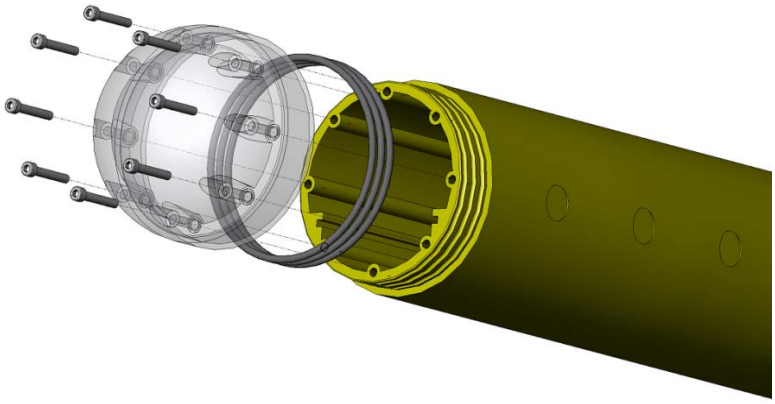

Figure 7: Bolt on Hatch

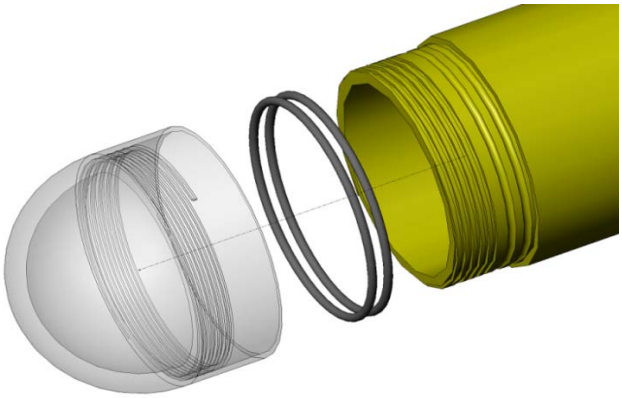

Figure 8: Screw-Type Hatch

In conjunction with developing these various concepts stress analysis was conducted on some of the different hull and hatch designs using finite element analysis software. The results of this analysis were promising, and revealed a high factor of safety, which allows a substantial amount of design flexibility.

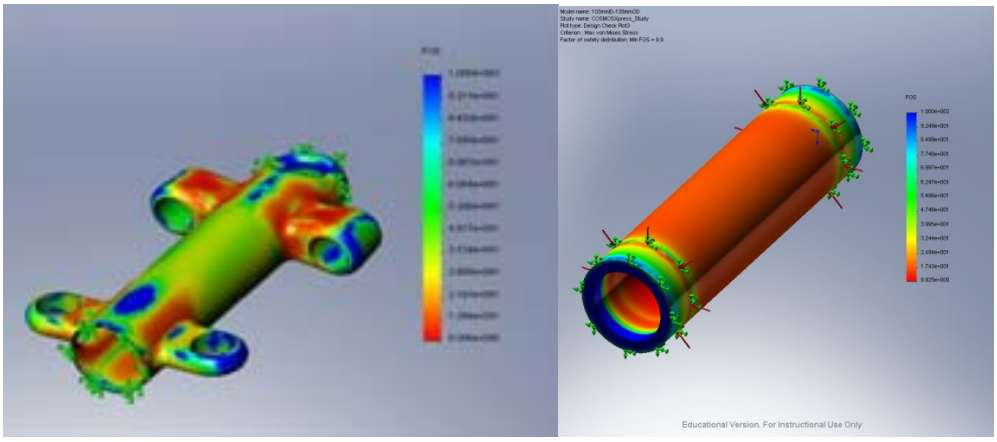

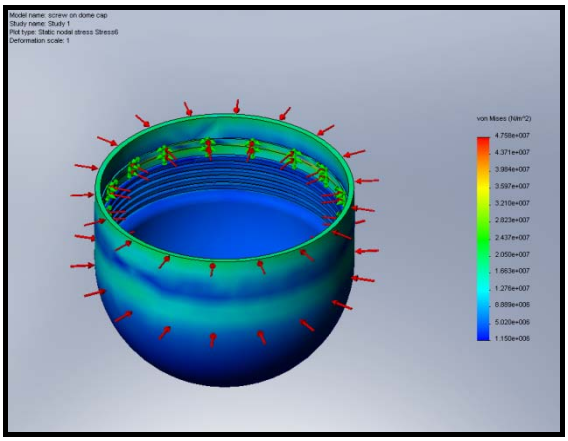

Figure 9: FEA of Components

IV. CONCLUSIONS

The work highlighted in this paper is an ongoing project that requires much further analysis to be conducted. However, the results thus far are very promising. Future work is to include ballast design, vehicle dynamics and balance, thruster design, hydrodynamic studies, and sensitivity analysis.

Special thanks to Brent M. Nowak, Ph.D. (College of Engineering), Prof. Stephen Ackley (College of Sciences), and Hongjie Xie Ph.D. (College of Engineering) for their support, as well as, the NSF MORE Science program.

V. REFERENCES

[1] [i] Sibenac, M. ; Krikwood, W.J. ; McEwen, R. ; et.al., "Modular AUV for Routine Deep Water Science Operations", IEEE 0-7803-7534-3, pp. 167-172., 2002.

[2] [ii] Smith, S. M. ; Kronen, D. ; et. al., "An Ultra Modular Plastic Mini AUV Platform for VSW Mine Reconnaissance", SPIE Conference on Information Systems for Navy Divers and Autonomous Underwater Vehicles Operating in Very Shallow Water and Surf Zone Regions, SPIE Vol. 3711, April 1999, pp. 173 – 183.

[3] [iii] von Alt, C. ; Allen, B. ; Austin, T. ; Stokey, R. ; "Remote Environmental Measure Units", Proceedings of the 1994 Symposium on Autonomous Underwater Vehicle Technology, July 19-20, 194, pp. 13 – 19.

[4] Nowak, B.; Ayhan, Y.; et al., “Design and Analysis of Hull Configurations for a Low-Cost, Autonomous Underwater Robot as an Enabling Technology for System of System Applications”, IEEE Systems, 2008.

Satellite Image-Based Geospatial-Intelligence Technique: Development and Implementation of a New System for Categorization Using Statistical Tools

Shuangxi Xie, **MS Student**

Keying Ye, **Advisor**

Department of Management Science and Statistics
University of Texas at San Antonio

The aim of this project is to develop and implement a new system in classifying the subjects of geospatial multi-spectral satellite data sets, by using Bayesian statistical method. In order to improve our satellite remote sensing data for geospatial intelligence analysis, we develop two data analysis systems based on the Bayesian algorithm in processing multi-dimensional data sets. The first one uses individual-band-frequency and the other one uses multivariate normal distributions. Through our study of satellite images, we first carefully choose training data sets containing different wave bands for a set of terrain types. Given a specific type of terrains, we construct a frequency table for each individual wave band in the individual-band-frequency approach; while in the multivariate normal distribution method, we construct multivariate normal distributions among all the wave bands.
In both approaches, we then apply the Bayes' rule to calculate the posterior probability related to each type of terrains for any individual pixel data that needs to be classified. Consequently, the specified pixel is then classified as a certain type of terrains with the largest posterior probability associated with this type. Although we have not applied our methods to large data sets, preliminary data analyses show that the results are promising. In future, we hope that we will be able to integrate our algorithm with the ArcGIS program to calculate the percentage of given terrain types in a specific area of satellite images.

Introduction

In this project, we are trying to convert the large quantities of geospatial data into useful and actionable information and intelligence. We want to classify the types of terrain automatically and efficiently by using our algorithm. The capacity of traditional human analysis and data classifying through the use of manual tools has many limit, but the intelligence technique is becoming the mostly important source information which directly derived from the satellite remote sensing datasets without touch and interaction.

In this study, we carefully chose the training dataset. All the algorithms to predicting other data are based on these datasets. In first approach, we assume that each terrain type is independent from each other, and then we get the maximum probability of any pixel with a given type by using Bayes' rule. In second approach, we construct the frequency distribution by using multivariate normal approximation because we believe that correlations among the wave bands for any given type of terrains do exist. Again, once we established normal distribution parameters, we obtain the maximum posterior probability of any pixel with a given type. We will use Arcmap to present types of all the pixels by different colors and we will compare these pictures with the original image to evaluate whether the algorithms are accurate and efficient in distinguish different terrain types.

Study Area and Data

The basic study area is found from LANDSAT ETM+ image of San Antonio acquired on July 21st, 2001. The ETM+ sensor has a moderate spatial-resolution (30 m for multi-spectral images and 60 m for thermal image). You cannot see individual houses on a Landsat image, but you can see large man-made objects such as highways (http://landsat.gsfc.nasa.gov/about/)

Figure 1: A partial image of the LANDSAT data (7/21/2001)

We randomly chose pixels and the dataset consist of 15 variables and number of observations. Explanations for all variable abbreviations are given in Table 1.

Table 1. The meaning of LANDSAT image variables.

ID	pixel number, is integer.
X	The X coordinates of these entire pixels window;
Y	The Y coordinates of these entire pixels window;
MapX	The UTM coordinate in X direction
MapY	The UTM coordinate in Y direction
Lat	The geographic latitude of the earth;
Lon	The geographic longitude of the earth;
B1	blue band, value from 0~255, no unit;
B2	Green band, value from 0~255, no unit;
B3	red band, value from 0~255, no unit;
B4	near infrared, value from 0~255, no unit;
B5	middle infrared, value from 0~255, no unit;
B6	temperature, value from 0~255, no unit; it's not the true temperature of the earth, but it is used to weight the true temperature value.
B7	middle infrared, value from 0~255, no unit;

Methods

Training datasets

The training datasets consist of pixels chosen from the satellite images. We chose nine terrain models and they are: agriculture cut, agriculture white, agriculture yellow, airport white (or concrete), grass, mining white (or limestone quarry), road, tree, and water. The selections of terrain types are based on visual recognition. Using these nine training datasets, we constructed our likelihood functions based on two methods. In individual-band-frequency table, we constructed the frequency table of the band wave readings for each individual terrain type without assuming any distributional form. On the other hand, the means and the variance-covariance matrices were calculated empirically from the training data and the multivariate normal distribution was constructed for each terrain type.

Individual-Band-Frequency Table

In this case, we assume that all the readings of nine terrain types are independent of each other. Total nine types of terrain is considered and for each type there are seven bands (or variables). First, we establish frequency models from the training datasets. The digital number ranges of bands 1 through 7 (B1-B7 in Table 1) are all from 0 to 255, we partitioned each range by regions with equal distance of 3 each and call those regions as "bin." Therefore, we obtained 256/3=85 total regions in the "bin" variable for each band. We mapped all the band values as "bin" values and constructed the frequency values for each type by using the training data. The relative frequencies through the "bin" range thus constitute the probability distribution, for each wave band. Part of those probability tables are given in Table 2.

Table 2. The probability distribution of bands (partial results). Type: 1 grass, 2 tree, 3 agriculture cut, 4 agriculture white,5 agriculture yellow, 6 road, 7 water, 8 airport white, 9 mining white; band:1-7 is B1- B7; Bin is band value/3, from 0-85; Prob: the probability of each band with the given type. Memo denotes the type of terrain represent by variable Type.

Type	Band	Bin	Prob	Memo
1	1	1	0	grass
1	1	2	0	grass
...	...	...	...	...
1	1	25	0.0012837	grass
1	1	26	0.0051348	grass
1	1	27	0.0141207	grass
...	...	...	...	...
9	7	68	0.001446	mining white
9	7	69	0	mining white
9	7	70	0	mining white
...	...	...	...	...

Once the frequency tables are established, we chose a sample image from the LANDSAT data. Assuming variable "bin" has index *I*, band with index *J*, and terrain type with index *T*, the frequency tables provide us the likelihood function

$$P(X_j = i \mid T) = P_{ijt}$$

From the Bayesian statistical method (see Galeman *et al*, 2005), we conclude that, for any pixel data with 7 band values, the posterior probability that this pixel belonging to type *t* can be calculated as

$$P(T = t \mid X_j = x_j, j = 1,...,7) = \frac{P(X_j = x_j, j = 1,...,7 \mid T = t)P(T = t)}{\sum_t P(X_j = x_j, j = 1,...,7 \mid T = t)P(T = t)}.$$

Assuming that we do not have any prior information which terrain type this pixel belongs to, i.e., $P(T = t) = \frac{1}{T}$, where *T=9* is the total number of types under consideration, we get

$$P(T = t \mid X_j = x_j, j = 1,...,7) = \frac{\prod_{j=1}^{7} P(X_j = x_j \mid T = t)}{\sum_{t=1}^{9} \prod_{j=1}^{7} P(X_j = x_j \mid T = t)}. \qquad (1)$$

For each individual pixel data with 7 band wave values, using formula (1), we can obtain the posterior probability that the geological point associated with this pixel belonging to each of the 9 terrain types. We then compare these nine posterior

probabilities and choose the one type with maximum value.

Multivariate Normal Distributions

From the nine training dataset, we found that there are correlations among different types for some of the wave bands. To incorporate such a correlation in likelihood in our analysis, we try to use multivariate normal distributions as an approximation.

Using the training data, we obtained the sample means and sample covariance matrix of the seven bands for each type. We then use these means and covariance matrices to construct 9 multivariate normal models associated with 9 terrain types. Assume the point that needs to be classified has pixel values $\underline{X}_0 = (X_{01},..., X_{07})$ while $\underline{X}_0 \sim n(\underline{\mu}(t), C(t))$ where $\underline{\mu}(t)$ and $C(t)$ are the mean vector and covariance matrix, respectively, for each give type $T=t$. The density function of $\underline{X}_0$ can be written as

$$f(\underline{X} \mid \underline{\mu}(t), Cov(t)) = \frac{1}{(2\times\pi)^{\frac{7}{2}} \times |C(t)|^{\frac{1}{2}}} \times e^{-\frac{1}{2}(\underline{X}-\underline{\mu}(t))' \times C(t)^{-1} \times (\underline{X}-\underline{\mu}(t))}.$$

Assuming again the non-informative prior probability at the point, we obtain the posterior probability that this point belongs to Type t as

$$P(T=t \mid \underline{X}_0) = \frac{f(\underline{X}_0 \mid t)P(t)}{\sum_{j=1}^{9} f(\underline{X}_0 \mid j)P(j)} = \frac{f(\underline{X}_0 \mid t_i)}{\sum_{j=1}^{9} f(\underline{X}_0 \mid j)}$$

$$= \frac{\frac{1}{|C(t)|^{\frac{1}{2}}} \times e^{-\frac{1}{2}(\underline{X}_0-\underline{\mu}(t))' \times \mathrm{cov}_i^{-1} \times (\underline{X}_0-\underline{\mu}(t))}}{\sum_{j=1}^{9} \frac{1}{|C(j)|^{\frac{1}{2}}} \times e^{-\frac{1}{2}(\underline{X}_0-\underline{\mu}(j))' \times \mathrm{cov}_j^{-1} \times (\underline{X}_0-\underline{\mu}(j))}}$$

$$= \frac{1}{\sum_{j=1}^{9} \frac{|C(t)|^{\frac{1}{2}}}{|C(j)|^{\frac{1}{2}}} \times e^{-\frac{1}{2}[(\underline{X}_0-\underline{\mu}(j))' \times \mathrm{cov}_j^{-1} \times (\underline{X}_0-\underline{\mu}(j)) - (\underline{X}_0-\underline{\mu}(t))' \times \mathrm{cov}_i^{-1} \times (\underline{X}_0-\underline{\mu}(t))}}}.$$

Again, we will classify the type with largest posterior probability.

Results

First, we assume that each terrain type is differentiable from one another, we use Delphi software with SQL language to search the Bin values and then we obtain the results in Table 3 (only shown partially). And the classified results shown in Figure 2

Table 3. The maximum probability of type for the test image using individual-band-frequency method. P1-P9 is the probability value of a pixel of different type; MaxP is the maximum probability value of a pixel by using Bayesian statistical method. Type is the maximum probability type by comparing all the probability.

P1	P2	P3	P4	P5	P6	P7	P8	P9	MaxP	Type
0.00	0.00	0.00	0.00	0.00	0.00	0.00	1.00	0.00	1.00	airport white
0.00	0.00	0.00	0.00	0.00	1.00	0.00	0.00	0.00	1.00	road
0.00	0.00	0.00	0.00	0.00	1.00	0.00	0.00	0.00	1.00	road
0.00	0.00	0.00	0.00	0.00	1.00	0.00	0.00	0.00	1.00	road
0.00	0.00	0.00	0.00	0.00	1.00	0.00	0.00	0.00	1.00	road
0.37	0.00	0.09	0.00	0.00	0.53	0.00	0.00	0.00	0.53	road
0.10	0.00	0.03	0.00	0.00	0.88	0.00	0.00	0.00	0.88	road
0.38	0.00	0.52	0.00	0.00	0.10	0.00	0.00	0.00	0.52	ag. cut
0.00	0.00	0.00	0.00	0.00	1.00	0.00	0.00	0.00	1.00	road
0.00	0.00	0.00	0.00	0.00	1.00	0.00	0.00	0.00	1.00	road
0.00	0.00	0.00	0.00	0.00	1.00	0.00	0.00	0.00	1.00	road
0.00	0.00	0.00	0.00	0.00	1.00	0.00	0.00	0.00	1.00	road
…	…	…	…	…	…	…	…	…	…	…

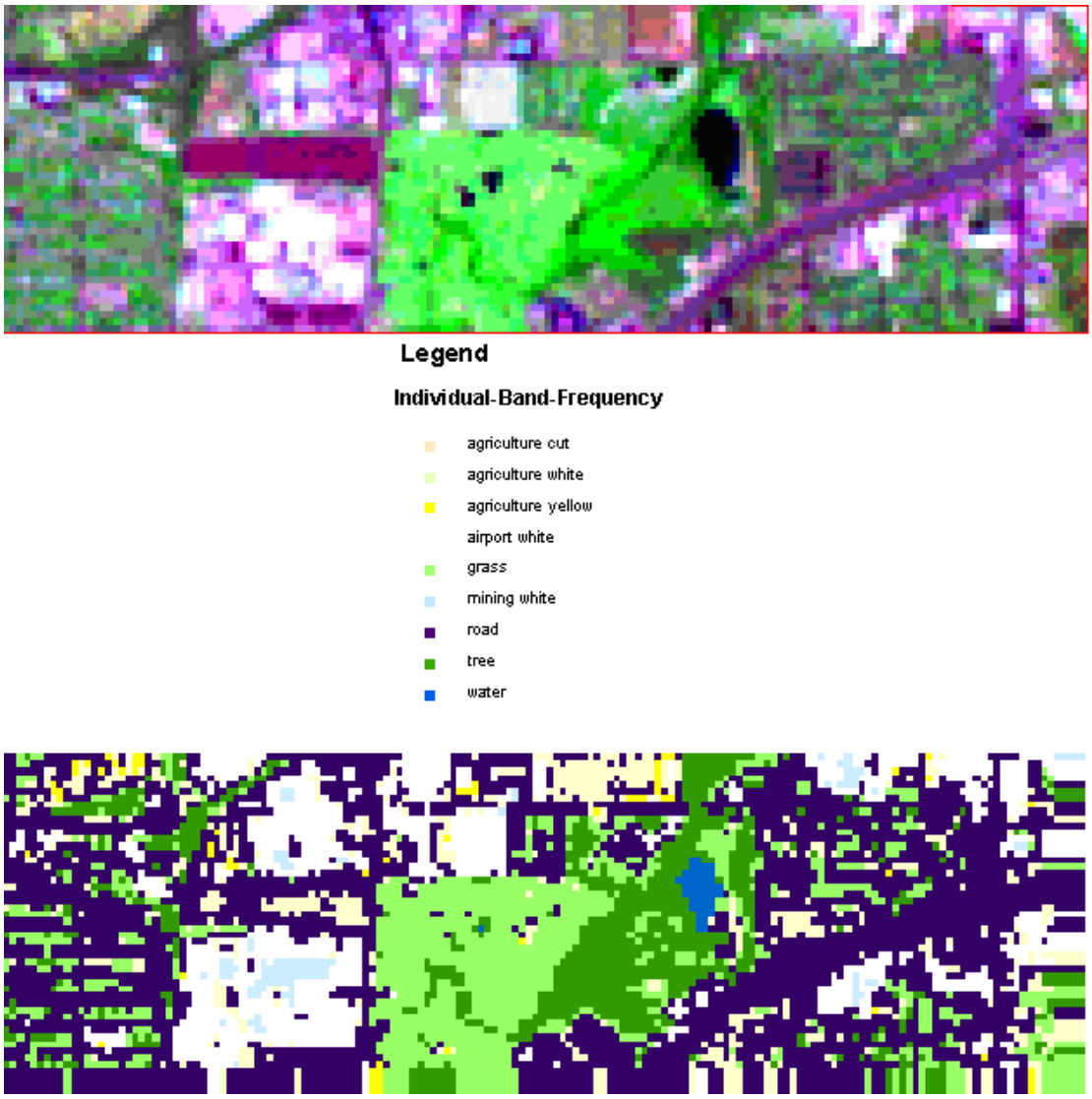

Figure 2: Comparisons of the original image (top) to the classified image (bottom) using individual-band-frequency table.

Next, we use multivariate normal distribution approximation to classify each pixel point. We use R program to calculate the results and partial results are given in Table 4 and classified results are shown in Figure 3.

Table 4. The maximum probability of type for the test image when suppose the data follows multivariate normal distribution. P1-P9 are the probability values of a pixel to types: 1 for agriculture cut, 2 agriculture white, 3 agriculture yellow, 4 airport white, 5 grass, 6 mining white, 7 road, 8 tree, and 9 water. MaxP is the maximum probability value of a pixel by using Bayesian statistical method. Type is the maximum probability type by comparing all the probability.

P1	P2	P3	P4	P5	P6	P7	P8	P9	MaxP	Type
0.00	0.00	0.00	1.00	0.00	0.00	0.00	0.00	0.00	1.00	airport white
0.00	0.00	0.00	0.00	0.00	0.00	1.00	0.00	0.00	1.00	road
0.00	0.00	0.00	0.00	0.00	0.00	1.00	0.00	0.00	1.00	road
0.00	0.00	0.00	0.52	0.00	0.00	0.48	0.00	0.00	0.52	airport white
0.00	0.00	0.00	0.00	0.00	0.00	1.00	0.00	0.00	1.00	road
0.00	0.00	0.00	0.01	0.98	0.00	0.02	0.00	0.00	0.98	grass
0.00	0.00	0.00	0.00	0.06	0.00	0.94	0.00	0.00	0.94	road
0.00	0.00	0.00	0.00	0.00	0.00	1.00	0.00	0.00	1.00	road
0.00	0.00	0.00	0.00	0.00	0.00	1.00	0.00	0.00	1.00	road
0.00	0.00	0.00	0.18	0.00	0.00	0.82	0.00	0.00	0.82	road
…	…	…	…	…	…	…	…	…	…	…

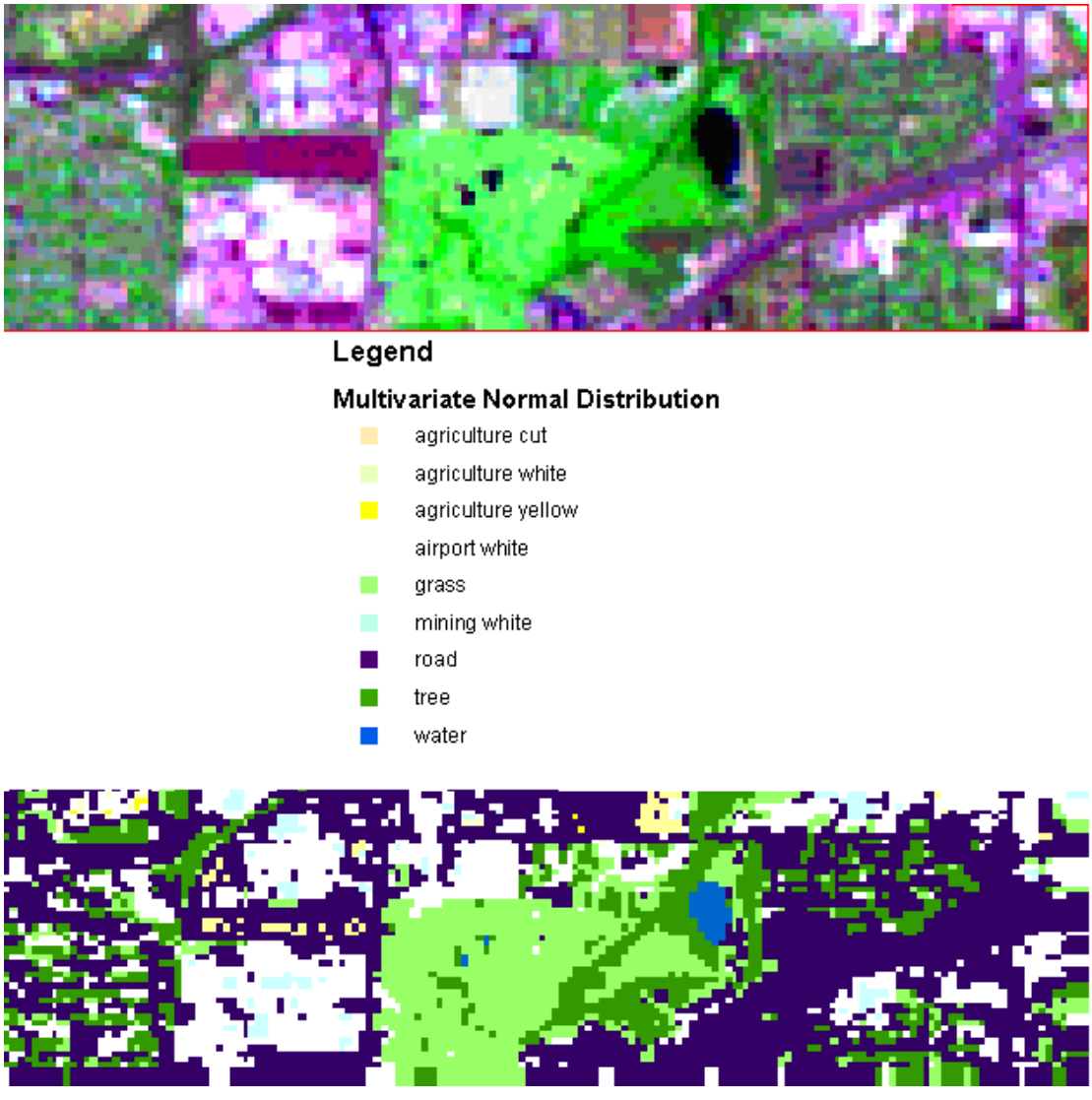

Figure 3: Comparisons of the original image (top) to the classified image (bottom) using the multivariate normal distribution method.

Discussions and Conclusions

From the data, we observe that, although we only used 9 different types, our algorithm is actually quite efficient in classifying the types of terrian included in this project, especially using the individual-band-frequency method. The multivariate normal distributions may be able to incorporate correlations among the wave bands. Yet, the data self may not be really following normal distributions. Hence it seems that multivariate normal distribution method results in more blurry images than the individual-band-frequency method. In the future we may combine those two methods together to make the classification more accurate. Furthermore, we may also incorporate spatial correlation into our modeling.

Acknowledgments

I would like to thank Dr. Ye for all his instruction and guidance for the past few months; and Dr. Xie's help in obtaining training datasets and assistance with Arcmap program. Finally, I would like to also thanks for the opportunity provided by the MORE Science internship.

References

Galeman, A. Carlin, J.B., Stern, H.S., and Rubin, D.B. (2005), Bayesian Data Analysis, 2nd edition, Chapman & Hall/CRC, New York.

THE UNIVERSITY OF TEXAS AT SAN ANTONIO

Analysis of ROV Video Imagery for Krill Counting under Antarctic Sea Ice

Brent M. Nowak, Ph.D. [1]
Thomas G. Whitney III [1]
Stephen F. Ackley [2]
[1] Mechanical Engineering Department, College of Engineering
[2] Geological Sciences Department, College of Sciences
San Antonio, Texas, USA

January 16, 2009

Abstract - An off-the-shelf SeaBotix ROV (Remotely Operated Vehicle) was deployed under the Antarctic sea ice near Palmer Station Antarctica during the September-October 2007 Sea Ice Mass Balance in the Antarctic (SIMBA) project from the research vessel *NB Palmer*. Video imagery taken showed significant numbers of Antarctic krill (sp. *Euphasia Superba* and/or *Euphasia Crystallorophis*) under the sea ice at the two stations deployed.

The goal of this research is to conduct image analysis on the recorded ROV video footage. From this we hope to count and estimate the visible krill population, as well as, make steps towards identifying other life forms. The difficulties of the image analysis include, but are not limited to, the relative motion between the krill and vehicle, the avoidant behavior of the krill, and the changing lighting conditions under the sea ice. In this paper, we will discuss these and other challenges and describe the algorithms that are under development.

For the image analysis, the ROV video was converted into a string of JPEG images, which were used to simulate an approximate running speed of 3 frames/second (fps). Three 5 second clip (15 frames each) were selected as an initial test for the developed image algorithm.

National Instruments: Vision Builder for Automated Inspection® has been selected as an image processing platform, which allows for rapid prototyping of algorithms. We found that inconsistent underwater illumination and poor image quality allowed only the most prominent individuals in proximity of the camera to be counted. In order to increase the visible depth of the recorded footage, certain image processing techniques were conducted. Grayscale noise reduction techniques were applied to reduce some of the image distortion. Edge detection filters (such as, but not limited to the Sobel and Roberts Filter) have been applied to further reduce the image's noise level and increase the contrast between the krill and the background environment. Next, intensity mapping was used to detect and count the contrasted objects. Finally, the data were logged. Once all of the parameters were set, the 15 images were cycled through the configured inspection in chronological order to simulate an actual inspection of the ROV video. Once completed, the result of the automated krill estimation was compared to a visual (naked eye) inspection of the same krill images.

These image techniques, through research and testing, appear to have practical application. Using these image enhancement techniques and other current technologies, we hope to develop an adaptable vision system that can be used in variety of underwater tasks. These and other issues are also discussed.

I. INTRODUCTION

This paper describes the early development of an image processing method applied to ROV video imagery for the purpose of identifying sea life and estimating population densities. In this work, we specifically address the method of image analysis, in the hopes that an adaptable system can one day be used for krill identification and population density estimation.

The Sea Ice Mass Balance in the Antarctic (SIMBA) program was a two-month science expedition from September to October 2007 [1]. During this program, a commercial, off-the-shelf, underwater Remotely Operated Vehicle (ROV), equipped with a general purpose color video system, recorded the footage which was used in this project. The SeaBotix Remote Underwater Vehicle (ROV), which was used in the SIMBA program, is equipped with two video cameras [2]. The primary camera is a 570 line color image based upon the Sony Ex-View HAD CCD with 0.2 lux sensitivity. The secondary camera is a 430 line black and white camera with

0.03 lux sensitivity. The internal lighting system provided with the camera is a 700 lumen LED array that allows the operator to vary the intensity.

The primary mission of the SIMBA program's ROV deployment was an investigation into ice, not sea life. But as a result of the supplied video imagery, our goal is to develop image processing solutions that may enable adaptive, autonomous behaviors of future underwater vehicles.

Section II discusses some of the technical challenges associated with underwater sea life identification and tracking. Section III describes our image analysis process. Our experimental results are described in Section IV. We close the paper with Conclusions in Section V.

II. BACKGROUND

Given the remote and severe conditions of the Polar Regions, ongoing scientific research of these hazardous environments by humans is prohibitively risky and costly. Yet, these regions are under-sampled and of high scientific, ecological and environmental importance, as explained by Yuh [3] and Singh [4]. These dual drivers have spurred the development of Remotely Operated Vehicles and Autonomous Underwater Vehicles (ROVs and AUVs, respectively).

These drivers have resulted in parallel, but non-uniform developments, in underwater platforms and imaging hardware, software and algorithms. For this work, it is essential to understand the nonlinear and coupled nature between the undersea platform (AUV or ROV) and the imaging system (camera or video).

Yuh provides a broad survey of the developments in AUV and ROV subsystems, applications and sensing systems that have occurred in the last decade of the 20th century. Singh discusses the challenges and advancements of underwater photography, imaging technologies and photomosaicing. Yuh and Singh, as well as, Jones [5], and Caccia [6] identify motion artifacts as one of the limitations to underwater imaging.

The technical challenges involved with the SIMBA project's ROV video imagery include, but are not limited to, turbidity, natural light absorption/scattering, non-uniformity of the ROV's artificial lighting, and variations due to depth, temperature and season, as discussed by Negahdaripour [7], Ortiz [8] and Fairweather [9]. In the case of expeditions under the sea ice, we have observed conditions, (author's observations on a separate expedition to Barrow Point, Alaska), that are equivalent to where the snow and ice thickness create a "cloudy day". As seen in Figure 1-2, although the water has low turbidity and adequate light, hot-spotting, the "cloudy day" effect and inconsistent lighting from the ice are still prevalent.

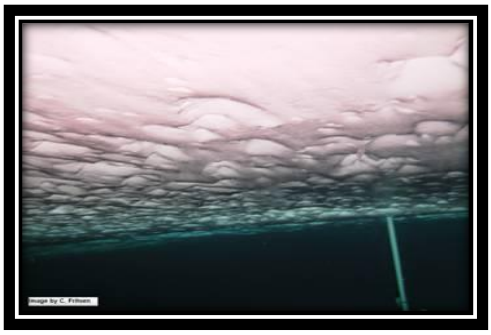

Figure 1: Site Brussels (Image by C. Fritsen [10])

Figure 2: Site Liege (Image by C. Fritsen [10])

III. IMAGE ANALYSIS PROCESS

The analysis software chosen for the krill population estimation was National Instruments (NI): Vision Builder for Automated Inspection (VBAI). It is an icon-based computer inspection software package, which allowed for rapid prototyping of inspection algorithms, as used by Andres [11] and discussed in the VBAI Manual [12]. Since Vision Builder's programming capabilities only include analysis on single digital images (no video footage), the ROV video (approximately 1800 seconds long) was converted into 5,370 images to model it at a running speed of roughly 3 fps using the Free Video to JPG Converter [13].

After the image conversion was completed, three 5-second clips (15 images/clip) were selected for analysis. The three clips were chosen because each displayed a variety of different background/lighting conditions, krill movements and ROV motion. The first test clip displayed the ROV moving at a relatively high speed in extremely cloudy water, with many krill being blurred by the vehicle motion and environmental effects. The second clip displayed a relatively stationary, although cloudy, environment, with blurred krill swimming in and out of the field of view, while the ROV remained still. In the final clip, the ROV's field of view is stationary and oriented towards the under surface of the sea ice, displaying a large number of krill in cloudless water. Although the water was clear, the underside of the ice drastically reduced the contrast of the krill to the background, which created problems in identification. The three unique clips were used to test the robustness of the developing algorithm. From the results of the three ROV image sets, we may be able to determine if one algorithm could be applied to the entire ROV video, which includes a wide variety of environmental conditions.

In order to do any image analysis, VBAI required all images to be converted from red, green and blue (RGB) color images to grayscale images. The Vision Assistant application was used for this grayscale conversion, which also slightly reduced the noise level of the images, as discussed in the VBAI Manual.

Next, the available VBAI image filters, listed and described in the VBAI Manual, were compared as they were applied to the underwater images to verify which filter, qualitatively and quantitatively, extracted the most krill from the background. The edge detection filters available in Vision Builder include the Laplacian, Differentiation, Prewitt, Sobel, and Roberts filter. Each filter uses a kernel (3x3 matrix), Figure 3, which is applied to each pixel of the image to extract and extend edge information.

$P_{1\,(i-1,j-1)}$	$P_{2\,(i,j-1)}$	$P_{3\,(i+1,j-1)}$
$P_{4\,(i-1,j)}$	$P_{5\,(i,j)}$	$P_{6\,(i+1,j)}$
$P_{7\,(i-1,j+1)}$	$P_{8\,(i,j+1)}$	$P_{9\,(i+1,j+1)}$

i=1, 2…# pixels in x direction
j=1, 2…# pixels in y direction

Figure 3: Basic Image Filter Kernel

In comparison of the different filtering methods, the Laplacian and Prewitt filters created very bright regions around the edges of the krill within the field of view, which decreased the number of individuals extracted from the background. This created problems when the Detect Object feature, discussed in the VBAI Manual, was applied to the developing algorithm. The Sobel, Roberts and Differential filters created much smoother edge extraction, making the krill more distinct from the background.

Through visual inspection and comparison of the results of each filter, the Sobel Filter was selected as the best available option for filtering out the image's background and displaying the

krill's outline. The Sobel Filter is an edge detection filter that measures variations in pixel intensity values to determine and extract an object's edges, as explained in the VBAI Manual.

Gonzalez [14] explains the Sobel gradient operator.

-1	-2	-1
0	0	0
1	0	1

-1	0	1
-2	0	2
-1	0	1

Figure 4: Sobel Horizontal and Vertical Operators

Figure 4 displays the kernel used to filter the krill images. The process applies the kernel to each pixel of the image and calculates a new value of the specified image pixel based on Eq. 1, which is derived and explained in Gonzalez.

$$p_5 \approx |(p_7 + 2p_8 + p_9) - (p_1 + 2p_2 + p_3)| + |(p_3 + 2p_6 + p_9) - (p_1 + 2p_4 + p_7)| \quad \{1\}$$

By using this method, the 3x3 kernel reduces (darkens) the intensity values (0-255) of areas having large numbers of pixels with similar intensity values and the kernel increases (lightens) the intensity of areas having large numbers of pixels with dissimilar intensity values.

Next, the Detect Object icon was imported into the algorithm, which was used to count the number of distinguishable krill outlines extracted from the original image. The detect object feature uses the calculated pixel intensity values of an image to identify groups of touching pixels with similar intensity values to be declared as 'objects' within the image. Based on VBAI's user-defined inputs, the number of required pixels for consideration as an object, increased or decreased the number of objects detected based on the pixel count input size.

The final step in the algorithm was logging the recorded number of objects detected in the automated inspection, as well as the elapsed inspection time, to a text file, as explained in the VBAI Manual. Figure 5 displays a flow diagram of the image algorithm.

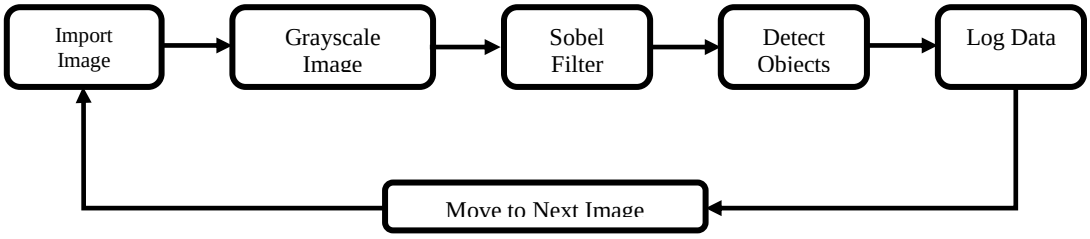

Figure 5: Image Analysis Flow Diagram

After the inspection algorithm was completed, each of the three 15 frame ROV clips were imported into VBAI and processed through the developed algorithm.

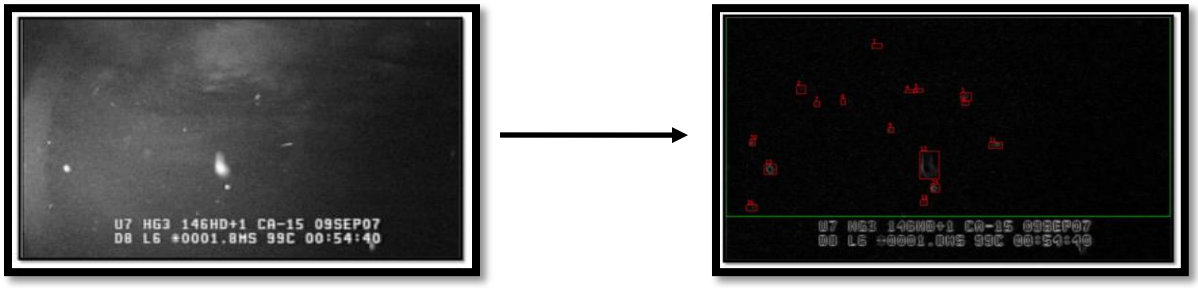

Figure 6: Results of the Developed Algorithm

Figure 6 illustrates the type of results that are achieved and displayed by the image analysis algorithm. As the figure shows, the algorithm was able to extract and display the most prevalent krill in the image. Section IV provides a brief overview of the data samples and statistical findings.

IV. DATA AND FINDINGS

In the next 3 pages, we explain and display the range environmental conditions that the imaging system had to adapt to on the 3 expedition video clips. Figure 7 illustrates some of the ROV induced imaging challenges. The left-hand side of each image suffers from hot-spotting induced by the ROV's LED lighting array. Also the ROV lens creates a halo effect as seen by the bright semi-circle on the left-hand side of each image. Finally, the motion of the vehicle blurred the visible krill and induced the white traces.

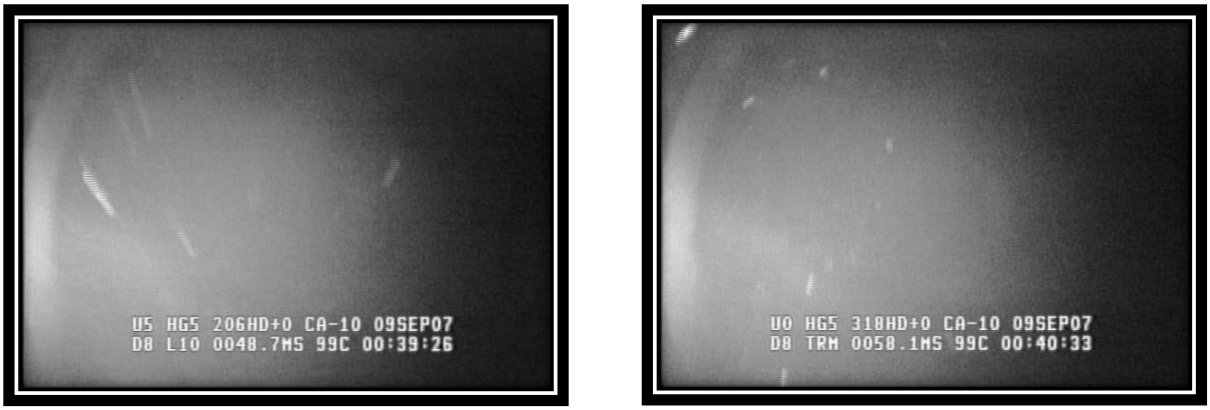

Figure 7: ROV Induced Imaging Challenges

Three series of images are provided, preceded with a histogram of the results and a brief discussion of the environment. In addition to the automated results, the histograms graphically illustrate the difference between the krill counts by a human (purple) vs. the image analysis algorithm (maroon). Finally, we provide a statistical comparison of the three in Table 1.

The first clip used in the analysis is shown on the next page (Figure 8b). The ROV was moving at high speed through the water, which greatly reduced the clarity of the krill. This blurring effect, due to the speed, the glare from the illumination source and the 'cloudy-day' effect from the water affected the krill's grayscale intensity values relative to the background, which in turn affected the ability of the program to identify them as objects, as seen in Figure 8a.

Figure 8a: Data from First ROV Video Clip

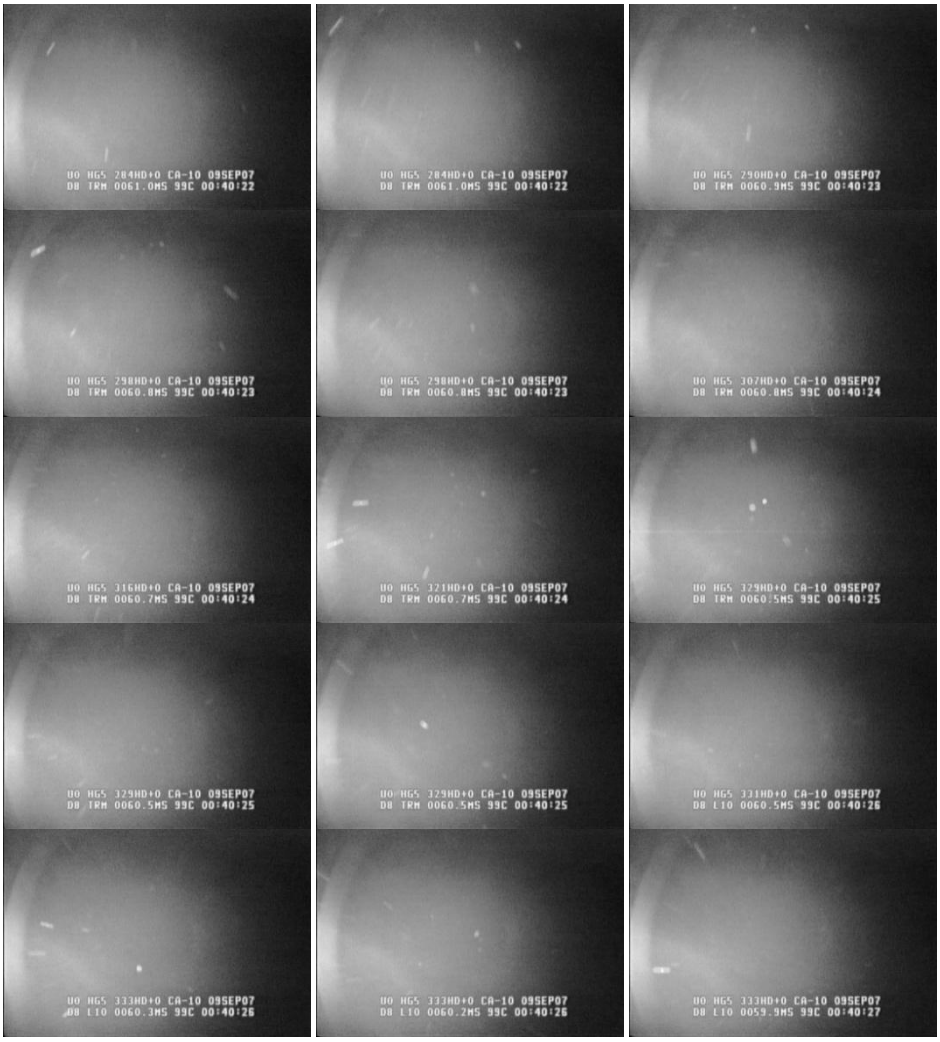

Figure 8b: Images from First ROV Video Clip

The second clip used to test the developed algorithm is shown below (Figure 9b). The ROV was relatively stationary at this point, allowing more krill to be illuminated and displayed in the field of view. The glare from the LED array and the 'cloudy-day' effect from the underwater images affected the krill's grayscale values and decreased the number of krill that could be identified, as seen in Figure 9a.

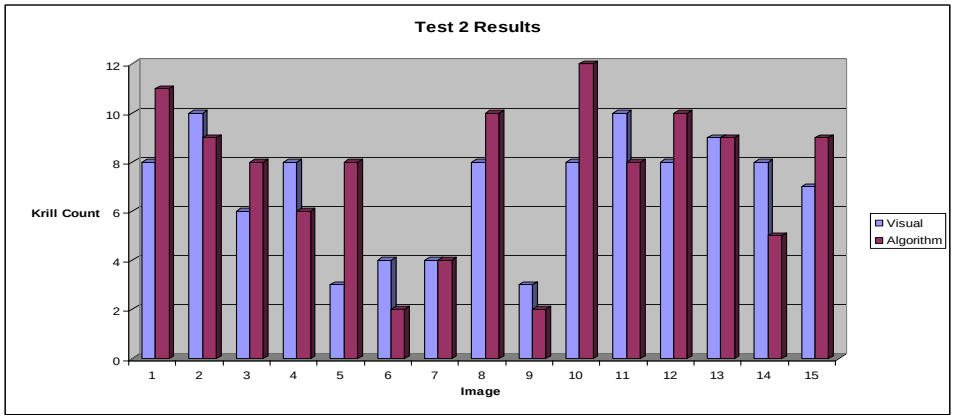

Figure 9a: Data from Second ROV Video Clip

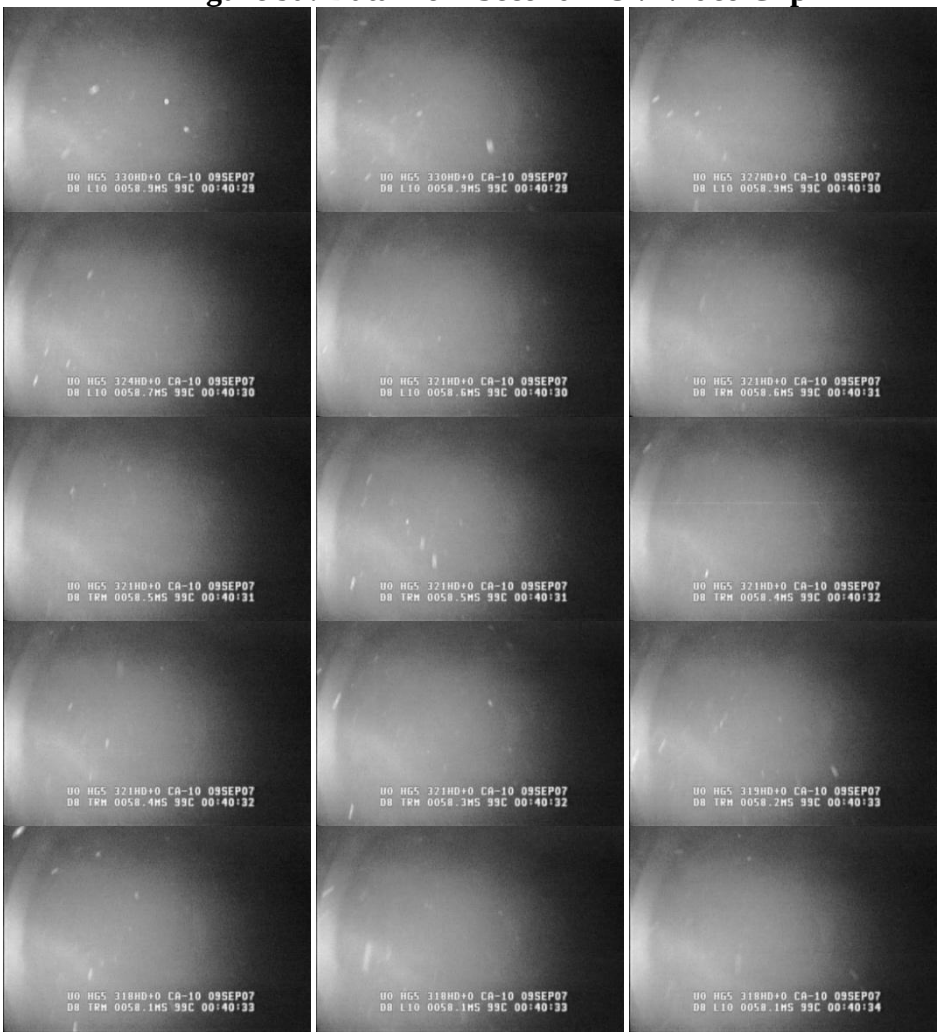

Figure 9b: Images from Second ROV Video Clip

The last clip used to test the automated inspection program is shown below (Figure 10b). The stationary field of view was oriented at the underside of the sea ice. Many krill were visible in these images, mostly due to the reduced 'cloudy-day' effect. The deep field of view displayed many more krill, but the image inspection found considerably less than those seen by the naked eye, as seen in Figure 10a. This was due to similarities in the grayscale pixel intensity values of the ice surface and krill.

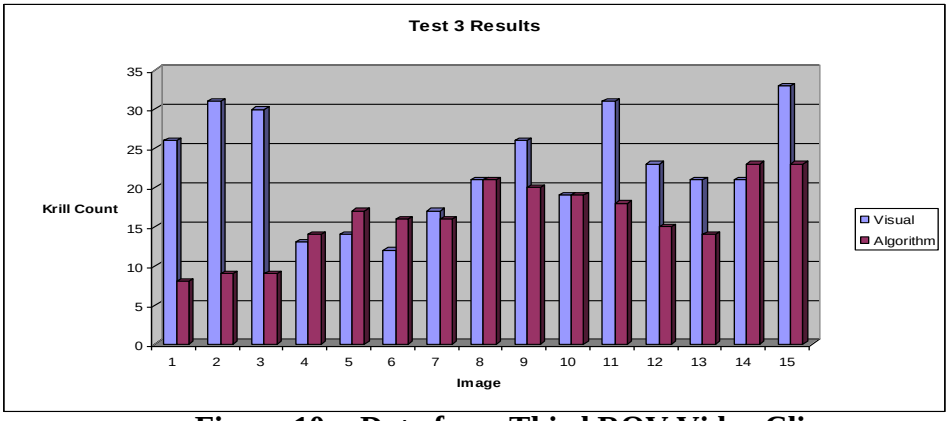

Figure 10a: Data from Third ROV Video Clip

Figure 10b: Images from Third ROV Video Clip

Table 1: Statistical Comparison of Image Analysis Algorithm

Test 1 Image #	Visual Inspection	Automated Inspection	Percent Error
#06301	5	7	40.0
#06311	8	7	-12.5
#06321	9	8	-11.1
#06331	9	13	44.4
#06341	9	8	-11.1
#06351	4	1	-75.0
#06361	13	13	0.0
#06371	15	13	-13.3
#06381	9	8	-11.1
#06391	10	11	10.0
#06401	12	14	16.7
#06411	8	7	-12.5
#06421	9	13	44.4
#06431	9	5	-44.4
#06441	7	7	0.0
Total	136	135	-0.7
Average Percent Error			-2.4

Test 2 Image #	Visual Inspection	Automated Inspection	Percent Error
#06511	8	11	37.5
#06521	10	9	-10.0
#06531	6	8	33.3
#06541	8	6	-25.0
#06551	3	8	166.7
#06561	4	2	-50.0
#06571	4	4	0.0
#06581	8	10	25.0
#06591	3	2	-33.3
#06601	8	12	50.0
#06611	10	8	-20.0
#06621	8	10	25.0
#06631	9	9	0.0
#06641	8	5	-37.5
#06651	7	9	28.6
Total	104	113	8.7
Average Percent Error			12.7

Test 3 Image #	Visual Inspection	Automated Inspection	Percent Error
#31951	26	8	-69.2
#31961	31	9	-71.0
#31971	30	9	-70.0
#31981	13	14	7.7
#31991	14	17	21.4
#32001	12	16	33.3
#32011	17	16	-5.9
#32021	21	21	0.0
#32031	26	20	-23.1
#32041	19	19	0.0
#32051	31	18	-41.9
#32061	23	15	-34.8
#32071	21	14	-33.3
#32081	21	23	9.5
#32091	33	23	-30.3
Total	338	242	-28.4
Average Percent Error			-20.5

The 45 total frames, from each of the 3 ROV clips, were examined with the developed algorithm. The time required for a full visual inspection and data logging were also recorded for comparison against the automated inspection. The automated machine vision inspection required less than 3 seconds to count and log the data, while the visual inspection of the images took just under 40 minutes (Table 2).

Table 2: Elapsed Inspection Time

	Visual	Algorithm
Test 1	10 minutes	<1 second
Test 2	12 minutes	<1 second
Test 3	15 minutes	<1 second

In contrast, the performance count variation between ROV clips is significant. As shown in Table 1, the difference between the visual inspections for krill population estimate versus the automated algorithm varies by about 30%. Although some of the error percentages are severe, one must consider the number of objects located, i.e. the fewer the number, the broader the range of the percent error. The magnitude of the difference illustrates the problem of the frame-by-frame counting. These can be contributed to inconsistencies and excessive noise in the ROV images; glaring, discrepancies in the pixel intensity values, inability of the algorithm to distinguish between the krill/background and the blurring of krill. These issues reduced the quality and accuracy of the inspection analysis for both the visual and automated processes. Due to the quality of the ROV images and limited abilities of the Vision Builder program, the

automated krill population estimates, although considerably faster, did not accurately represent those made by visual inspection.

Test 3 (Figure 10a-10b and Table 1) displays the most considerable deviation from the visual inspection, which was due to the underside of the Antarctic Sea Ice being within the field of view of the ROV. This resulted in double counting of single krill due to the low intensity contrast between the object of interest and the background, as shown in Figure 11.

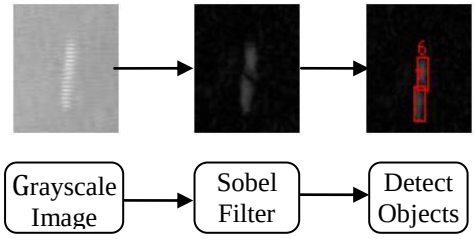

Figure 11: Doubling Counting of a Single Krill

V. CONCLUSIONS

The application of computer aided inspection for krill population estimation, although inconclusive in this experiment, does seem to have practical application. Further testing, involving more complex machine vision algorithms, as well as, digital image processing techniques can greatly increase the accuracy of the inspection. Through research and continued algorithm testing, we hope to develop a vision system that can accurately adapt to the Antarctic water conditions and further the scientific research being conducted there.

VI. ACKNOWLEDGEMENTS

This work was funded in part through the UTSA Office of Sponsored Research under their Collaborative Research Seed Grant Program (CRSGP-2008). In addition, we wish to acknowledge NSF SIMBA program.

VIII. REFERENCES

[1] "SIMBA: Sea Ice Mass Balance in the Antarctic." [Online information], [2008 June 10], Available at http://www.utsa.edu/lrsg/Antarctica/SIMBA/

[2] "ROV – SeaBotix Inc. LBV-ROV." [Online information] 2008, [2008 June 17], Available at http://www.seabotix.com/

[3] J. Yuh, "Design and Control of Autonomous Underwater Robots: A Survey," Autonomous Robots, 2004, pp. 7-24.

[4] H. Singh, J. Howland, and O. Pizarro,"Advances in Large-Area Photomosaicking Underwater," IEE Journal of Oceanic Engineering, *vol. 29*, no. 3, pp. 872-886. 2004.

[5] D. Jones, S. McPhail, B. Bett, C. Flewellen, and M. Conquer, "Seabed Photography from an Autonomous Underwater Vehicle," Journal of Marine Science and Environment, pp. 21-28, 2005.

[6] M. Caccia, "Experiments in Low Cost High Precision Motion Control for ROVs," in Proc. IEEE International Conference on Robotics and Automation, Barcelona. 2005, (pp. 4667 - 4672).

[7] S. Negahdaripour, X. Xu, and A. Khamene. " A vision system for real-time positioning, navigation, and video mosaicing of sea floor imagery in the application of ROVs/AUVs," in Proc. Fourth IEEE Workshop on Applications of Computer Vision '98, 1998, pp. 248-249.

[8] A. Ortiz, M. Simo, and G. Oliver, "A vision system for an underwater cable tracker," Machine Vision and Applications (IEEE WACV), 2002, pp. 129-140.

[9] A. Fairweather, A. Grieg, and A. Allnutt, "Object Recognition by Machine Vision to Enhance Scene Interpretation in an Underwater Application," in Proc. OCEANS '95. MTS/IEEE. Challenges of Our Changing Global Environment, pp. 1865 - 1870.

[10] C. Fritsen, "Final Report of SIMBA's SIMCO's." [Online Document], [2008 September 19], Available at http://www.utsa.edu/lrsg/ Antarctica/SIMBA/

[11] N. Andres, R. Marimuthu, Y. Eom, and B. Jang, "Development of a machine vision system for automotive part inspection," ICMIT 2005: Information Systems and Signal Processing, 2006.

[12] National Instruments, NI Vision: NI Vision Concepts Manual, Austin, Texas: National Instruments Corporation, 2005.

[13] "Free Video to JPG Converter." [Online Download Service], [2008 June 6], Available at http://www. dvdvideosoft.com/products/dvd/ Free-Video-to-JPG-Converter.htm

[14] R. Gonzalez, and R. Woods, Digital Image Processing, 2nd ed., Prentice Hall, New Jersey, 2002.